Aerodynamic investigation of an airfoil in deep stall using SU2

A report submitted in partial fulfillment of the requirements of the course

AE5110: Master's Thesis AE

Ravi Ramesh

Delft University of Technology

TUDelft

Aerodynamic investigation of an airfoil in deep stall using SU2

A report submitted in partial fulfillment of the requirements of the course

by

Ravi Ramesh

Student Name	Student Number
Ravi Ramesh	5020336

Company Supervisor: Dr. Huseyin Ozdemir
University Supervisor: Dr. Francesco Avallone
Institutions: TNO Petten, Delft University of Technology
Place: Faculty of Aerospace Engineering, Delft
Project Duration: December, 2020 - October, 2021

TUDelft

Preface

"Glorious is the fruit of good labour" - one of my favourite quotes that I had come across in recent times during the journey of my thesis in one of my Dutch classes. This sparked an interest in me during my thesis during the difficult periods when I would be stuck. This was also a quote that I would resonate with at a fundamental level, which has been the driving force throughout the journey of thesis as well.

DDES simulations, on the outset, were not a new method to analyze flow fields - there have been extensive studies using these methods for a multitude of applications. However, for an airfoil in deep stall, this has been performed, but had not been completely understood from the flow physics point of view. Therefore, as a student of Aerodynamics, this provided an impetus to begin an investigation, first during my internship, where I first got introduced to basic DDES simulations, and then later during my thesis, wherein I had analyzed DDES simulations on my own for the final purpose of acoustics. From a wind energy perspective, it was quite refreshing to explore an airfoil in deep stall as a special case of wind turbines operating in stalled conditions, or wind turbines experiencing strong gusts, both of which were real-life examples that provided me further purpose to explore this case in more detail and provide scientific insights into the flow phenomenon.

Despite all the pitfalls that I had fallen into during my thesis journey, I would like to first thank my supervisors, without whose patience and acceptance of my results, I would not be in the position that I am today. Next, my parents for providing me their unending support during this journey. And finally, to God and my friends during various stages of my journey, who had ensured that I did not lose track of my final goal.

Ravi Ramesh
Delft, November 2021

Abstract

Airfoils in deep stall have been a subject of extensive computational discussion in the past, with multiple efforts being performed by various institutions to test their solvers and turbulence/hybrid sub-grid scale (SGS) models for their use in massively separated flows. This case has an important application in turbomachinery where unsteady flow is encountered - including wind turbines and helicopter rotors - for studies in both aerodynamics as well as aeroacoustics. Stalling conditions are caused in these applications when there is blade-wake interaction, and also in the presence of strong gusts. The change in the local flow physics in both these cases is caused by a local variation in the angle of attack, which can affect the aerodynamic performance from entire blades.

Although there have been studies in the past that have involved various hybrid SGS models and turbulence models to investigate the effect of them for this flow case, the shear-layer adapted SGS (SLA-SGS) model has not found precedence for the purpose of aerodynamic investigation in this flow case. Therefore, this thesis provides an extensive aerodynamic investigation of an airfoil in deep stall, with a comparison of flow field visualization results using this approach, and comparing aerodynamic performance parameters with other hybrid SGS models. An attempt has also been made to compare the simulation results with other turbulence models and meshing strategies for similar airfoils, to present a case to estimate the similarities and differences in performance.

The results show that the there is an overprediction of the trends obtained from the 3D results compared to the 2D experimental data. The sectional 2D results also show an overpredicted output. Contradictory results are obtained in comparison to the reference literature used for different SGS models.

Finally, additional studies have been performed on the aerodynamics points of view, with an overview of the acoustics code implementation in SU2 being provided. This is in order to provide an insight into not only the working of the code, but also the possibilities of implementing the code for providing acoustic outputs for the present case.

Contents

Nomenclature

Abbreviations

Abbreviation	Definition
SU2	Stanford University Unstructured
NACA	National Advisory Committee for Aeronautics
DDES	Delayed Detached Eddy Simulation
LES	Large Eddy Simulation
CFL number	Courant-Friedrich-Lewy number
S-A model	Spalart-Allmaras model
PSD	Power Spectral Density
CTUs	Convective Time Units
FW-H	Ffowcs-William and Hawking
DES	Detached Eddy Simulation

Symbols

Symbol	Definition	Unit
U_∞	Freestream Velocity	[m/s]
M	Reynolds number	[-]
b	Span	[m]
c	Chord length	[m]
k	Wave number	$[m^{-1}]$
C_l	Sectional lift coefficient	[-]
C_d	Sectional drag coefficient	[-]
C_n	Sectional normal force coefficient	[-]
C_t	Sectional tangential force coefficient	[-]
t^*	Non-dimensional time steps (CTUs)	[-]
Δ	Characteristic grid size	[m]
∇	Divergence operator	[-]
ρ	Density	[kg/m^3]
μ	Molecular viscosity	[kg/m-s]
ν_t	Turbulent viscosity	$[m^2$/s]
$\frac{\partial}{\partial y}$	Spatial gradient of a quantity	[quantity unit/m]

List of Figures

List of Tables

1

Introduction

Airfoils encounter various kinds of flows in different kinds of conditions, some of which cause unsteady effects in them such as unsteady blade loading or delaying the onset of stall amongst other effects [1]. These effects are especially important from a turbomachinery perspective, which include both wind turbines [2] and helicopter blades [3]. The blades for these applications often encounter unsteady inflow conditions [4]. The aerodynamic performance of these blades can also be affected by factors that increase the noise generated by them as well, which include the impact of blade-wake interaction [2], as well as blades exposed to a sudden gust [5]. Both of these phenomena can alter the local angle of attack on the blade. Therefore, this can lead to a stalled condition in some extreme situations, which can adversely impact the overall performance of the unsteady airfoil in each case. Furthermore, the flow physics of the noise generation mechanisms of airfoil flow separation and stall is a relatively less understood phenomenon. Therefore, a thorough aerodynamic investigation of airfoils in deep stall is necessary.

In order to analyze this, one must have to explore the existing flow physics that has been obtained as insights into what could possibly be expected from the flow problem at hand. There have been multiple methods that have been used in academia for this purpose, that include both experimental ([6]) and more so, computational ([7], [8]) approaches. The findings from all these studies have been further described in Chapter 2. The next step would be to identify the methodology that must be used to resolve the flow field, and possibly model certain flow structures, and then the numerical schemes used to analyze such flow problems. The methodologies can be further divided based on the basis of the method used to obtain the flow solution. This flow solution can be obtained by the use of multiple methods, that include the Reynolds Average Navier-Stokes (RANS), Large Eddy Simulations (LES), and Delayed Detached Eddy Simulation (DDES). These methods have been classified based on the kind of fidelity till which they resolve the turbulence present in the flow. While the RANS method obtains the flow solution by taking the mean flow properties into account, the LES method resolves the large-scale eddies, while modelling the smaller ones. Finally, the DDES method is a kind of a hybrid RANS/LES approach, in which the boundary layer is resolved by using RANS (or unsteady RANS - URANS), and the flow regions, where the boundary layer is detached, are resolved by using the LES method. First described by Spalart [9], this method has proved not only to be quite intuitive from the flow physics point of view for multiple applications, but has also been quite cost effective in comparison to RANS. The use of such a method for massively detached flows has also been well documented [8]. Since it is well-known that there is a massive detached flow region in an airfoil undergoing deep stall ([7], [10]), it would only be logical to use such a method to further probe into the current problem statement. Also, the qualitative analysis of this flow problem can be of great importance when considering fluid-structure interactions of wings and blades on a larger scale, as the flows predicted by these methods can cause different structural responses, with DDES possibly predicting a vibration with different patterns and frequency responses [11].

The next section on numerical schemes would describe the kinds of methods that are used to solve the governing equations in the flow in more detail, providing a method to discretize the

continuous form of these equations that are used. These numerical schemes are one of the primary focus points of this thesis, as will be seen in the subsequent chapters. The parameters that are used for the simulation are then described in Chapter 3, with details regarding the mesh, freestream and numerical settings described. The flow field is studied in great detail in Chapter 4, with appropriate physical explanations given in the context of the visualizations shown.

To conclude, Chapter 5 provides a bird's eye view of the main takeaways that can be obtained from the thesis, with some additional recommendations that future researchers could implement in Chapter 6. Additional reading material for the inquisitive reader regarding certain calculations in the thesis, as well as other clarifications, has been placed in Chapter A. In order to provide a glimpse, but a detailed overview of the acoustics code implementation in SU2, a dedicated chapter in Chapter B.1 has been mentioned in the appendix for the purpose of explaining the functionalities of the code, with a brief summary of how it could be operated for future use. The acoustics code could not be applied in the interest of the research questions that were planned for the thesis, as well as due to some lacking existing functionalities of the code that would be required for further analyses. Therefore, it has been mentioned as an appendix at the end of the report.

Lastly, one additional chapter in the appendix describing the various additional studies performed in the analysis of the flow problem have also been described in Appendix C. These include a brief statistical analysis of the lift and drag coefficients that would provide further support to the findings. Next, additional studies regarding the performance of the DDES grid to support LES considerations, and the comparisons with DES grids are also done. And finally, some considerations regarding the attempts performed using a fine mesh are also described.

<div align="right">

2

</div>

Literature Study

This section describes the literature studied in the past in the context of deep stall. An introduction to the flow physics involved in airfoils undergoing deep stall is first provided in the first few sections, with a further investigation into the findings from the literature as described in Section 2.1. Next, the the research questions are described in more detail in Section 2.2. The governing equations are then described in more detail in Section 2.3, while the various numerical schemes for Computational Fluid Dynamic (CFD) studies are described in Section 2.4. To conclude, the various methodologies to resolve turbulence are provided in Section 2.5.

2.1. Airfoil in deep stall

Airfoils in deep stall have been studied in extensive detail from the computational point of view ([7], [10], [12]), given that massively detached flows are a challenge to simulate, and can prove to be a challenging case study for aerospace applications [12]. Furthermore, the noise generated by these airfoils is also relatively not well understood, and is also important for applications such as turbomachinery and wind turbines [4]. Therefore, one of the objectives of this thesis would be to first study the flow physics involved in the airfoils in deep stall by choosing an appropriate numerical scheme, and then perform additional analyses. The literature study would hence, be described in the following manner. The first sub-section describes the flow physics involved in the analysis of airfoils in deep stall, while the rest provides a study of how the literature describes the flow phenomena that occurs in these airfoils.

2.1.1. Flow physics involved in study

The primary flow physics that was found in the current study involved the following phenomena:

1. Presence of an unsteady, three-dimensional, massively separated wake. This can be observed in the form of periodic vortex shedding that occurs in a coherent manner.
2. There are additional random turbulent fluctuations at higher frequencies.
3. Random modulation and intermittent shedding at lower frequencies.

There is also the presence of shear layer instabilities that are also one of the important sources of noise [5] that can be observed in the detached flow region. This can be found to propagate downstream in the wake region as well. In the literature, these have been found to exist for post-stall angles and not just for deep stall. A diagrammatic representation of this is given in Figure 2.1. Furthermore, adding to these instabilities, there is also the presence of shear layer flapping that can be observed at lower Strouhal numbers. An airfoil in deep stall has these as well, including the presence of shear layer flapping that can be observed at lower Strouhal numbers (at approximately St = 0.02-0.03).

<div align="center">

3

</div>
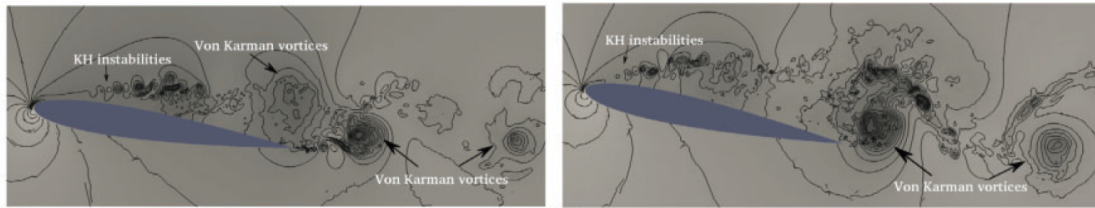
Figure 2.1: Pressure contours of an airfoil in pre-stall (left) and post-stall (right) [13]
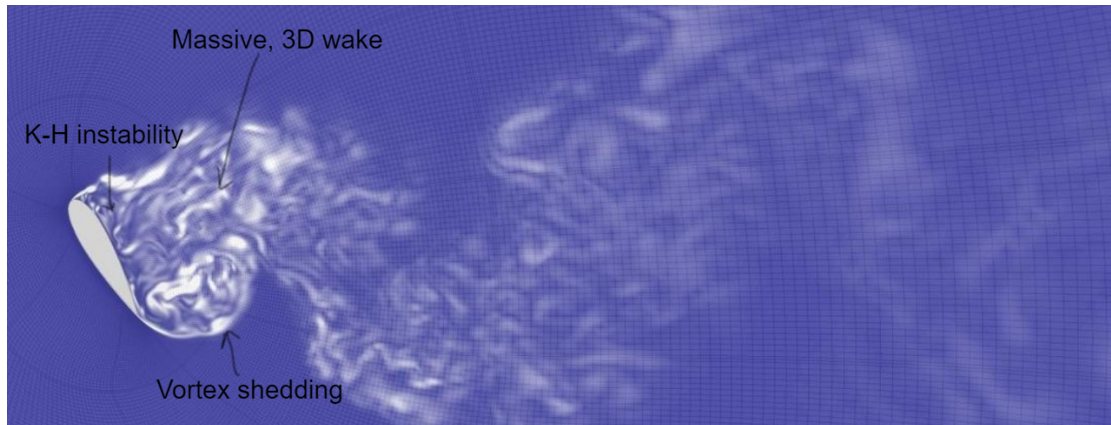
Figure 2.2: Physical phenomena that can be observed in a vorticity contour in an airfoil in deep stall [14]

In Figure 2.2, it can be observed that in a similar manner as the post-stall angles, there is also the presence of shear-layer instabilities like K-H instabilities in airfoils undergoing deep stall. There is also the presence of a massively separated wake region in the suction side of the airfoil, which also has the presence of vortices that propagate downstream of the airfoil. Another interesting observation that one can also expect is the resolution of various spatial scales that are present in the wake (from the smallest ones to the largest that are of the order of the fraction of the chord length of the airfoil).

2.1.2. Experimental findings from the literature
So far, the major experimental data that was used to obtain comparisons with in the literature, given the complexity of the unsteady flow regime, has been found to be quite limited. In fact, the experimental data obtained from Swalwell [6] has been widely used for comparison for airfoils in deep stall ever since computational studies have been performed. In the current paper as well, the comparison made for the simulation setup, as will be described in Chapter 3, was performed using the same experimental data. The pressure data that was used to obtain the lift coefficient and the corresponding pressure coefficient was using a setup as shown in Figure 2.3.
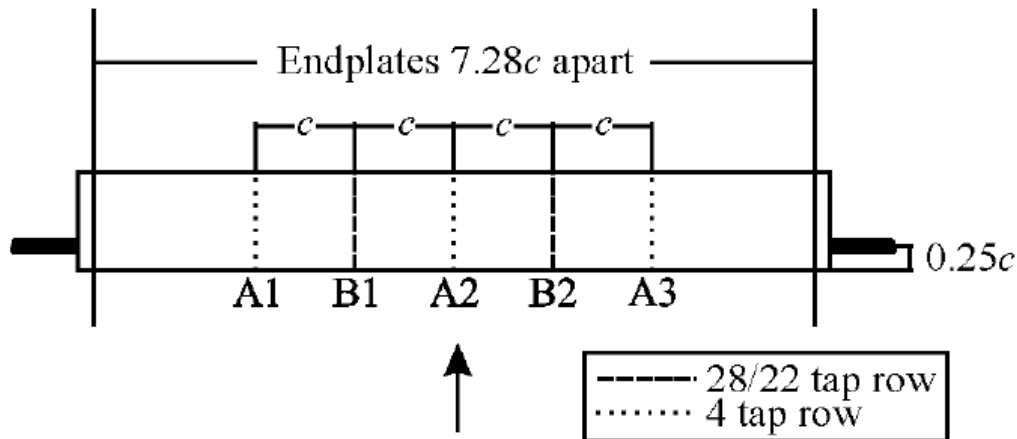
Figure 2.3: Location of pressure taps according to experiment [6]

From Figure 2.3, it is important to mention that the pressure taps that were taken into consideration were located at locations B1 and B2 respectively. From basic mathematics, it is easy to compute that the location of the pressure calculation is at 0.363 times the span. This location has been henceforth used for obtaining calculations of different aerodynamic parameters for future comparisons.

Some of the important findings that one can obtain from this paper are that at an angle of attack of $60°$, the length scale that was used to calculate the Strouhal number took into account the wake width. A similar convention was taken into consideration for flat plates by Fage and Johansen [15]. Given that the current analysis did take into account a large wake into consideration, it is quite clear to take the same length scale into account when comparing the results from the experiment. Furthermore, it can also be mentioned that the experimental time series obtained provide some very interesting conclusions regarding the flow physics, as shown in Figure 2.4.
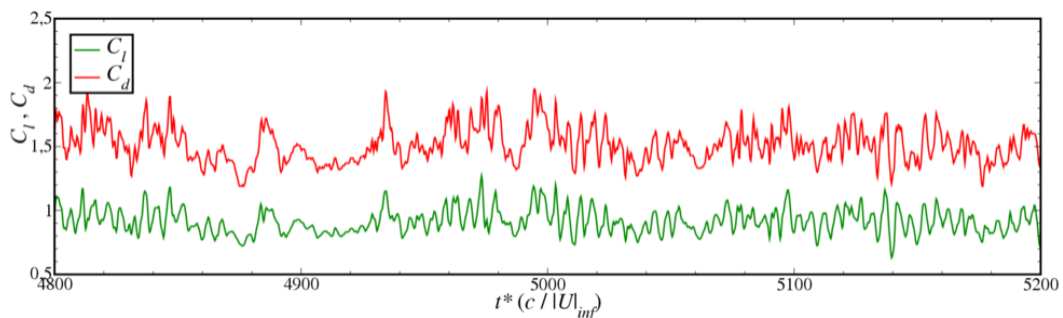
Figure 2.4: Experimental time series of C_l and C_d [6]

One of the most important observations that one can infer from Figure 2.4 is the nature of these fluctuations. This was described by the DESider project [14] as quasi-periodic, and by Zhang [16] as chaotic. It can, however be observed that Figure 2.4 depicts two different cycles of shedding. This included the quasi-periodic vortex shedding cycle of the von Karman vortices, along with the presence of a significant low frequency intermittent region. This is a result that would also impact the remaining analyses, and is also one of the major points of comparison in computational evidence found in the literature, as well as in the current flow problem in the thesis.

2.1.3. Computational findings from the literature

In comparison to experimental data, computational studies on airfoils in deep stall have been given a lot of detail in the literature. Given the presence of a large detached flow region, it has been of great interest to explore the use of hybrid RANS/LES methods, that are a subject of discussion in Section 2.5.3. One of the first studies conducted in the literature for such a flow regime, that involved massive 3D separation to analyze the complex flow physics in it, was performed by Shur et al. [7] for an angle of attack of $45°$. From this study, it was clear that using a URANS approach was not suitable for predicting the vortex shedding, as it simply suppressed out the smaller eddies and effectively dampened out the three-dimensionality of the flow field. The DES approach, however, was found to predict a more physical result by accurately capturing vortex shedding, although at the expense of computational costs that were one order of magnitude higher than URANS. An example of the vorticity contours (ω_z) is shown in Figure 2.5.
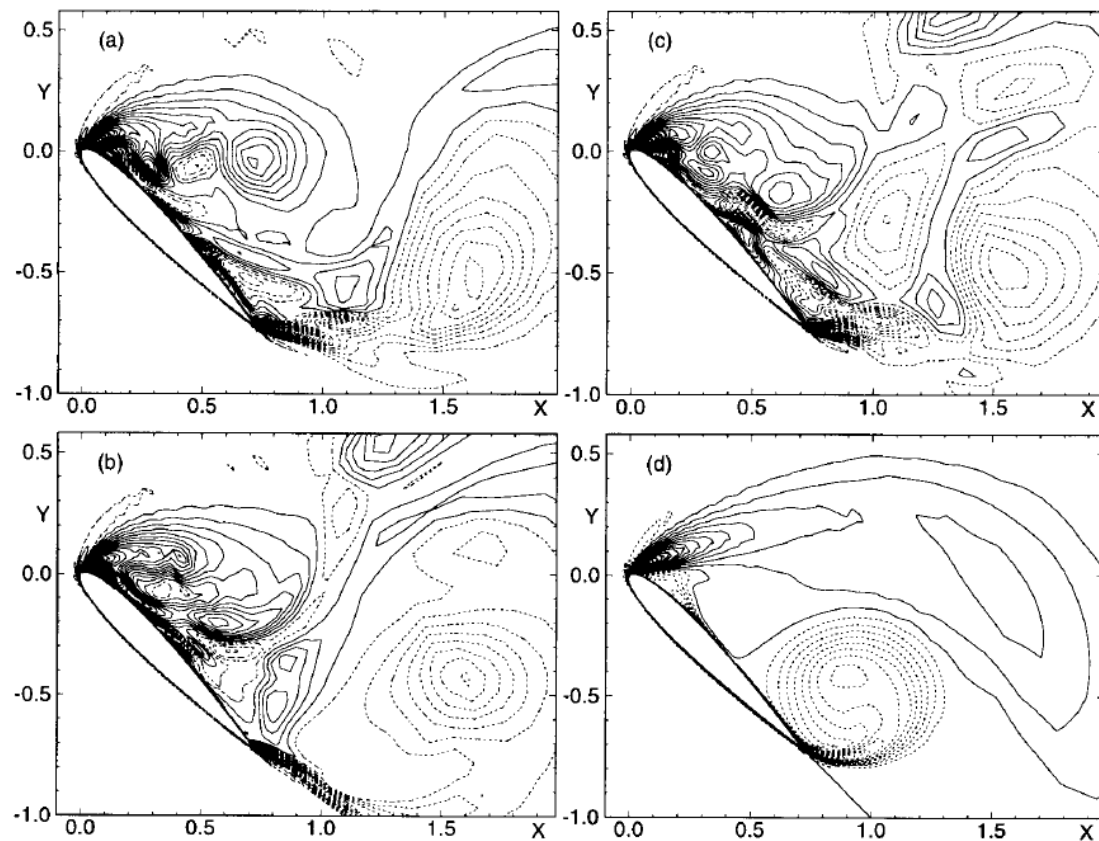
Figure 2.5: ω_z contours for DES simulations of NACA 0012 at angle of attack = $45°$ [7]. Figures (a) - (c) are at locations z/b = 0.25,0.5,0.75. Figure (d) is a URANS result

Further studies were performed by Strelets [8], in which he had used a modified DES approach that involved the use of a hybrid scheme for upwind and central differencing schemes. He had compared the results for two different turbulence models in RANS, namely the S-A and SST models. It could be observed that smaller structures were better visible, but the time history of C_l and C_d were not found to provide reliable time averaged information, as the computational cost was found to be higher. A glimpse of their findings can be shown in the time history of C_l and C_d as shown in Figure 2.6.
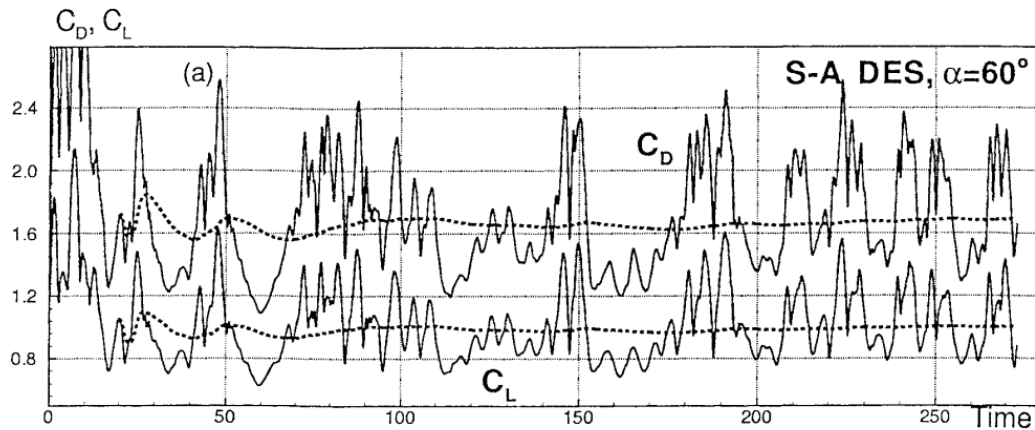
Figure 2.6: Variation of C_l and C_d with CTUs [8]

From Figure 2.6, it is clear that the plots do have a transient behaviour attached with them. The authors had attributed this to a lower amount of computational time used. This was also a reason pointed out as the cause for a largely fluctuating C_l and C_d values.

In order to try different variations of the DES model, the impact of using a different definition of the calibration constant in DES, C_{DES}, was independently pursued by Yan et al. [3]. It was found that using 1000 convective time units (CTUs), a well-converged solution was obtained, which depicted the stochastic behaviour of the unsteady flow. A depiction of this converged behaviour can be observed in Figure 2.7.
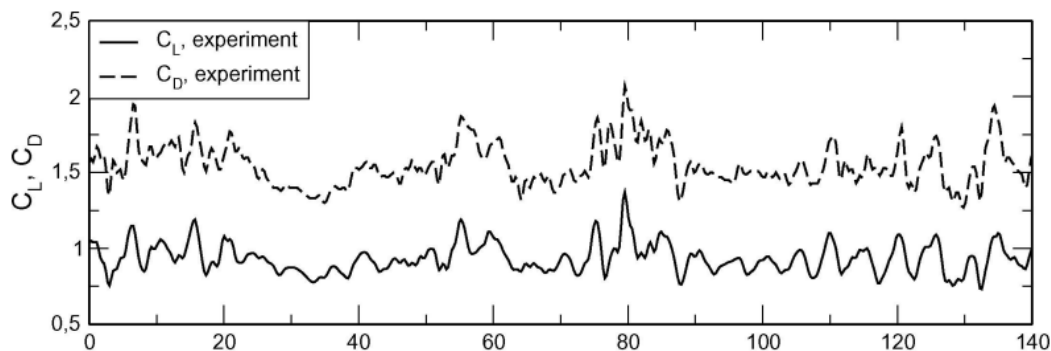
Figure 2.7: Variation of integrated C_l and C_d with CTUs [3]

From Figure 2.7, it can be observed that changing the definition of C_{DES} largely removes a lot of the fluctuations in the integrated C_l and C_d. However, the authors still recommend the simulation to take place for a longer computational time in order to get rid of stochastic effects in the flow.

A key study by Haase et al. and various other EU partners in the ERCOFTAC project using their own in-house solvers, called the DESider project [14], had later simulated the results for a geometry of span $4c$, where c is the chord length taken into consideration. It was observed that the effect of using a smaller span was to, indeed, increase the magnitude of the coefficients. It was shown that having a narrower span as obtained from earlier DES findings for massively separated flows is actually quite optimistic. This was also confirmed by Garbaruk [10], as evidence for having a larger span to study the effects of the span would be better from a computational perspective as well. This is because of the fact that the ratio of the variance (σ) to the mean (μ) value of the aerodynamic performance coefficients, σ/μ, is considerably higher for a lower span ($1c$) in comparison to the $4c$ geometry. Another important finding from the DESider project was that grid refinement did not impact the spanwise averaged results. This is an important point to

be considered in the results, as the over-prediction in the performance coefficients are indeed, due to the absence of a larger span than $1c$.

Yet another study that confirmed the need for a higher number of convective time units was performed by Zhang et al. [16] using a DDES solver that used a Spalart-Allmaras (S-A) turbulence model and second-order upwind schemes for time discretization, but used a smaller span of $1c$, proved to obtain results that confirmed the need to investigate numerical schemes that provided a basis for the results. This can also be observed from the presence of chaotic fluctuations in the time history for C_l and C_d as shown in Figure 2.8.
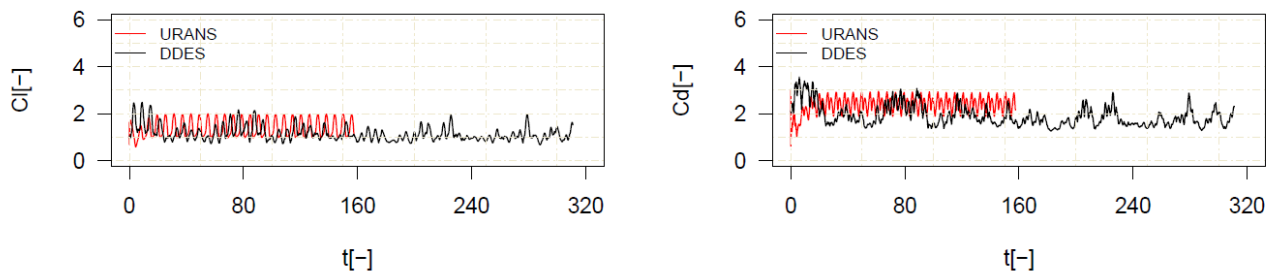
Figure 2.8: Variation of spanwise averaged C_l and C_d with time for (a) DDES and (b) URANS [16]

Furthermore, the need to justify using an appropriate numerical scheme can be seen by using a central differencing scheme alone for time discretization seems to have diffused the numerical errors through all frequencies, as can be observed in the PSD plot shown in Figure 2.9.
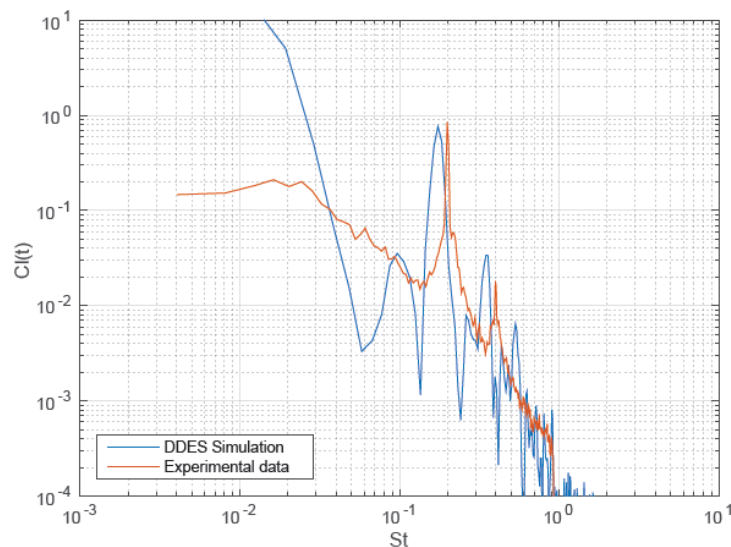
Figure 2.9: Power Spectral Density (PSD) of the lift coefficient (C_l) vs. Strouhal number (St) [16]

Due to the presence of unsteady effects around the airfoil, several subsequent computational studies were performed for studying the impact of different turbulence models and meshes ([17], [18]), as well as with different numerical schemes [12]. In particular, Winkler [17] found that using a different kind of a turbulence model would be useful for predicting the results. This is because of the fact that a modified S-A model would be useful to allow dissipation of the largest energetic scales of the flow at the smallest scales, whilst allowing for the turbulence spectrum to form in the presence of massively detached flows, as was also defined by Patel [18].

Finally, Lacagnina [5] included, although for the sake of acoustics, the presence of three primary sources of noise that would also be a basis for mechanisms that govern the flow physics

of airfoils in deep stall. These include coherent structures in the detached shear layer, wavelike instabilities, such as K-H instabilities in the detached shear layer, and shear layer flapping. This was also confirmed by the findings of Moreau [19] earlier, when the Sound Pressure Level (SPL) findings obtained by him indicated the presence of both vortex shedding and the corresponding shedding harmonic.

From the literature, there has been an investigation into different turbulence models and numerical schemes and how they impact the solution. However, there is a clear need to investigate how varying different hybrid SGS models when using LES in the detached flow regions, that would impact the flow solution. Although studied by Molina [12], the impact of this would have to be seen with a model that would be useful for shear layer flows, as has not been studied in earlier findings in the literature. Therefore, there is a need to investigate in the literature as to the exact gaps in the existing literature to find an answer to two major studies performed in the thesis - one, to identify how the use of a certain numerical scheme and turbulence model affected the flow physics, and second - how this affected the performance parameters of the airfoil itself. Therefore, the research questions are defined next to justify the requirement of such an analysis.

2.2. Research Questions

The research questions that are to be investigated in this thesis are divided primarily into two - one major research question and the corresponding sub-research questions.

The major research question that is to be investigated as a part of this thesis is:

> ***How can the aerodynamic performance of an airfoil in deep stall be described using the DDES approach by employing SU2?***

The sub-research questions are as follows:

1. What is the influence of the hybrid SGS model on the performance characteristics of the airfoil?
2. What is the influence of increasing the number of inner iterations on the performance characteristics of the airfoil?
3. What is the influence of the hybrid SGS model on the determination of accurate flow physics?

The answers to the above questions will be shown in the following steps:

1. The complete aerodynamic study of the results was performed, which involved a case study of the number of inner iterations affecting the aerodynamic results.
2. A separate section within the aerodynamic results section has been dedicated to the investigation of how well a simple model to calculate lift and drag affects the time history coefficients, as well as the corresponding comparison with the 3D results have been described in detail.

The next step would to describe the governing equations involved in the flow around the airfoil.

2.3. Governing equations of motion

Fluid motion around any given body, is governed by certain physical laws, which can be written in a condensed form as the Navier-Stokes equation. This equation obtained by simply solving the continuity and the momentum equations in such a way that includes the modelling of the viscous stress tensor τ_{ij}. These equations are simply a consequence of the conservation of mass and momentum respectively. These equations can be summarized by Equations 2.1 and 2.2 respectively from a fluid particle (Lagrangian) frame of reference.

$$\frac{D\rho}{Dt} + \rho(\nabla \cdot \vec{V}) = 0 \tag{2.1}$$

$$\rho\frac{DV}{Dt} = \rho g + \nabla \cdot \tau_{ij} \tag{2.2}$$

Where V is velocity field, ρ is the density and τ_{ij} is the viscous stress tensor, that is defined by Equation 2.3.

$$\tau_{ij} = -p\delta_{ij} + \mu\left(\frac{\partial v_i}{\partial x_j} + \frac{\partial v_j}{\partial x_i}\right) + \delta_{ij}\lambda\nabla \cdot V \tag{2.3}$$

Where p is the pressure field, v is the velocity component of the velocity field V, δ_{ij} is the Kronacker delta function that determines whether a given function has a non-zero value or not depending on whether the indices based on tensor notation are equal or not respectively. The notations i, j are based on tensor calculus, where the ith index is for the primary variable and the jth index is for any dummy variable. λ is the second coefficient of viscosity, defined by Stokes' hypothesis [20], that is related to the molecular viscosity μ for isotropic flows as given by Equation 2.4.

$$\lambda = -\frac{2}{3}\mu \tag{2.4}$$

By substituting Equation 2.3 into Equation 2.2, wherein the latter describes the momentum equation, one obtains the Navier-Stokes equation as shown in Equation 2.5, which is the major equation that is discretized in all CFD calculations.

$$\rho\frac{DV}{Dt} = \rho g - \nabla p + \frac{\partial}{\partial x_i}\left[\mu\left(\frac{\partial v_i}{\partial x_j} + \frac{\partial v_j}{\partial x_i}\right) + \delta_{ij}\lambda\nabla \cdot V\right] \tag{2.5}$$

In Equation 2.5, it can be observed that the viscous stress tensor term has to be known exactly in order to solve for the velocity field. In the case of incompressible flows, the density can be assumed to be independent of the pressure. Also, assuming that the dynamic viscosity μ is also constant, the Navier-Stokes equation for incompressible, three-dimensional (3D) flows can be simplified and given by Equation 2.6.

$$\rho\frac{DV}{Dt} = \rho g - \nabla p + \mu\nabla^2 V \tag{2.6}$$

For the flow involved in the current flow problem, the ρg term is negligible, because of the absence of body forces on the airfoil. Therefore, the main term that has to be taken into consideration is that of the stress tensor itself. Given that for most flows, it is difficult to obtain this term exactly, it is necessary to create models for them, so that the equations of motion for the fluid can be solved. Also, solving these equations of motion is not an easy task analytically. Thus, there is a need to provide numerical methods to solve these Therefore, the upcoming section describes the need to provide numerical means to solve these governing equations in some more detail.

The next step would to describe the methodologies involved in approaching to solve the current flow problem and answer the research questions. This involves the following two steps: first choosing the right turbulence model, and second, to describe the numerical schemes that would be suitable to resolve or model (or both) the appropriate turbulent flow structures. These approaches will be described in the next section.

2.4. Numerical schemes in CFD

Numerical schemes form an important part of solving the continuous form of governing equations in any flow physics problem. The ones involved in the current aerodynamic analysis arise from different schemes in CFD, which can be broadly classified into the popular finite difference (FD), finite volume (FV) and the finite element (FE) methods, along with their variants. For the given problem statement, which is the analysis of the flow field around an airfoil in deep stall, the

numerical schemes used depend largely on the turbulence approach that is used for the analysis of the problem. This section, hence, deals with the numerical schemes that have been used by authors in the past for the purpose of analyzing the flow field around airfoils.

In CFD, there are primarily two major numerical schemes that are used for the analysis of a general flow problem, namely spatial schemes and temporal schemes. Spatial schemes can be further divided into central schemes and upwind schemes, depending on their frequency of their usage in the literature.

Central schemes have been found to be used in the analyses of various kinds of flow problems in the literature [21]. In this scheme, a first order spatial gradient ($\frac{\partial u}{\partial x}$), in its most general form, can be written as given in Equation 2.7.

$$\left(\frac{\partial u}{\partial x}\right)_i \approx \frac{1}{\Delta x} \sum_{j=-M}^{M} a_j u_{i+j} \qquad (2.7)$$

Where M is the stencil width, which is unity for the simplest central difference scheme, which is the second-order scheme, which is given by Equation 2.8. This is very commonly used in standard CFD applications, along with additional artificial dissipation terms in order to account for numerical errors, that would otherwise cause the solution to be contaminated.

$$\left(\frac{\partial u}{\partial x}\right)_i \approx \frac{1}{2\Delta x}(u_{i+1} - u_{i-1}) \qquad (2.8)$$

Given that the current analysis requires the study of highly unsteady phenomena, the use of RANS would highly limit the analysis, as RANS provides flow results only in steady state conditions. However, even using URANS in the literature has been found to provide unsatisfactory areodynamic results, and almost dissipating the small amplitude waves, such as acoustic waves, in their entirety [22] because of the presence of excessive numerical dissipation. Therefore, turbulence approaches of higher fidelity are required, and in the given problem statement, a mixture of RANS and LES approach, called the DDES approach, is considered, as it is able to resolve the larger eddies, which contain most of the turbulent kinetic energy, while modelling the small-scale turbulent structures. Furthermore, since LES is an inherently unsteady method, it makes it even more useful to solve the problem statement at hand.

The central differencing schemes are popular for use in LES because of two reasons. First, when used with the finite volume (FV) method, these schemes can be used in skew-symmetric form [21]. Second, they have a built-in dealiasing property. This is an attractive option for LES, as it allows one to remove spurious waves of certain wave numbers that can contaminate the solution. Fourth-order schemes are also quite popular in LES applications, and a depiction of this has been done by Almutairi et. al. [23], for example. Sixth-order schemes have also been attempted in the past for LES applications, but they have been found to be restricted to fully turbulent boundary layer and channel layer. Sixth-order schemes have also been used in the LES analysis of airfoils [24], which has been shown to provide results that match quite well with experimental data, within the limits of the order of accuracy that is expected from scientific precision.

There is however, an underlying problem with the preceding grids, and that is the fact that these schemes provide accurate results mainly with cartesian and uniform grids. This is because of the fact that their formulation requires mesh points that are not clustered. In order to overcome this issue, upwind or downwind schemes can be introduced, which lay emphasis on the points that are upwind or downwind respectively. This strategy is useful in the case of non-uniform grids, where the clustering of points can be accommodated. Multiple kinds of upwind schemes have been used in the literature in the past for LES applications. One of the most popular schemes used in the past is the MUSCL (Monotonic Upstream centred Schemes for Conservation Laws) scheme [25], which is a modified version of the Roe scheme [26]. The numerical fluxes are calculated by using the cell centers on both the left and right of a given node. The MUSCL approach differs from the Roe scheme in the first-order accurate version, in that the cells that are farther away from the interface are also taken into account for calculating flux values. This

allows the MUSCL approach to expand its definition to obtain a greater accuracy by employing second and third-order schemes. However, one has to apply limiters in order to maintain the monotonous nature of the solution according to Godunov's theorem, which states that monotonic linear schemes for convection problems have to be first-order accurate.

Other higher-order schemes, such as the advection upstream splitting method (AUSM), have been used in high Mach number flows for shock-related phenomena. However, as the present analysis involves low Mach number flows, a variant of the AUSM method called the simple low-dissipation AUSM (SLAU) is more suitable. The SLAU method has the advantages [27] of modifying the pressure flux term in the regular AUSM approach, thus accommodating for multiple velocity directions, and also avoiding unphysical solutions at low Mach numbers by introducing certain empirical functions.

With that being said, an investigation has been made with regards to the various numerical schemes available in the literature. The next step in this analysis would be to provide a method to define the turbulence models that would be required to provide a closure to the discretized equations that are obtained from the numerical schemes discussed.

2.5. Turbulence models in the literature

In the case of obtaining the solution of the Navier-Stokes equations for turbulent flows, the major approaches found in the literature are the Direct Numerical Simulation (DNS) method, Reynolds Averaged Navier-Stokes (RANS) method, [28], Large Eddy Simulations (LES) and the Unsteady Reynolds Averaged Navier-Stokes (URANS) method [29]. The following sub-sections describe the various approaches to model turbulence used in the literature that are relevant for the thesis.

2.5.1. RANS approach

RANS simulations do not resolve any of the turbulent length scales, but models all of them after computing the mean flow solution. Thus, for turbulent flows, the accuracy of RANS solutions depends entirely on the turbulence model used. This results in a lower computational cost, but it does sacrifice the accuracy of the flow physics, especially near the wall, where various turbulent structures, whose length scales are in the inertial range and below, cannot be captured accurately. These structures include streaks, ejections, sweeps, vortical structures of several forms etc [30].

The time averaged version of the Navier-Stokes equations are the governing equations that form the basis of the RANS analysis. This is obtained by dividing any flow quantity into its corresponding mean (denoted by the over-line over the quantity) and the fluctuating component (denoted by the apostrophe over the quantity) respectively. The final Reynolds-averaged form of the continuity and momentum equations are given by Equations 2.9 and 2.10 respectively.

$$\frac{\partial \overline{v_i}}{\partial x_i} = 0 \tag{2.9}$$

$$\rho \frac{\partial \overline{v_i v_j}}{\partial x_j} = -\frac{\partial \overline{p}}{\partial x_i} + \frac{\partial}{\partial x_j} \left(\mu \frac{\partial \overline{v_i}}{\partial x_j} - \rho \overline{v_i' v_j'} \right) \tag{2.10}$$

In the case of turbulence resolution approaches, it is the Reynolds stress tensor ($\rho \overline{v_i' v_j'}$) that is usually required to be modelled, as the averaged fluctuations cannot be obtained explicitly (there are ten unknowns in total, three averaged velocity components and one pressure component, along with six Reynolds stresses). Therefore, there is a requirement for closure of the system of equations. For this purpose, there are many turbulence models that have been devised in the past that are used to obtain exact relations for the Reynolds stress tensor. This is often done by introducing a viscous dissipation factor for the turbulent dissipation occurring in eddies, called the turbulent eddy viscosity (denoted by ν_t). Some of them are briefly described as follows:

Spalart-Allmaras model
First described by Spalart [31], this approach used a one-equation model that was based on empirical calculations to compute the relation between the Reynolds stress tensor and turbulent

eddy viscosity. This model has been found to be extremely good for external aerodynamic flows. However, it makes the assumption that there are no turbulent eddies near walls. This could, however, cause problems in detached flows, where adverse pressure gradients are found [32].

Menter SST model
The Shear Stress Transport (SST) model, developed by Menter [33], was developed by combining the advantages of the original $k - \omega$ model developed by Wilcox [34] in the inner layer of the boundary layer, and utilizing the standard $k - \varepsilon$ in the detached flow regions. This is on account of the fact that in the detached flow regions, the sensitivity of choosing an optimal value of the specific dissipation rate (ω), that causes the model to suffer in those regions. Therefore, by combining the advantages of the two existing turbulence models (using $k - \varepsilon$ in the boundary layer region and using $k - \omega$ in the regions where the boundary layer is detached), the SST model was found to be quite competent in obtaining good results in flows with adverse pressure gradients. In the case of massively separated flows, it can be inferred that there is the presence of adverse pressure gradients in the case as well, which has also been confirmed from the literature on airfoils in deep stall [7].

2.5.2. LES approach
The LES approach is one in which there is a balance struck between modelling some parts of the flow (roughly 10% of the flow that is relative to the smaller scales [35]) that cannot be resolved without sacrificing accuracy, while resolving the rest of the flow, just as in the case of DNS. For this reason, LES can also be termed as quasi-DNS (QDNS) [36], since it provides a lower resolution of the flow, and hence, has a lesser computational expense (roughly by about ten times) in comparison to DNS.

In the case of wall-bounded flows, this would require a sufficiently fine mesh near the wall in order to resolve the length scales within the boundary layer, despite the introduction of wall-models to accurately prescribe the flow physics near the wall [37]. This requirement of a finer mesh near the wall is because of the large discrepancy in the flow scales for those structures near the wall and the ones that are away from the wall. Hence, LES would require much more computational power in comparison to RANS near the wall. However, for non wall-bounded flows, the required resolution of the domain by using LES has been found to be more successful for predicting the nature of the flow, as viscosity is mainly used to set the scales of the dissipative eddies [38].

2.5.3. Hybrid RANS/LES approaches
In order to combine the advantages, as well as negate the drawbacks, of both RANS as well LES, two approaches could be followed, namely a hybrid RANS/LES approach and the Detached Eddy Simulation (DES) approach. While RANS is a useful turbulence approach for attached flows at high Reynolds numbers, it fails for separated flows and complex flow regimes at a decent computational cost. LES, on the other hand, is good for separated flows, but its prohibitive computational cost limits its application for boundary layer resolution at high Reynolds numbers. This provides a strong incentive to combine the benefits of RANS and LES to obtain a hybrid RANS/LES approach, a variant of which is the DES approach.

The major objective of the hybrid RANS/LES approach is to overcome the need for high grid (mesh) resolution near the wall, which is required by LES, but not by RANS. The basic concept in the two approaches - hybrid RANS/LES and DES - is the same: URANS is applied in the near-wall region, where the near-wall turbulent structures are modelled and not resolved, thus ensuring that the near-wall turbulent structures are captured accurately [39], whereas the regular LES approach is applied away from the walls [40].

The major difference between the hybrid RANS/LES and DES approaches lies in the manner in which they model the boundary layer. While the hybrid RANS/LES approach models only inner part of the boundary layer with URANS, the DES approach models the entire boundary layer with URANS [41]. The difference between the two approaches arises in the requirement of what needs to be computed: while the hybrid method focuses on obtaining information about

the inner part of the boundary layer by modelling while resolving the outer part by using LES, the DES approach focuses on modelling the entire boundary layer by using URANS in the near wall regions, and LES far away from the wall, with the change being brought about by using grid spacing.

Broadly speaking, the hybrid RANS/LES methods can be divided into two categories, namely the zonal and the non-zonal approach. The zonal approach includes those methods in which the user defines the regions where the RANS and LES modes are active. While this approach on the outset has the gray area issue, which is a well-known issue with hybrid RANS/LES approaches as mentioned in the literature [42]. This is because the user specifies the transition from RANS to LES by a synthetic turbulence interface [43]. Hence, it is difficult to implement for complex geometries. Hence, the non-zonal approach, wherein the solver defines the regions where RANS and LES are to be used, is employed. This approach is also quite flexible, and hence, is suitable for complex industrial applications. However, it must be kept in mind that this approach still suffers from gray area effects.

Two major weaknesses of using hybrid RANS/LES as well as the DES approaches have been identified recently. The first one is with regards to that part of the flow region where the URANS and LES models overlap with each other. This area has been traditionally known as the gray area [42]. The transition from RANS to LES in this region causes the velocity fluctuations that develop in the LES region not to completely develop, which can cause nonphysical results, such as a loss in skin friction coefficient and may cause problems such as grid-induced separation in some severe cases [44]. The second weakness concerns the delay in the formation of instabilities in the mixing layers due to the advection of the upstream RANS eddy viscosity. This has been found to cause issues in the field of acoustics [45]. There has been some light that has been thrown with regards to this delay of instabilities, that is based on the concept of using new zonal sub-grid scales that depend not only on the grid spacing, but also on the flow solution that depends on the local vorticity vector as well [42].

2.5.4. Detached Eddy Simulation (DES)

Detached Eddy Simulation (DES) is a kind of hybrid RANS/LES approach in which the entire boundary layer is modelled using the URANS approach, while the detached eddies outside the boundary layer are modelled using LES. DES can be considered as a weak RANS-LES coupling method [42], as there is no mechanism to transfer the modelled turbulence energy to resolved turbulence energy. First introduced by Spalart [9] as DES97, this model is based on the Spalart-Allmaras (SA) turbulence model [31], and uses a modified wall distance ($\tilde{d}$) and grid size (Δ) which are defined by the Equations 2.11 and 2.12 respectively:

$$\tilde{d} = \min\left(d, C_{DES}\Delta\right) \tag{2.11}$$
$$\Delta = \max\left(\Delta_x, \Delta_y, \Delta_z\right) \tag{2.12}$$

Where C_{DES} is an empirical constant equal to 0.65 calibrated by using the assumption of isotropic turbulence by Spalart [9], and Δ_x, Δ_y and Δ_z are the grid sizes in the three spatial dimensions x, y and z respectively. The concept behind using a grid-dependent transition from RANS to LES was developed from the idea that the grid spacing parallel to the wall is much greater than at least half the thickness of the boundary layer, so that non-physical grid-induced separation is not introduced in the regions where the mesh spacing is violated [9]. Furthermore, a large drop of eddy viscosity can lead to the abrupt decrease in the turbulent length scale, thus causing an incomplete generation of LES content. This phenomena is known as modelled stress depletion (MSD). The abrupt reduction in the length scale can also cause the original DES length scale to be lesser than the boundary layer thickness, which results in a condition known as "ambiguous grid densities" for the original DES, and an incorrect activation of LES inside the boundary layer [43].

2.5.5. Delayed Detached Eddy Simulation (DDES)

In order to tackle MSD, some approaches have been taken into consideration, one of which is the Delayed Detached Eddy Simulation (DDES) approach. First introduced by Spalart [46],

this method involves delaying the switch from RANS to LES by re-defining the length scale that represents the distance from the wall ($\tilde{d}$) as given by Equation 2.13.

$$\tilde{d} = d - f_d \max\left(0, d - C_{DES}\Delta\right) \tag{2.13}$$

Where f_d is called the delaying function that depends on the distance from the wall for which the transition from RANS to LES is delayed (called r_d), defined by Equation 2.14.

$$f_d = 1 - \tanh\left(8r_d\right)^3 \tag{2.14}$$

$$r_d = \frac{\tilde{\nu} + \nu}{\sqrt{U_{i,j}\,U_{i,j}}\;\kappa^2 d^2} \tag{2.15}$$

Where $\tilde{\nu}$ is the turbulent eddy viscosity and ν is the kinematic viscosity, $U_{i,j}$ is the velocity gradient, k is the von Karman constant and d is the distance of the mesh element from the nearest wall.

The physical interpretation of Equation 2.14 is to provide a clear distinction to the solver between the zones where RANS would be applied and where LES would be applied. This is where a significant advantage of the DDES approach can be observed: the influence of the local flow physics on its formulation would ensure that there is no unavoidable switching when the flow regime is supposed to operate from the LES mode. Hence, when $f_d = 0$, the flow region would be solved using the RANS approach, while when it is 1, it would be solved using the LES approach. Thus, the DDES approach is advantageous while solving the problem of ambiguous grid densities. In comparison to DES/DES97, it has also been found that the DDES approach is quite resilient to MSD, and only faces the issue when the grid is extremely fine [46].

However, the fundamental problem behind the DES methods, which include the gray area problem has not been solved. Hence, in order to mitigate this, several other methods were implemented to overcome the issue of the transition from RANS to LES in shear flows, such as vorticity-based SGS [42] and shear-layer adapted (SLA) SGS [47], which are described in more detail in subsection 2.5.6.

2.5.6. DDES with hybrid SGS models

SGS models are used in order to provide a method to model the smaller turbulent length scales in the LES regions of the grid. The method in which these models work depends largely on the flow physics to be solved, and essentially define the zone where the transition from wall-resolved RANS proceeds towards LES. The variations of DDES that incorporate the SGS model modifications, namely the vorticity-based DDES, and the shear-layer adapted (SLA) SGS, are described in the following sub-subsections.

Vorticity-based SGS DDES
The vorticity-based SGS model, first described by Deck et al. [48], is a zonal DES approach in which the grid size is defined based on the flow dependent alignment of the vorticity vectors. This is to ensure that the LES content is gradually developed, especially in the case of mixing layers.

A more improved version of the vorticity-based model was developed later by Deck again [42], in which the vorticity-based approach defines the grid size by including the vorticity in each direction to be a weighting factor, as shown in Equation 2.16.

$$\Delta_\omega = \sqrt{n_x^2 \Delta_y \Delta_z + n_y^2 \Delta_x \Delta_z + n_z^2 \Delta_x \Delta_y} \tag{2.16}$$

Where n_x, n_y and n_z are the vectors aligned normally to the vorticity vectors in the respective spatial directions. In the case of unstructured grids, the improved version of the sub-grid scale was defined based on the average cross-section of a cell that is normal to $\vec{\omega}$ (denoted by $\tilde{S}_\omega$), defined as

$$\Delta_\omega = \sqrt{\tilde{S}_\omega}$$

This definition of the grid size ensures that in regions where there is non-zero vorticity, there would be one particular direction that would be indicated by the vorticity vector.

Shear Layer Adapted SGS
There can also be another variation that can be used for the definition of the sub-grid length scale, which is called the shear-layer adapted (SLA) length scale. This combines two different approaches to reduce the excess eddy viscosity generated by certain shear layers: first, by using a SGS sensitive to vorticity as used by Mockett [49], and second, by using an empirical function that takes into account the two-dimensionality of the flow [43]. The definition of the grid is given in Equation 2.17.

$$\tilde{\Delta}_\omega = \frac{1}{\sqrt{3}} \max |I_n - I_m| \tag{2.17}$$

Where $I_n = n_\omega \times r_n$, n_ω is the unit vector that is aligned with the vorticity vector, and r_n is the vector that passes through the cell-centre in the normal direction.

The reason for choosing this definition was because of the fact that the original definition of the grid size, as formulated by Deck in Equation 2.16, reduces to $\sqrt{\Delta_x \Delta_y}$ in the case of 2D flows, in which Δ_z is found to be very small compared to the grid spacing in the other directions. However, as observed by Shur [47], the influence of Δ_y was proving to be quite a problem, as it involved considering the smallest grid direction. Therefore, the maximum of Δ_x and Δ_y was considered. However, because SU2 uses a vertex-based discretization method, one cannot directly apply this definition of the grid size. Therefore, Molina [43] proposed a new definition for vertex-based methods as given by Equation 2.18.

$$\tilde{\Delta}_\omega = \frac{1}{\sqrt{3}} \max |n_\omega \times r_{ij}|_{j=1,n} \tag{2.18}$$

Where n_ω is the unit vector aligned with the vorticity at a point i, and r_{ij} is the edge vector that connects points i and j.

The transition between RANS to LES, as is the case with DES as has been mentioned before, is a problem that has to be mitigated, and the SLA SGS approach does so by scaling down the grid filter, and thus, reducing the eddy viscosity in the initial shear layer. The reason why this formulation was adopted was because the vorticity-based DES model was found to be too "conservative" in the initial region of shear layers that were resolved by anisotropic grids.

For isotropic grids, Shur et al. also proposed an additional kinematic measure to identify those regions in a quasi-2D flow where implicit LES treatment is desirable. This measure, called the vortex tilting measure (VTM), uses a normalized upper bound of the cross-product of the vorticity-evolution term $\hat{S} \cdot \vec{\omega}$ and the vorticity vector $\vec{\omega}$, which can be read as given in Equation 2.19.

$$VTM = \frac{\sqrt{6}|(\hat{S} \cdot \vec{\omega}) \times \vec{\omega}|}{\omega^2 \sqrt{3 \, \text{Tr}\left\{(\hat{S}^2)\right\} - \left[\text{Tr}\left\{(\hat{S})\right\}\right]^2}} \max 1, (\nu^*/\nu_t) \tag{2.19}$$

Where $\hat{S}$ is the strain tensor and $\text{Tr}\{(.)\}$ is the trace of the parameter in brackets, and $\nu^* = 0.2\nu_t$. In inviscid flow regions, the VTM quantity oscillates strongly in space because $\vec{\omega}$ wavers at zero, thus there is a limit applied to prevent numerical issues.

Thus, the new SLA-SGS uses the VTM quantity and the length scale $\tilde{\Delta}_\omega$ to replace the DDES SGS scale as given in Equation 2.13, given by Equation 2.20.

$$\Delta_{SLA} = \tilde{\Delta} F_{KH}(< VTM >) \tag{2.20}$$

Where <.> indicates the average of the quantity within the brackets over the neighbouring cells. This is done so that any strong variations of the VTM function in the regions of developed turbulence are eliminated. F_{KH} is a piece-wise linear function which is used to unravel the

Kelvin-Helmholtz instability in the initial parts of the shear layer. This function is defined as given in Equation 2.21.

$$F_{KH}(<VTM>) = \max\left(F_{KH}^{min}, \min\left(F_{KH}^{max}, F_{KH}^{min} + \frac{F_{KH}^{max} - F_{KH}^{min}}{a_2 - a_1}(<VTM> -a_1)\right)\right) \quad (2.21)$$

Where F_{KH}^{max} = 1.0, F_{KH}^{min} = 0.1, a_1 = 0.15 and a_2 = 0.3. This function has been formulated in such a way that it remains at small values when <VTM> is less than a predefined threshold value, while it increases rapidly to unity with an increase of <VTM>.

Given that the current flow problem has been well established from the flow physics point of view, the governing equations have been described in some detail, the different kinds of numerical schemes available for CFD in the literature are provided, and the various turbulence resolution approaches have been discussed in quite some detail, it would be fitting to move on to the following chapter on how to setup the simulation.

3

Simulation Setup

As has been mentioned in the introduction, the problem statement that would be investigated is the computational investigation of an airfoil in deep stall. The motivation behind this flow problem is to investigate the flow physics of an airfoil in deep stall by selecting an appropriate numerical scheme. This also includes the verification and validation of the results obtained from the simulations with existing literature.

The motivation behind selecting this model has been elaborately explained in Chapter 2. To this end, the flow field investigated in this section of the thesis is that around a NACA 0021 airfoil that is undergoing deep stall. The airfoil experiences stall at an angle of attack of $60°$, which is obtained by keeping the incoming flow to the airfoil inclined at that angle of attack rather than the airfoil being inclined itself, which is a characteristic feature of CFD simulations. The pressure and the suction sides can, therefore, be clearly identified by the presence of vortex shedding on the suction side, and the pressure side can be identified as the part where the boundary layer is attached throughout the airfoil curvature. The presence of deep stall, however, necessitates the use of an existing converged solution in order to resolve the flow field properly by using the DDES turbulence model, in order to avoid numerical errors.

Therefore, the solution procedure that is followed in these calculations is as follows:

1. The **RANS 1st order solution** is obtained by using the existing boundary conditions and convergence criteria, and is run until convergence is achieved.
2. The **RANS 2nd order solution** is obtained by using the converged RANS 1st order solution as an input, in order to ensure that the solution reaches convergence. It has been observed that the solution diverges by directly using a DDES 2nd order scheme, on account of the difficulty in predicting separation just after the leading edge. Therefore, a converged 2nd order RANS solution is provided as an input to the DDES 2nd order solver. The MUSCL numerical approach is activated in order to accurately obtain the pressure fluxes. The solution is run until a satisfactory convergence criteria (obtained from the density residual) is attained.
3. The **DDES 2nd order solution** is obtained by using the converged RANS 2nd order solution and additionally, activating the unsteady simulation settings.

Before proceeding to explain the computational setup involved in the simulation, it would be important to describe the kind of solver that is used in the setup. Thus, the first section describes the solver used (SU2) in brief in Section 3.1. This is followed by the boundary conditions and mesh settings in 3.1.1. The results obtained using the different numerical schemes (1st and 2nd order) and turbulence models (RANS and DDES) are then explained thereafter in Chapter 4.1, with the calculation of the time step explained in 3.2. The results of the DDES 2nd order solution, taking these parameters into account are to be presented in Chapter 4.2 of this report.

18

3.1. SU2 as a solver

Various numerical schemes have been investigated in the past on different kind of solvers, and not every numerical scheme can be used effectively on all solvers. The choice of the solver is merely a tool which uses certain numerical schemes to be used for the application at hand. In the current project, the solver used is an open-source code called Stanford University Unstructured (SU2).

SU2 is an open source software suite written in C++ and Python for the purpose of multi-physics simulations and design [50]. It was built specifically for solving partial differential equations (PDEs) as well as PDE-constrained optimization problems on general unstructured meshes, with its core comprised of a Reynolds-averaged Navier Stokes (RANS) solver that is capable of solving compressible, turbulent flows. Initially being used for aerodynamic applications, SU2 has developed quickly in the last few years, and is being used for a variety of applications, including turbomachinery [51], acoustics [52] and fluid-structure interaction [53].

The focus of the numerical schemes implemented in SU2 will be divided into spatial and temporal schemes for a better understanding of the physical problem at hand.

Spatial schemes

SU2 implements both the finite volume as well as the finite element methods, and in the case of fluid flow and aerodynamic problems, the finite volume approach is the more natural way to proceed towards the solution because of the fact that the method incorporates the effect of source terms quite well, and is also advantageous in terms of memory usage and solution speed as well.

PDEs in SU2 are discretized using the standard edge-based structure that constructs control volumes by using a median-dual vertex-based scheme [50]. These median-dual control volumes are obtained by connecting the centroids of the faces, edges and the midpoints of all the cells that share a given node or vertex. Once the integration for the governing equations over a given control volume for the problem statement is done, the integral, semi-discretized form of a typical PDE is given by Equation 3.1 [43].

$$0 = \int_{\Omega_i} \frac{\partial U}{\partial t} \mathrm{d}\Omega + \sum_{j \in \mathcal{N}(i)} (\tilde{F}^c_{ij} + \tilde{F}^v_{ij}) \Delta S_{ij} - Q|\Delta_i|$$
$$= \int_{\Omega_i} \frac{\partial U}{\partial t} \mathrm{d}\Omega + R_i(U) \tag{3.1}$$

Where R_i is the residual obtained from the spatial integration of all the terms in the control volume surrounding the vertex *i*, $\tilde{F}^c_{ij}$ and $\tilde{F}^v_{ij}$ are the numerical approximations of the convective and the viscous fluxes that are projected along an edge respectively, and Q is the source term.

Several numerical schemes have been implemented in SU2 for the purpose of doing a spatial discretization, which include the JST (Jameson-Schmidt-Turkel) method, Roe's scheme, AUSM, HLLC and Roe-Turkel [50]. From the analysis performed in Sections 2.4, it can be safe to say that various higher order schemes are suitable in the use of methods that involve low dissipation and dispersion schemes, such as the AUSM method and its variants, such as the SLAU algorithm, are a good options for the analysis of the given problem statement. And as justified in sub-section 2.4, the SLAU algorithm is the more useful variant that is applicable for low Mach numbers.

Temporal schemes

The time marching technique for an ordinary differential equation as shown in Equation 3.1 is shown in Equation 3.2.

$$0 = \frac{\mathrm{d}(|\Omega_i|U_i)}{\mathrm{d}t} + R_i(U) \tag{3.2}$$

The forward or the backward Euler schemes are available, and based on stability and performance, one has to choose the right scheme. In the given problem statement, it is better to go

for the implicit (Backward-Euler) scheme because it allows for greater stability and convergence in the case of numerically stiff flow problems [43]. Another advantage of implicit schemes is the fact that they enable the use of higher CFL conditions than the ones in explicit methods, which allow to transfer the values of certain time steps to allow to relax the flow problem. Dual-time stepping is also advantageous, and can be used to achieve a higher-order accuracy in time. This is performed by converting an unsteady problem into a series of steady problems, that can be solved with the well-known algorithms for convergence acceleration at each physical time step.

The next section describes the boundary conditions and the kind of mesh used for the simulation setup involved in brief.

3.1.1. Boundary conditions and mesh settings
This section describes both the boundary conditions, as well as the mesh settings separately by using a single diagram.

Boundary conditions
A description of the boundary conditions is provided in Figures 3.1(a) and 3.1(b) respectively.
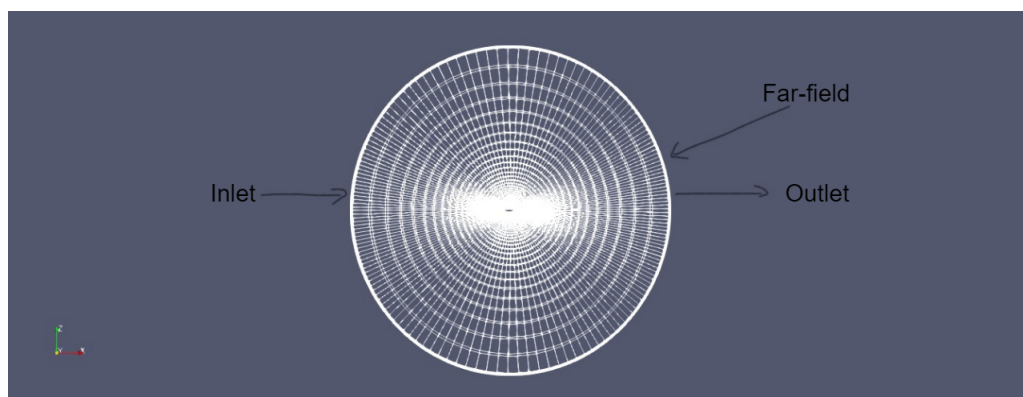
(a) Mesh overview
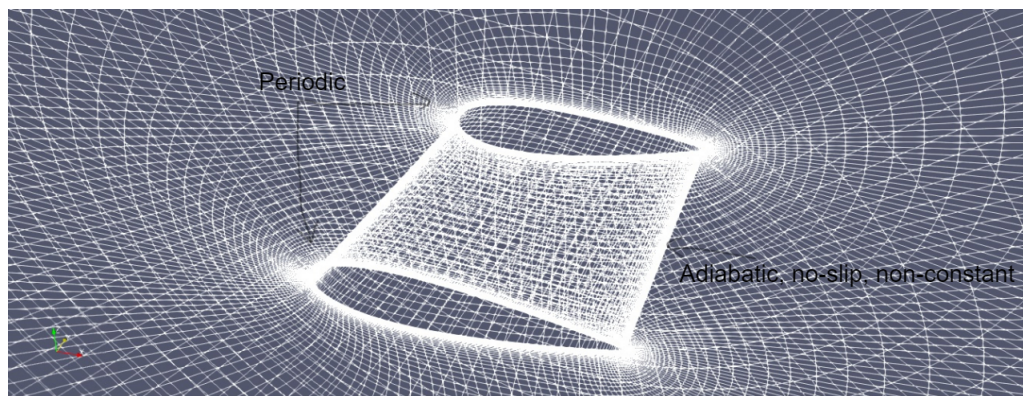
(b) Airfoil mesh

Figure 3.1: Mesh details, given by 3.1(a) the overall mesh view and 3.1(b) the zoom-in airfoil view

As can be observed, there are four major boundary conditions that are implemented, namely:

1. An ***adiabatic, no-slip*** boundary were applied to the airfoil walls, setting the heat flux generated at the walls to zero.
2. A ***non-constant*** wall temperature boundary condition is imposed on the airfoil, as the flow is non-isothermal, and hence, the airfoil walls cannot impose an isothermal boundary condition.

3. The ***far-field*** boundary condition is imposed on the edges of the domain, where the freestream values of temperature, velocity, pressure and density are used.

4. The **inlet & outlet** boundary conditions are defined separately. While the inlet is taken to have a turbulent inflow, wherein the eddy viscosity (ν_t) is comparable to the molecular viscosity (ν) [14], the outlet has a pressure and temperature specified, which are 300 K and 101325 Pa respectively.

5. The ***periodic*** boundary condition is applied to the airfoil in the spanwise direction, in order to ensure that the flow field remains periodic throughout the span. The boundaries that are indicated by 'Sym' denote the boundaries of the periodic boundary condition.

Another set of markers are used to indicate where the flow properties are extracted from for plotting purposes, as the 'Airfoil' keyword indicates. This is also used to monitor the residuals of the parameters used for post-processing the results.

Mesh settings
The mesh settings are first described by the mesh setup as shown in Figure 3.1. The mesh that was used in this case was the same as that from Molina et. al. [12].

From sub-figure 3.1(a), it can be seen that the mesh follows the pattern of being extremely refined at the airfoil, while becoming progressively coarser as one proceeds away from the airfoil. The mesh consists of hexahedral elements, with the mesh characteristics shown in Table 3.1.

Mesh Quality Metric	Minimum	Maximum
Orthogonality Angle (°)	75.2797	89.9989
CV Face Area Aspect Ratio	1.0474	1555.98
CV Sub-Volume Ratio	1.00268	1.70419

Table 3.1: Mesh quality metrics

As one can observe from Table 3.1, the orthogonality of the mesh elements is slightly compromised, from the point of view of having the minimum angle to be farther away from the desired value of $90°$. The maximum aspect ratio can be kept well above unity, given the fact that the attached part of the flow is resolved by RANS, which would require a coarser mesh compared to the detached flow region which is resolved by LES. This contributes to the high aspect ratio in this case.

The grid resolution is made in such a way to ensure that $y+ = 1$ everywhere. This is indicated by the presence of inflation layers near the walls of the airfoil, that causes an increase in the resolution of the mesh. The mesh follows an O-grid orientation, with gradual inflation being applied to the mesh elements as one proceeds towards the far-field. The far-field domain extends for about $20c$ (where c is the chord length) from the airfoil surface, which sufficiently far enough to ensure that there are no wave reflections.

Furthermore, the presence of a strong spanwise computational domain, as pointed out by Garbaruk et. al. [10] is taken into account. This has to be taken into account because of the fact that the flow is highly separated, which requires the mesh to be quite resolved in the wake region. Therefore, keeping this in mind, the fine mesh is refined by taking twice the number of elements in the coarse mesh in the spanwise direction. Finally, the spanwise size is redefined to be $4c$, having a constant step size of $0.02c$. The time step used in this computation, as was found to be optimal from precursor studies in the literature [3], was therefore, taken to be the same as that used in the paper of Molina et. al. [12], which is $0.025c/U_\infty$.

From sub-figure 3.1(b), the airfoil surface is finely meshed across the span, which is in line with the fact that the flow field and the corresponding physical phenomena (such as boundary layer separation and vortex shedding) have to be accurately captured.

3.1.2. Freestream settings

Before moving onto the results section, it is important to specify the freestream conditions of the flow, which are defined by Table 3.2.

Property	Value
Reynolds number (Re)	2.7×10^5
Chord length (c)	$1 \ m$
Angle of attack (AoA)	$60°$
Freestream Mach number (M_∞)	0.1
Freestream streamwise turbulence intensity (l_u)	0.6%

Table 3.2: Freestream properties of the flow

3.1.3. Flow parameters specific to SU2

The results obtained in this section are obtained by using an unsteady CFL of 5 and a time step (Δt) of 0.000864 s. The reason for choosing this CFL is because it was observed that for higher CFL values, the simulation did not converge upto the halfway mark of the tolerance (of the order of 10^{-14}), while the simulation time had to be compromised in the case of lower CFL numbers. This can be observed from the residuals obtained for each case, as can be seen in Figure 3.2.

```
+----------------------------------------------------------------+
|   Time_Iter|  Outer_Iter|  Inner_Iter|     rms[Rho]|   rms[RhoE]|
+----------------------------------------------------------------+
|        1496|           0|           0|    -4.650576|    0.703642|
|        1496|           0|           1|    -4.680437|    0.673398|
|        1496|           0|           2|    -4.710237|    0.643248|
|        1496|           0|           3|    -4.739994|    0.613149|
|        1496|           0|           4|    -4.769748|    0.583040|
|        1496|           0|           5|    -4.799503|    0.552904|
|        1496|           0|           6|    -4.829284|    0.522710|
|        1496|           0|           7|    -4.859053|    0.492516|
|        1496|           0|           8|    -4.888830|    0.462297|
|        1496|           0|           9|    -4.918585|    0.432107|
```

(a) CFL =1

```
+----------------------------------------------------------------+
|   Time_Iter|  Outer_Iter|  Inner_Iter|     rms[Rho]|   rms[RhoE]|
+----------------------------------------------------------------+
|        1496|           0|           0|    -4.603478|    1.246033|
|        1496|           0|           1|    -4.528772|    1.288679|
|        1496|           0|           2|    -4.640613|    1.227258|
|        1496|           0|           3|    -4.602203|    1.264503|
|        1496|           0|           4|    -4.582693|    1.265819|
|        1496|           0|           5|    -4.711287|    1.217329|
|        1496|           0|           6|    -4.591183|    1.274504|
|        1496|           0|           7|    -4.645431|    1.237266|
|        1496|           0|           8|    -4.683853|    1.233148|
|        1496|           0|           9|    -4.588651|    1.269120|
```

(b) CFL = 10

Figure 3.2: RMS residuals of density for different CFL numbers

As can be observed from Figure 3.2, it can be observed that the residuals do not reach a tolerance limit of even 10^{-5}, which is two orders of magnitude higher than at least half the value that is provided as an input for the limit of residual tolerance (10^{-14}). The reason for taking residuals of the order of 10^{-7} is because of general CFD guidelines. According to this, a change in the solution between 10^{-6} and 10^{-7} is negligible. Therefore, neither the values of 1 or 10 would be sufficient. It is to be noted that the reason 1496 iterations were taken into consideration was because of the fact that the residuals from later outer iterations did not go beyond the values predicted for this outer iteration. Therefore, it was deemed not necessary to provide information for higher iterations for these two CFL numbers.

In the case of CFL = 5.0, the number of inner iterations does improve the convergence of the solution by reaching a value of at least half the tolerance value. In the context of DDES simulations, given the stochastic nature of the solution, as will be shown in later simulations, was considered sufficient. Furthermore, from the guidelines mentioned in the DESider project [14], it was known that having 80 convective time units of an initial transient solution can be expected. Since 1496 outer time iterations correspond to about 45 CTUs, it would be necessary to consider a greater number of outer iterations before the transient nature of the solution is not present in the solution. For a CFL of 5.0, it was found that this transient nature was less prominent even for 45 convective time units (CTUs). Hence, this CFL was chosen for the rest of the analysis.

3.1.4. Numerical schemes

The numerical scheme that was involved in this study was an SLAU, 2nd order scheme, the working of which has been explained in some detail in Chapter 2 on the Literature Study. The numerical schemes in space and time are elaborated as follows.

Spatial discretization

The spatial discretization is performed by using a 2nd order solver of an upwind scheme method that is a low Mach number variant of the traditional Roe's scheme [26] that involves splitting the pressure fluxes that interpolate cell properties by using an upwind scheme, called the advection upstream splitting method (AUSM). This low Mach number variant, called the simple low-dissipation AUSM (SLAU), provides additional correction factors for the pressure flux, that take account for the numerical dissipation that occurs at such flow regimes, as explained by Shima et al. [27]. This is described mathematically by Equations 3.3.

$$\tilde{p} = \frac{p^+ + p^-}{2} + \frac{\beta^+ - \beta^-}{2}(p^+ - p^-) + f_p \cdot (\beta^+ + \beta^- - 1)\frac{p^+ + p^-}{2} \tag{3.3}$$

Where p is the pressure flux, β is the van Leer factor, and f_p is a non-dimensional function that depends on Mach number, which is used to control numerical dissipation in the AUSM scheme. The discretization stencil is defined in such a way that quantities calculated in the cell ahead of the ith cell are denoted by the $+$ subscript, while the quantities calculated in the cell behind the ith cell are denoted by the $-$ subscript.

In addition to this, the numerical blending of Travin and Shur (NTS) low dissipation scheme [54] was used in tandem with the SLAU2 scheme. This is because of the fact that this scheme provides a blending function that provides a additional theoretical backing to allow the switching between an upwind scheme and a central differencing scheme. This is represented in Equation 3.4.

$$F_{i+1/2} = (1 - \phi)F_{central,i+1/2} + \phi F_{upwind,i+1/2} \tag{3.4}$$

Where F is any inviscid flux, that can correspond to multiple quantities, such as density, pressure, velocity and so on, and ϕ is an empirical blending function. The subscripts 'central' and 'upwind' signify the fact that the central scheme flux value is used in that region (a fourth order scheme, for example), while the upwind scheme flux value is used in that region (third/fifth order scheme, for example), respectively. This switch from the central scheme to the upwind scheme and vice-versa, is activated by the blending function. This scheme activates RANS like behaviour in regions where the blending function is unity, which allows for stability in the coarser mesh regions, whereas it activates LES like behaviour in regions where refinement occurs where the blending function is not unity. Therefore, in such regions, the smaller turbulence length scales are resolved, while activating an almost central differencing scheme.

Temporal discretization

The temporal discretization has been performed by using a second order time stepping scheme, that incorporates a dual time stepping scheme. First described by Jameson [55], this scheme solves the Navier-Stokes equation by introducing an additional time step called the pseudo time step, that avoid any form of time step restriction. This is simply because of the fact that dual

time stepping is inherently implicit. The unsteady flow is essentially divided into multiple smaller pseudo steady state solutions, whose overall effect is to solve the problem by using the pseudo time step as the local time step. The unsteadiness in the flow is considered to be an external forcing term in solving the Navier-Stokes equation, as shown in Equation 3.5.

$$\frac{\partial \mathbf{q}}{\partial t^*} + \mathcal{N}(\mathbf{q}) = \mathcal{S}(\mathbf{q}) \tag{3.5}$$

Where $\mathbf{q}$ is the solution vector corresponding to the density and momentum flux vector $(\rho, \rho u, \rho v, \rho w)^T$ and $\mathcal{N}$ is the Navier-Stokes operator. S is the source term that accounts for the unsteadiness in the flow for each pseudo time step. The $*$ over the temporal derivative implies that the solution is obtained in pseudo time. This source term can be calculated using multiple iterative methods, and in the case of the given solver, it is calculated using a second order method.

One of the biggest advantages of the dual-time stepping scheme is to provide the time step as a function of the local time scales, irrespective of the spatial discretization. This is especially advantageous for the flow problem taken into consideration, given that a hybrid RANS/LES method would solve multiple turbulent structures in the RANS region that would have to be accurately captured. Therefore, it is imperative to have a good temporal resolution in such regions.

3.1.5. Linear solver
In order to solve the second order Navier-Stokes equation for each time step, there is a need to solve these equations iteratively, which can be performed using different methods. Both explicit and implicit methods can be used for this purpose, and in this case, the Incomplete Lower Upper factorization (ILU) method is used for that purpose. Although this method is quite computationally expensive, it is also quite effective from the point of view of obtaining results for this flow case, given that URANS is used for the attached flow region, while LES: which is the computationally more expensive method, can be optimized by using this linear solver, which only requires storage of the parameter values on the diagonals, thus making it quite memory effective [56].

3.1.6. RANS
There are multiple turbulence models that could be used along with the DDES approach, as described in Section 2.5.1 of the literature study. In this case, the Spalart-Allmaras model [46] was used. The advantages of the predecessor of this method, i.e., the Detached Eddy Simulation (DES), are well-documented in the literature for various aerodynamic flows, including detached flows [8]. This has been found to provide better results in comparison to RANS: in fact, the accuracy is at par with that of LES, at a lower computational cost than LES [37]. However, some of the well-known issues of DES, including modified stress depletion (MSD) and grid induced separation (GIS) are well known. These issues have been found to cause excess eddy viscosity to be estimated in some cases, while estimating lesser in some others [37]. Therefore, the DDES approach is used in tandem with sub-grid scale models that allow for a better understanding of the flow physics to avoid those issues.

One comment that could be made regarding the turbulence model that are used in the simulation is that the use of a different turbulence model such as the two-equation SST model, as described by Menter [33]. The current study uses the one-equation Spalart-Allmaras model, which has been proved to provide good results for external aerodynamic flows, which included certain cases of separated flows [46]. However, in the context of DDES simulations, it has been proved in the literature that the two methods perform very similarly [57], and has been investigated in the past for the case of unsteady flow past tandem cylinders [58]. This was further vindicated by Strelets [8] in his paper on massively separated flows over an airfoil. Therefore, the SA model has been used for the simulations in this case.

3.1.7. LES
As described in sub-section 2.5.6, there are two major different kinds of turbulence models for LES (called hybrid SGS models) available in SU2 for the purpose of resolving the flow field in

the case of shear layer flows. In the current flow problem, the presence of shear layer instabilities does, indeed, vindicate the requirement of such a model. There are multiple such models available in the literature, and specifically for DDES applications in SU2, these can be classified into four different categories depending on the mathematical model, which are summarized as follows:

1. DES based on the maximum size of the grid, as defined by Spalart [9].
2. DDES defined on the maximum size of the grid ($\Delta = \Delta_{max}$): based on the transition from RANS to LES based on the maximum grid size (denoted by Δ_{max}), as defined by Spalart [46].
3. DDES defined on a vorticity-based length scale ($\Delta = \Delta_{\omega}$), as defined by Deck [42].
4. DDES defined on a shear-layer adapted (SLA) SGS, otherwise called enhanced DDES (EDDES), as defined by Shur [59].

In this case, the shear layer adapted sub-grid scale (SLA-SGS) model was used. The reason for the use of this model is because of the fact that the flow physics, as described by Lacagnina et al. [5], does contain K-H instabilities, as well as shear layer roll-up that accompanies vortex shedding and the presence of a dominant wake region. Therefore, the use of such a model is indeed, justified.

3.2. Calculation of sampling frequency and time step

The sampling frequency that has to be calculated for both the flow-field analysis, as well as for a basic analysis of acoustics, which has been attempted once the flow field analysis was completed. The sampling frequency can further be used to calculate the time step. This has been attempted by defining the grid size of the cell that is present in the region where the vortex shedding has occurred. A description of this is given by Figure 3.3. It is to be noted that the cell that was used in this case as a preliminary estimate was obtained using a 2D slice from the mesh. Although this is not a very accurate estimation of the time step and the corresponding sampling frequency, given that the mesh size may vary even a few chord lengths away from the location where the calculations were performed, it is still useful to provide an initial estimate of the time step. It is also useful to compare the results with the time step obtained from the frequency of vortex shedding.

The sampling frequency, and the corresponding time step, are calculated in the following steps:

1. Setting the correct steady state CFL number.
2. Calculating the characteristic length of the grid.
3. Calculating the necessary time step for the sampling frequency.

The cell is chosen to be just downstream of the suction side of the airfoil, where the boundary layer has separated due to stall effects. This is done in order to apply a correct steady state CFL number, which provides an indication about the amount of flow information that is convected between two cells. It is advisable to keep the parameter as low as possible, so that the errors that would propagate between cells would be kept to the minimum. For the calculations performed in this section, the steady state CFL number is taken to be unity. This is because of the fact that the calculations in this section are preliminary, and can be re-defined using a higher CFL at a later stage. And lastly, the values of the grid size was obtained by using the ruler function in Paraview, which was also used as the tool for visualization purposes in later chapters.
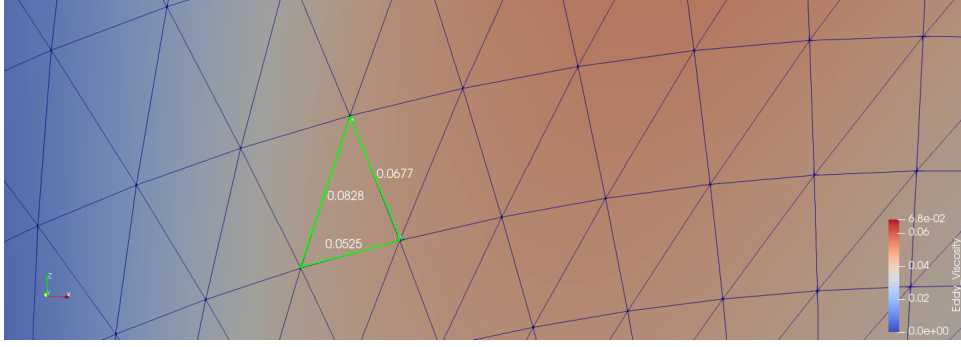
Figure 3.3: Cell just downstream of suction surface of airfoil with dimensions

As can be seen in Figure 3.3, the edge lengths of the grid cell that is downstream of the suction side is given by 0.0828 m, 0.0627 m and 0.0525 m respectively (when measured in the clockwise orientation).

The next step in this process is to calculate the characteristic length of the grid to be used for the calculation of the time step from the steady state CFL number. This is done in the following four ways, namely:

1. Preliminary estimate by using the maximum length using the LES grid size.
2. Corrected estimate of grid size using DES.
3. Estimate by using a grid size defined by DDES.
4. Estimation by using the range of frequencies where vortex shedding is predominant in stalled airfoils.

Each strategy and the corresponding calculations are elaborated in the following subsections.

3.2.1. By using maximum length of grid cell (LES)

The first strategy that is used to calculate the sampling frequency (and the corresponding time step) is that the maximum length of the grid is taken to be the grid size for the mesh. Hence, if Δ_x, Δ_y and Δ_z are the three length scales (assuming that the vorticity vector is aligned with the Y-axis, and given that the discretization is performed in the X-Z plane alone, so Δ_y and Δ_z correspond to the dimensions of a single cell in the X-Z plane). The characteristic length of the grid is obtained by using Equations 2.11 and 2.12 respectively.

From this calculation, the grid size has been found to be around 0.0858 m. This is further used to obtain the time step necessary for the calculation, which is found from the steady state CFL number (CFL_{conv}). Taking $CFL_{conv} = 1$, we get $\Delta t = 0.002386s$. Corresponding to this time step, the Nyquist frequency and the corresponding sampling frequency calculated based on the Nyquist's criteria ($f_{sampling} \geq 2 \times f_{Nyquist}$) are 1.0485 and 2.097 kHz respectively.

Although this is a good estimation of the grid size, it is important to note that the LES approach was found to be unable to sufficiently resolve the largest eddies, which were observed from the flow field output obtained from Paraview (the largest eddies that can be resolved from LES are of the order of the maximum grid size itself). This was found from the findings of the results obtained from the time step used. Therefore, this approach was ruled out.

3.2.2. Using DES consideration

The second strategy that is used to calculate the sampling frequency is by using the DES length scale, which is defined as given by Equation 3.6. This approach requires the use of the distance of the given element from the wall (d), as well as the size of the mesh element (Δ).

$$\tilde{d}_{DES} = \min(d, C_{DES}\Delta) \tag{3.6}$$

The distance from the nearest wall was found from the mesh using the Ruler tool in Paraview, as shown in Figure 3.4. The reason to take the highlighted cell is due to the fact that the wall

distance taken into account where the presence of the wake has the maximum eddy viscosity, while also being the region where LES can be applied. Furthermore, this can also be a test for how DES works in such flow regions.
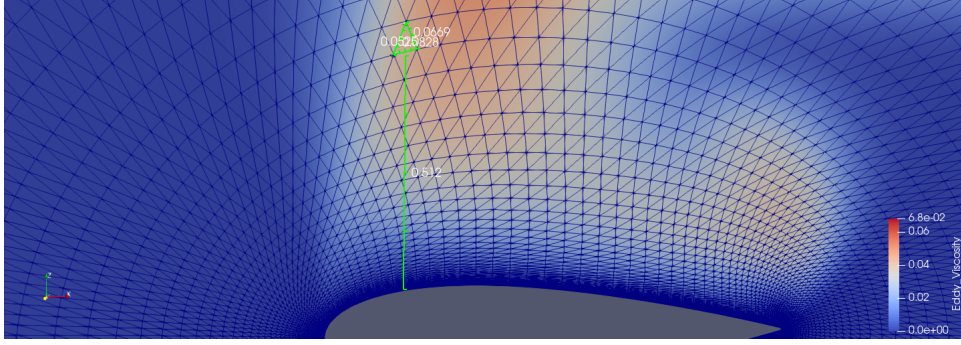
Figure 3.4: Cell normal distance

Using the parameters defined in the formulation for the grid spacing using the DES approach as has been provided earlier in Equation 2.12, the parameters $C_{DES} = 0.65$, $d = 0.512m$ and $\Delta = 0.0858m$ are plugged into Equation 3.6. One then gets the grid size as $\tilde{d}_{DES} = 0.05382m$. The corresponding time step for a $CFL_{conv} = 1$ is found to be $1.55 \times 10^{-3}s$. The corresponding Nyquist frequency that can be resolved using this approach is found to be 645.16 Hz, which although lies in the range of frequencies for vortex shedding, does not provide information about the higher frequencies (upto 1000 Hz). Therefore, this method is not used.

3.2.3. Using DDES formulation

The DDES formulation to obtain the grid size is calculated by using the DDES grid size calculation, first provided by Spalart et al. [46]. This provides a relation between the characteristic length scale of DDES and the wall distance, allowing to define the boundary layers where the transition from RANS to LES would be taking place. The relationship is given by Equation 2.13.

The empirical function f_d is calculated by using the formulation given by Spalart as shown in Equation 2.14.

From the paper of Spalart [46], it is mentioned that when using the S-A turbulence model, the numerator of Equation 2.14 can be approximated as as $\tilde{\nu}$. From the contours in Figure 3.4, it can be approximated that $\tilde{\nu} = 0.005m^2/s$. The velocity gradient has been approximated from the skin friction coefficient magnitude (C_f) as given by Equation 3.7 and by using Newton's law of viscosity that relates the wall shear stress and the velocity gradient.

$$\frac{\partial u}{\partial y} = \frac{C_f \times \frac{1}{2}\rho U_\infty^2}{\mu} = 0.2 \tag{3.7}$$

The cell that is used for the purpose of calculating the velocity gradient is the same as given in Figure 3.4. The empirical function f_d at that location is found out to be calculated by taking $\tilde{\nu} \approx 0.005$ in that cell, $d = 0.512268m$, $U_{i,j} = 0.2s^{-1}$ (based on Equation 3.7) and $k = 0.4$. From these values, $f_d = 0.596$.

Therefore, from the above parameters, the value of the grid size is calculated by using Equation 2.14 as shown in Equation 3.8.

$$\tilde{d}_{DDES} = 0.512268 - 0.596 \max(0, 0.512268 - 0.65 \times 0.517768) = 0.4054\,m. \tag{3.8}$$

From Figure 3.4, it can be observed that the values of d and Δ are 0.512 m and 0.0828 m respectively. Plugging these values into Equation 2.14, we get $\tilde{d}_{DDES} = 0.4054m$. Corresponding to this length scale and $CFL_{conv} = 1$, we get a time step of $\Delta t = 0.01168\,s$.

The disadvantage of using this method is the fact that on calculating the range of frequencies from the time step, one obtains that the highest frequency range that this time step can resolve

is in the order of around 856 Hz. Although this is in the range of vortex shedding frequencies in deep stalled airfoils (given that the vortex shedding frequency in such cases can be up to 1000 Hz), it might not be sufficient in the higher frequency range. Therefore, this method cannot be used as well.

3.2.4. Using range of frequencies of vortex shedding

From the literature, as reported from the experimental results obtained by Moreau et. al. [19], it has been found that the range of frequencies that correspond to the vortex shedding of an airfoil in deep stall are in the range of 100 - 1000 Hz for an airfoil having a chord length of 0.15 m. Given that there is a direct correlation between the frequency range obtained from the literature and the chord length [5], it is important to take into account the fact that the smaller vortices are in the higher range of frequencies, corresponding to their smaller characteristic length scales. These vortices are invariably linked to the periodic vortex shedding associated with the shedding noise.

On that note, the following observations have been made with regards to the sampling frequency and the time step that is to be used for the calculations:

1. The time step of 0.000864 s has been calculated keeping in mind the fact that 100 times the time step is equivalent to 3 convective time units. This is calculated keeping in mind the frequency limit of vortex shedding as well, which was in the range of 1000-1200 Hz when calculated using this time step. Also, this time step was simply calculated by taking into account the guidelines provided by Shur [7]. Taking an initial estimate of $CFL_{conv} = 1$ and $U_\infty = 34.7224\ m/s$, we obtain that the grid size is around 0.03 m. Taking the freestream temperature of the simulation to be around 300 K, the largest frequency that can be resolved using this grid size is obtained to be around 11 kHz. This is an order of magnitude higher than what is required. Therefore, it can be afforded to be a bit less conservative as far as the CFL_{conv} is concerned, and one can take higher values if required.

2. The unsteady CFL (abbreviated as CFL_{unst} henceforth) is an indication of how the information travels between two cells in the mesh from one time step to the next. However, because one is using an implicit, density-based solver, the unsteady CFL would not affect the final solution.

3. The steady state CFL (abbreviated as CFL_{conv}) is an indication of how information travels between two cells for each steady state solution. This is defined as per the formulation given by Palacio [60]. In SU2, this is provided by the CFL of the finest grid cell. In the given case, it is useful to note that this value is taken to be 5.0 for this simulation, based on the reasoning given in Chapter 3. This has been taken into account keeping in mind that the residuals of density, that are used as an indicator for the convergence criteria, do not reach the desired levels with a high amount of accuracy (the RMS residuals of density are to be made as low as possible, of the order of about 10^{-6} or 10^{-7}), in accordance with standard engineering principles, that the residual value must fall to about 10^{-6} times the original value of the residual, whose value may start from the order of unity. Furthermore, being extremely conservative from the temporal point of view is also not desirable, taking into account the amount of flow time that is needed to obtain a steady state solution. Therefore, keeping a balance between these two factors, the steady state CFL value has been chosen.

4. From the DESider project [14], it can be observed that there were at least 4800-5200 convective units of time (defined as $(U_\infty/c) * t$) that were required for obtaining a steady state solution of the unsteady simulation. For the given parameters of the simulation, the flow time that is required in order to obtain the steady state flow solution corresponding to these convective time units was between 115.2 s and 149.76 s. Therefore, keeping this in mind, the maximum flow time for the solution was set to be 150 s. The number of iterations that were required to obtain the flow solution were calculated to be a maximum of approximately 180000 to reach the flow time of 150 s.

5. The other flow parameters were kept the same, with the solution output written for 100 iterations until 4800 convective time units were reached, after which the solution was written for each iteration to obtain better clarity of the flow solution.

4

Results & Discussion

4.1. RANS results

4.1.1. Results from RANS 1st order

The results for the pressure field, eddy viscosity and Mach number contours are described in this section.
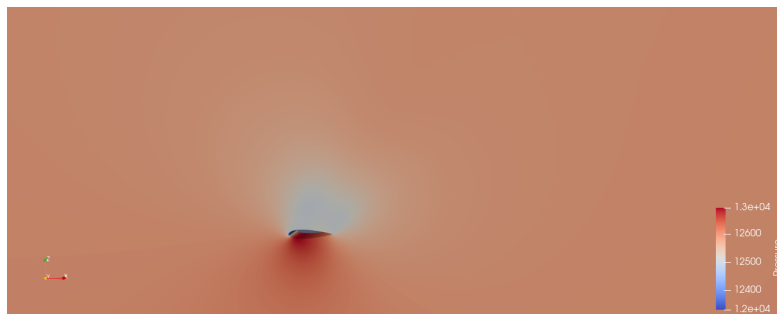
Figure 4.1: Pressure contours of the RANS 1st order

From Figure 4.1, it can be clearly seen that there are two distinct suction and pressure sides on the airfoil. This is understood, as the suction side is where the presence of a large separation region can be observed, while the boundary layer is completely attached on the pressure side. Because of this, there is a favourable pressure gradient that is caused due to the curvature effects, that cause an increase in the static pressure. Therefore, there is a visible presence of not only separation on the suction side of the airfoil, but also that of boundary layer attachment on the pressure side throughout the time period of the simulation.
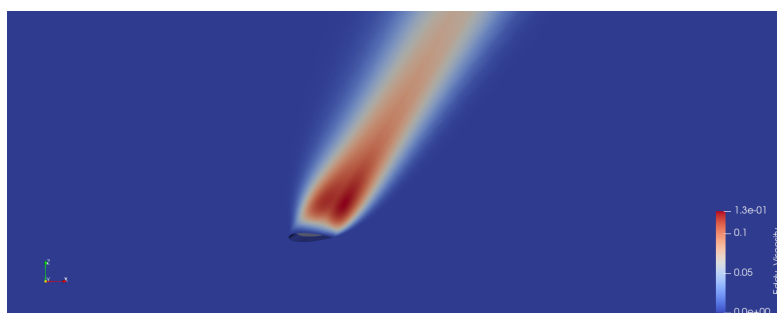
Figure 4.2: Eddy viscosity contours of the RANS 1st order

The reason why eddy viscosity is plotted is because of the fact that there is a need to observe how far the vortex shedding in the wake takes place without the effect of viscous dissipation

taking over and dissipating the vortices. From Figure 4.2, it can be concluded that the eddy viscosity shows an expected trend of being the highest just downstream of the airfoil, due to the presence of extremely high pressure gradients, boundary layer separation and reversed flow. This is also shown to have a progressively reduced effect as one proceeds downstream. In order to check whether this is physically valid or not, a good indicator of this would be to find the variation of the turbulence kinetic energy with viscosity. This is because of the fact that the effects of turbulence die down due to viscous dissipation of the turbulent kinetic energy at the smallest length scales.
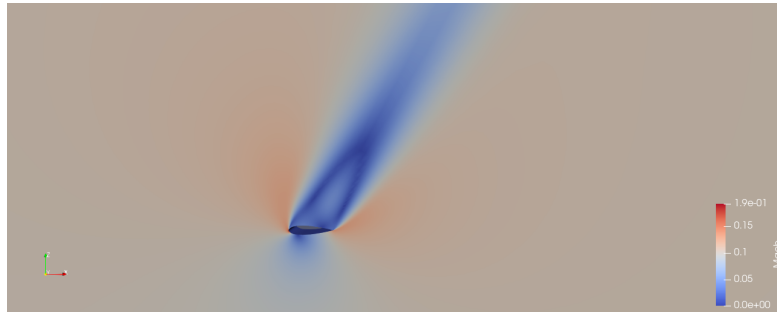
Figure 4.3: Mach number contours of the RANS 1st order

Figure 4.3 describes the variation of the Mach number in the domain around the airfoil. From this, it can be observed that the effects of a region of deep stall can be observed. This is because of the presence of deep stall in these regions, which causes the region in the suction side of the airfoil to have a different velocity contours in comparison to the other regions downstream of the flow. The recirculation region, however, cannot be completely ascertained from the suction side as well. This can be observed in both Figures 4.2 as well as 4.1. The suction side, however, has a separated boundary layer that experiences acceleration due to curvature effects of the airfoil, which is observed as the flow gradually moves from the leading edge to the trailing edge.

One major point of observation that is missing, from the point of view of the physical phenomena, that can be observed in these contours is the fact that the vortex shedding cannot be observed. This is due to two reasons, first, RANS is inherently a steady turbulence solver, which cannot be used to predict an unsteady, periodic and time-dependent phenomenon such as vortex shedding. This has also been observed in the unsteady RANS versions in the literature as well ([7], [8]). Second, using a first order scheme to discretize the Navier-Stokes equation is not very accurate as discretization errors would cause a compromise in the flow solution accuracy. The dispersion errors would also not be treated accurately, as the discretization stencil is not big enough to provide a sufficient interpolation of the flow solution in every grid cell.

Therefore, it would be wise to take into account the results obtained from a higher order RANS solver, such as the 2nd order solver, so that a better comparison can be made. This is performed in the next section.

4.1.2. Results from RANS 2nd order

As mentioned in the Introduction section, the RANS 2nd order solution is obtained by providing the converged RANS 1st order solution as an input, so that numerical errors (both discretization and dispersion) can be avoided as much as possible. The purpose of comparing the pressure, eddy viscosity and Mach number contours is to compare and contrast the flow physics that can be ascertained from both the numerical schemes critically, in order to provide a valid conclusion as to why using the RANS approach might not be useful to predict all the flow features of the current problem.
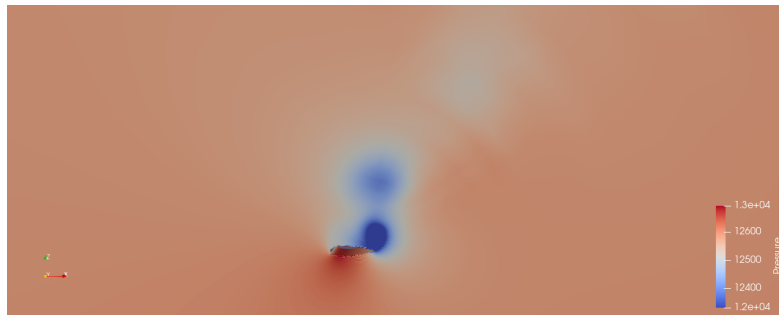
Figure 4.4: Pressure contours of the RANS 2nd order

From Figure 4.4, the pressure contours that are obtained from the solution reflect the presence of vortex shedding a bit, near the trailing edge, where the preliminary effects of vortex formation can be observed. However, as is the case with steady simulations, a periodic vortex shedding formation cannot be observed. Hence, one cannot obtain a complete description of vortex shedding, beyond a single period, in this case.
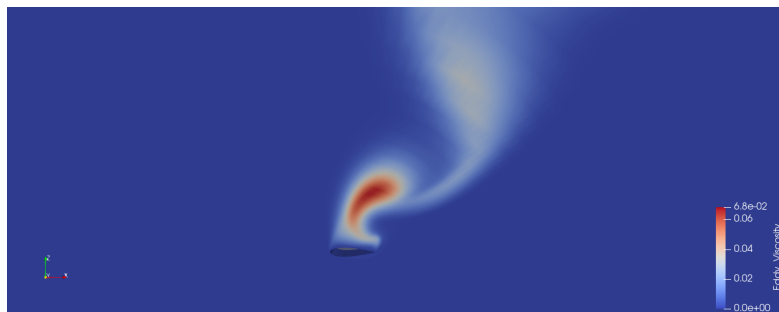
Figure 4.5: Eddy viscosity contours of the RANS 2nd order

From Figure 4.5, it can be observed that, in a similar manner to the pressure contours shown in Figure 4.4, the region of high turbulence and flow separation is the region with the highest eddy viscosity, as can be observed in the small, dark-red region just downstream of the suction side of the airfoil. This indicates the presence of deep stall, as was observed in the pressure contours as well in the wake near the suction side of the airfoil. There is once again, a slight hint of vortex shedding, as can be seen by a vortex roll-up. However, the periodic phenomenon of vortex shedding can, once again, not be observed, on account of the solution being a steady one in nature. Furthermore, the absence of the resolution of the smaller turbulent structures is also missing, which is a clear indication that the flow solution has been averaged out.
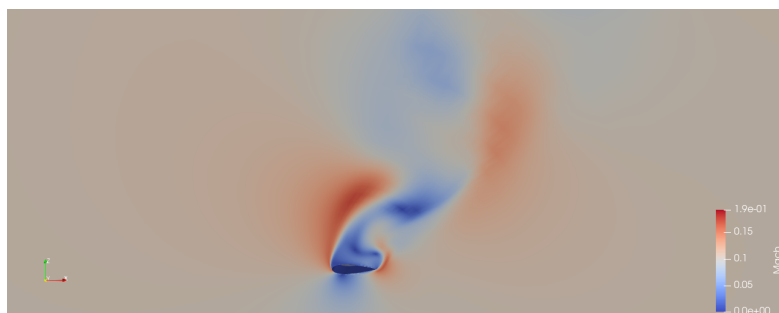
Figure 4.6: Mach number contours of the RANS 2nd order

From Figure 4.6, it can be observed that the Mach number contour follows a trend akin to that of the eddy viscosity contours shown in Figure 4.5. There is once, again, a hint of vortex shedding, as well as vortex roll-up, as can be observed in the downstream of the suction side of

the airfoil. There are areas of recirculation that can be observed just downstream of the airfoil on account of this vortex shedding, which justifies that the phenomenon can, indeed, be observed. However, there is a lack of periodicity for this vortex shedding beyond 2-3 periods.

It can be concluded that although the results from the RANS 2nd order solution have a greater accuracy in terms of obtaining the presence of the physical phenomenon of vortex shedding and an improved spatial accuracy, on account of an increased spatial accuracy of the 2nd order numerical scheme, the periodicity of vortex shedding is once again missing, on account of the steady nature of RANS. Therefore, there is a need to use an unsteady approach to resolve the flow field and accurately capture the flow physics, which is done by the DDES solver in the next section.

4.2. DDES results

In order to provide a greater insight into the unsteady flow physics that could not be obtained from the RANS solution in the detached flow regions, the DDES approach was used to obtain possibly improved results in this regard. This was obtained by using a 2nd order solver in both space and time, as has been described in detail in Chapter 3. The results of the DDES 2nd order are obtained by providing a converged RANS 2nd order solution as an input, so that the flow solver could work with an initial converged solution. This is to mitigate the numerical errors caused due to high adverse pressure gradients during separation of the boundary layer from the suction side of the airfoil.

In this section, the results obtained from the DDES 2nd order solver have been discussed. It is to be noted that since this is an unsteady simulation, all the results mentioned in this chapter are for the converged solution at the final time step.

The first step taken before these results are discussed is to plot the divergence of velocity contours in both the spanwise and the chordwise directions. The purpose of performing this step is to ensure that the use of a compressible solver is justified for the Mach number of 0.1, which is less than the general compressible flow regime of 0.3. This can be seen in the divergence of velocity plots, which is explained in Section 4.2.1.

4.2.1. Divergence of velocity contours

According to basic aerodynamic theory, the divergence of velocity is considered to be one of the criteria for deciding the compressibility of a fluid flow [20]. Therefore, this can be defined mathematically as shown in Equation 4.1.

$$\nabla \cdot \vec{V} = 0 \tag{4.1}$$

Therefore, the regions where the divergence of velocity is not zero would require the use of the compressible flow equations to be solved in order for them to provide the correct output. The theory behind this concept lies in the fact that the effects of compressibility would be determined by the presence of a non-zero sum total of the velocity gradients, which indicates that the flow has constant density. Thus, this would simply imply that there is no spatial variation of the density in the domain.

Spanwise direction

This section explains the variation of the divergence of velocity at various locations along the span of the airfoil. In this case, the divergence of the velocity is obtained for three spanwise locations, namely at $y/b = 0.25$, $y/b = 0.5$ and $y/b = 0.75$ respectively.

(a) $y/b = 0.25$ (b) $y/b = 0.5$ (c) $y/b = 0.75$
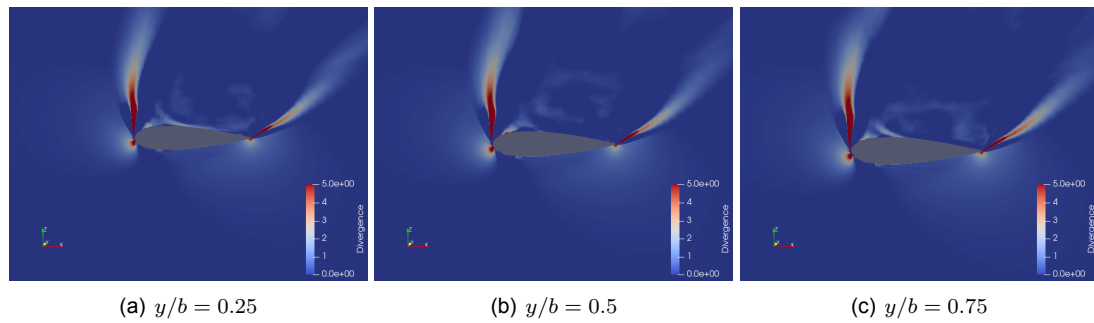
Figure 4.7: Variation of the divergence of velocity with span

From Figure 4.7, it can be observed that the divergence of velocity is non-zero in multiple regions (indicated by all colours apart from blue) around the airfoil on both the suction and pressure sides. The red regions are where the flow separates from the airfoil suction side. Therefore, these regions are compressible as the divergence of velocity is not zero. This can be seen in all the various spanwise locations.

Furthermore, there is a strong recirculation region that can be observed on the suction side, which also has an impact on the effects of compressibility along the spanwise direction. The compressible nature of the K-H instability is also justified with this analysis, as one of the effects of this instability is the change in local density. This would impact the divergence of velocity directly. Therefore, this is a useful indicator of the effect of the K-H instability on local density changes.

Chordwise direction
This sub-section describes the use of a compressible flow solver to describe the flow phenomenon that can be observed along the chordwise direction.

(a) $x/c = 0.1$ (b) $x/c = 0.25$

(c) $x/c = 0.75$ (d) $x/c = 0.98$
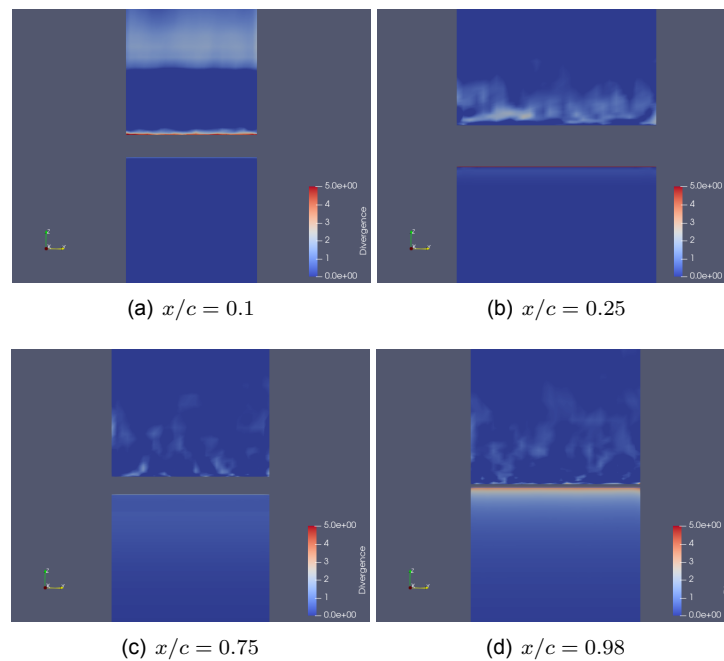
Figure 4.8: Variation of the divergence of velocity with chord

From Figure 4.8, it can be observed that at $x/c = 0.1$, the presence of the compressible boundary layer can still be observed on the suction side of the airfoil, as one can observe a very high non-zero divergence value. This can also be attributed to the fact that the boundary layer

starts to experience a very high pressure gradient, that can contribute to the high divergence as well.

At sections $x/c = 0.25$ and $x/c = 0.75$, it can clearly be seen that the boundary layer no longer remains attached with the suction side of the airfoil. The presence of non-zero divergence is because of the presence of the large recirculation region just downstream of the suction side of the airfoil. On the pressure side, as expected, the boundary layer remains attached, and therefore, the presence of a high divergence on the pressure side of the airfoil. Even at $x/c = 0.98$, one observes a semblance of boundary layer attachment on the pressure side of the airfoil, given the divergence value near the airfoil surface. Furthermore, the presence of the wake region on the suction side of the airfoil is also an indicator of the shear layer instabilities and the corresponding roll-up.

4.2.2. Initial results obtained from 10 inner iterations

Time history of DDES 2nd order results

The variation of the lift (C_l) and drag (C_d) coefficients with experimental data are shown in Figures 4.32 and 4.33 respectively. The results shown are for 10 inner iterations.
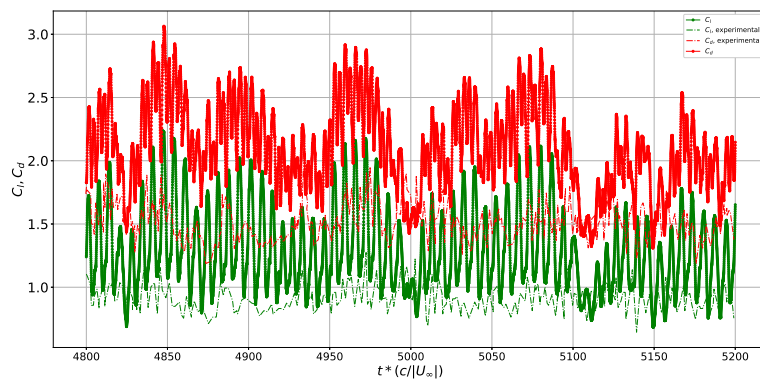
Figure 4.9: Variation of C_l and C_d vs. t^* for 10 inner iterations

From Figure 4.9, it can be clearly observed that the mean value of both C_l and C_d are over-predicted by values of 40.78% and 36.95% respectively (the mean values of C_l and C_d from experimental data are found to be approximately 1 and 1.54 respectively [6]), which is an indication that the solution has not sufficiently converged in order to provide a reasonable comparison with the experimental data. This also provides a secondary incentive to increase the number of inner iterations in order to obtain a better, converged solution.

Variation of power spectral density (PSD) of lift coefficient (C_l)

The variation of the PSD of C_l vs. Strouhal number (St) is given in comparison to experimental data in Figure 4.11. The PSD formula used to calculate the results presented in this section, as well as in other sections, are given in Appendix A. The time series plot for C_l versus t^* is given by Figure 4.10.
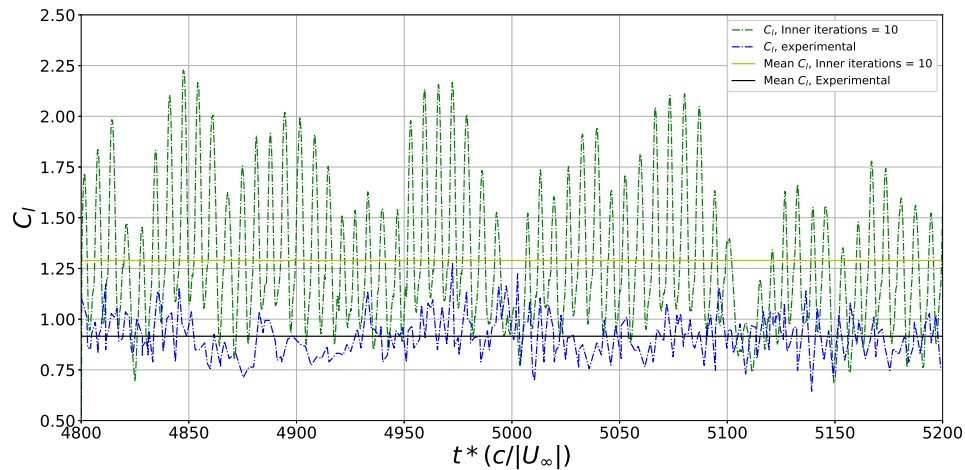
Figure 4.10: Comparison of C_l for 10 inner iterations with experimental data [6]

Figure 4.10 clearly shows that there is a very high over-prediction of C_l compared to the experimental data. This is quite evident from the mean value of C_l obtained from the simulation of 10 inner iterations, which over-predicts the mean value from the experimental data by 40.78%, which is a very high error. This can be accounted for two reasons. First, the residuals may not have converged entirely as a result of running the simulation for only 10 inner iterations. And second, the use of a narrow span (of a span of $1c$, where c is the chord length), can although allow for most of the turbulent structures to be captured according to Shur [7], cannot predict the spanwise effects of the C_l and C_d accurately, as was later shown by the DESider project [14] and Garbaruk's [10] findings.

As an additional comparison, the comparison of the PSD of C_l with Strouhal number (St) is then performed, as shown in Figure 4.11.
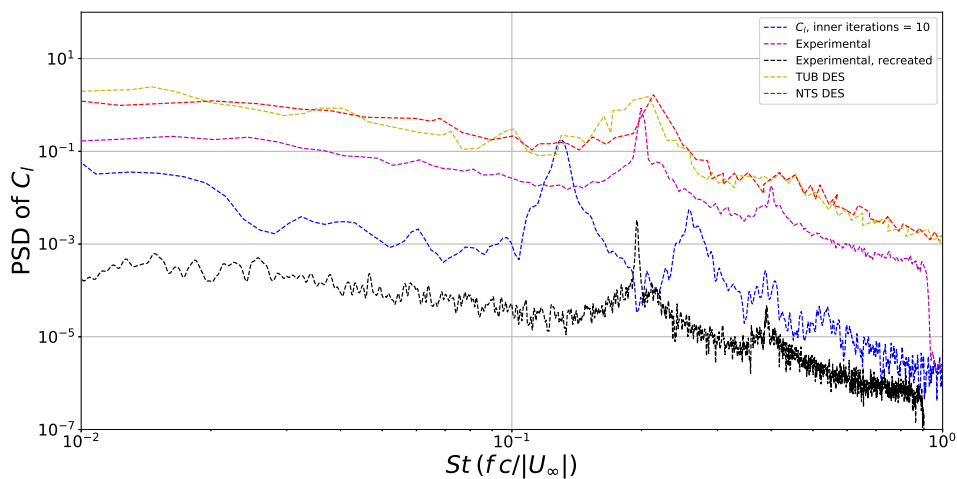
Figure 4.11: Comparison of results from experimental data [6], computational data [14] and SU2

From Figure 4.11, the following observations can be made:

- It can be observed that the results obtained from SU2 do not match very well with the experimental data in terms of predicting the peak for vortex shedding. As mentioned by Swalwell et. al. [6], it can be observed that the peak falls at a Strouhal number of 0.2.

This does not match very well with not only the re-created experimental data, but also the results obtained from the DES results obtained by TU Berlin and NTS respectively in the DESider project [14]. This implies that the flow physics is not sufficiently well predicted by having only 10 inner iterations.

- One major point of difference that can be observed in the two plots is that of the order of magnitude of the PSD value of C_l as seen in the plots for the DES versus the experimental data. This can be accounted for by the fact that the DES does not take into account the change in grid size transition from RANS to LES in the separation regions as smoothly as DDES. This results in an over-prediction of the eddy viscosity, and hence the corresponding drag and lift forces are over-predicted. This is, however, not seen in the case of the DDES results obtained from SU2, which actually provides a better comparison to the experimental data.

- The presence of the additional secondary peak in PSD after the first one, which is similar to the second shedding peak obtained by Moreau et al. [19] from experimental data. This indicates the presence of the corresponding harmonic to the vortex shedding frequency. This are a characteristic of the flow physics of airfoils in deep stall. The reason for the shift in the Strouhal peaks is because of the fact that the definition of St number as taken by the DES results would not have considered the wake length into account (given by $c \times \sin 60°$), which has also been described by Swalwell [6].

- In comparison to both the experimental and the DES results, it can be observed that there is the presence of excessive noise at the higher frequency range. This results in the presence of This can be attributed to the presence of numerical noise in the broadband range of frequencies. In order to avoid this, it is useful to consider increasing the number of inner iterations to improve the convergence of the solution.

From the results obtained for 10 inner iterations, it is clear that there is a need to improve the convergence of the solution, as there is a very high error in the lift and drag coefficients (>15% in each case), which is higher than the general scientific acceptance. Therefore, the next step would be to investigate a better convergence by introducing a greater number of inner iterations in the dual-time stepping solver.

4.2.3. DDES results with higher inner iterations

The purpose of increasing the number of inner iterations is to obtain a better converged solution. Therefore, there is an attempt made to improve the convergence of the solution, as well as the C_l and C_d coefficients. Thus, this section discusses the impact of the increase in the inner iterations on the convergence of the solution, as well as the impact on the time history of the relevant parameters. The flow field is first visualized in order to provide an insight into the flow physics of the problem. In the case of the current flow problem, it would be interesting to study the variation of the pressure, vorticity and the Q-criterion contours.

Pressure contours

The pressure contours that are obtained from the DDES simulation are shown in Figure 4.12. The purpose of showing the variation of these pressure contours is to provide the reader a physical sense as to how the presence of a massive wake region affects the flow solution downstream of the airfoil. It is to be noted that the pressure contours are obtained for 40 inner iterations.
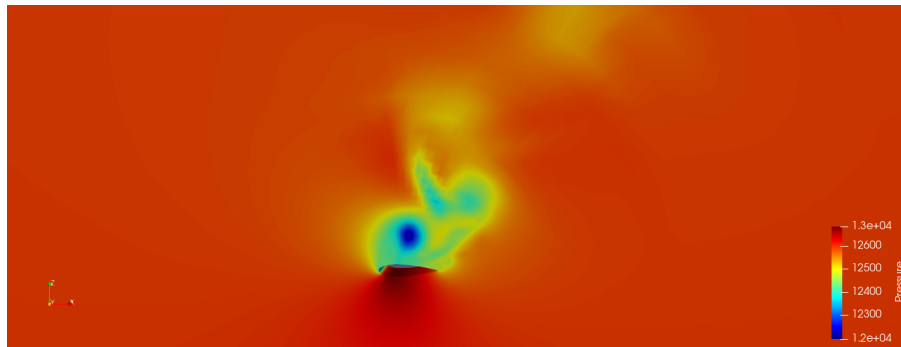
Figure 4.12: Pressure contours for the domain at the final time step

From Figure 4.12, one can observe the presence of vortex roll-up, which is a phenomenon that can be justified by the presence of vorticity in the spanwise direction as described in Section 4.2.3.

It can also be observed that there is a vortex formed at the leading edge, that convects towards the trailing edge of the airfoil at this time instant, in a region having a lower total pressure compared to the pressure side. This is one of the indicators of deep stall, which is that of a wake region consisting of vortex shedding. This wake region naturally has a lower pressure gradient, given the fact that there is no boundary layer in this region that can drive the flow by using a favourable pressure gradient. This is caused due to the fact that at this angle of attack, the recirculation region is located just downstream of the suction side. Therefore, this is indication of the presence of these vortical structures moving downstream and tilting towards the streamwise direction [5]. This can also be confirmed by the presence of the isosurfaces that provide a 3D visualization of these structures, as is explained later in Section 4.2.3.

Vorticity magnitude contours at various spanwise locations
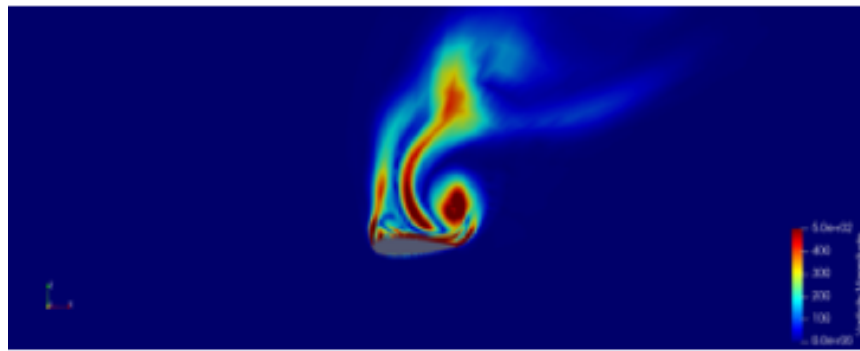
(a) $x/b = 0.25$
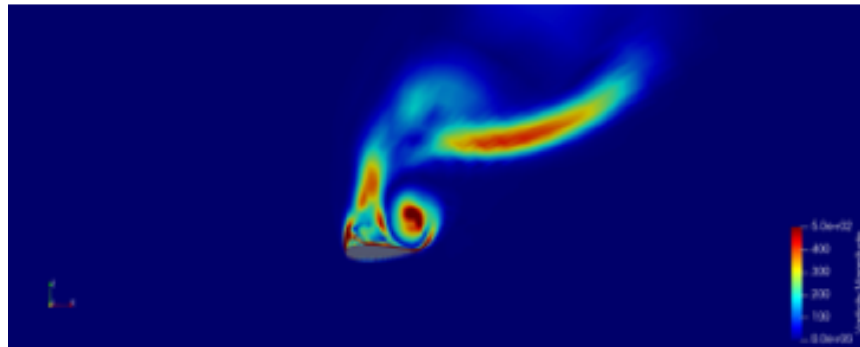
(b) $x/b = 0.5$
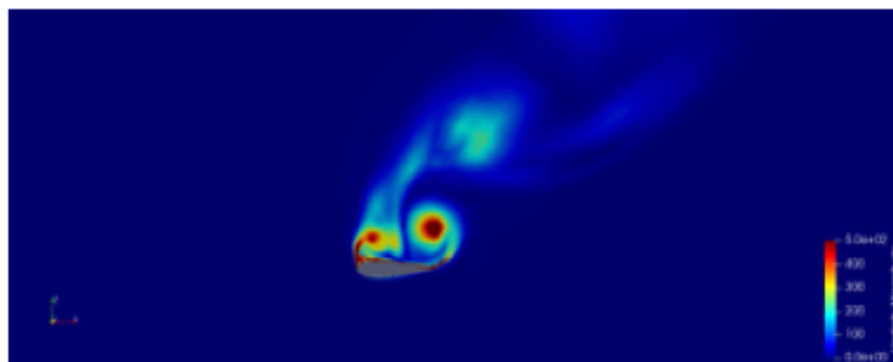
(c) $x/b = 0.75$

Figure 4.13: Vorticity contours for various spanwise locations

The purpose of having vorticity contours in the spanwise direction, is to provide a sense of how vortex roll-up occurs as the flow progresses in time, which is one of the characteristic features of the flow. From sub-figures 4.13(a), 4.13(b) and 4.13(c), it can be observed that the presence of vortex shedding can be justified by the regions where the vorticity magnitude is the highest.

Another observation that can be seen in the case of the vorticity contours is the evolution of the vortices differently at different spanwise locations for the same time instant. This can be attributed to the fact that despite the periodic boundary conditions imposed on the front and back wall faces, it can be noticed that the evolution of the flow is dictated by the change in the kind of turbulence model that is used for the purpose of obtaining the flow solution. This can be compared to the results obtained by Molina et. al. [12], as shown in Figure 4.14 in four different cases, one being using URANS, while the other three being in DDES.

(a) URANS

(b) Regular DDES

(c) Low-dissipation DDES

(d) Vorticity-based DDES
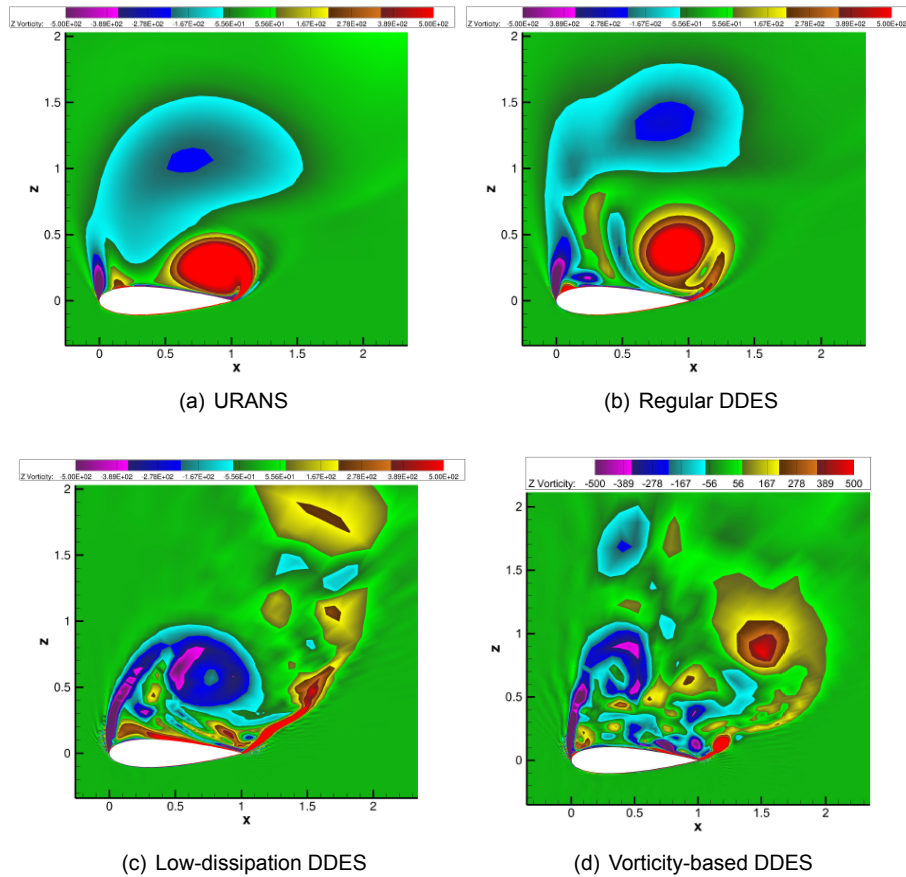
Figure 4.14: Vorticity contours based on different solution approaches (RANS on the left, DDES on the right) [12] at spanwise location $x/b = 0.363$

Furthermore, as these structures convect in the streamwise direction, they experience a greater tendency to roll-up together. This is because of the fact that the boundary layer closer to the trailing edge tends to re-attach with the suction side of the airfoil, which causes the vortical structures to come closer to each other. However, the presence of alternating periodic vortex shedding cannot be seen in the spanwise direction in this case, as can be seen in the presence of vortices located downstream of the airfoil. This has been further confirmed by Molina et. al. [12], whose reasoning can be used in this case as well: the coarser mesh, which was used for this particular simulation as well, is unable to capture the periodicity of vortex shedding accurately. Therefore, there is a need to improve this periodicity of vortex shedding by using a finer mesh.

Another way to test the periodicity as well as the roll-up of the vortices, this time in the spanwise direction, as has been observed by Lacagnina et. al. [5], is by observing the variation of the vorticity in the chordwise direction. This is described in further detail in Section 4.2.3.

Q-criterion contours at various spanwise locations
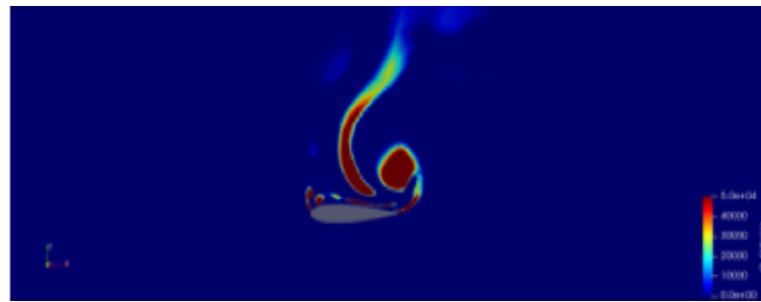
(a) $x/b = 0.25$
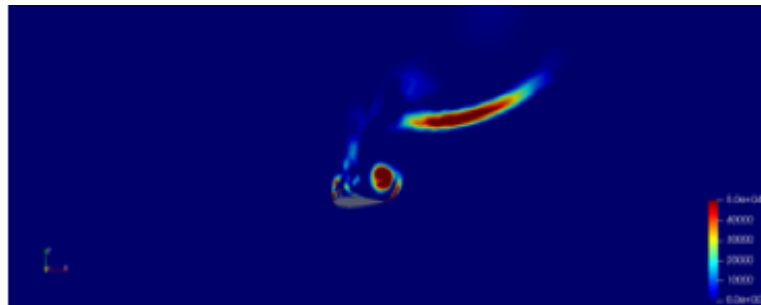
(b) $x/b = 0.5$
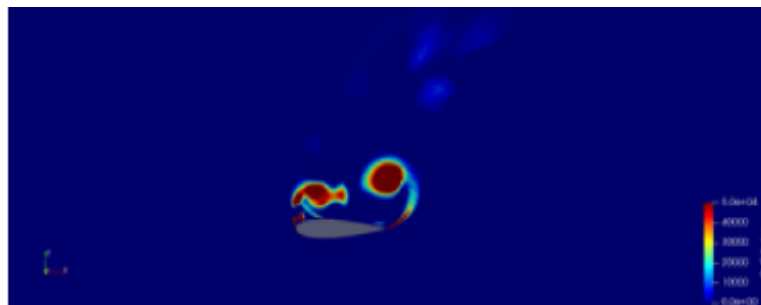
(c) $x/b = 0.75$

Figure 4.15: Q-criterion contours for various spanwise locations

The Q-criterion plots provide an insight into how various regions of non-zero vorticity are spread across different spanwise locations on the airfoil. From Figures 4.15(a), 4.15(b), 4.15(c), it can be observed that there are large regions where there is a presence of vorticity, as the Q-criterion plots confirm. These plots, however, do not indicate the presence of re-attachment of the boundary layer or the alternating nature of the vortices themselves. This is indicative of the fact that the Q-criterion only represents regions where vorticity is present, and more importantly, where the strain rate tensor is much higher than the vorticity tensor. Given that the strain rate tensor does not vary too much in the absence of vorticity in comparison to the regions vortices exist, this phenomena can hence be justified in that manner.

Furthermore, there are also smaller pockets of regions of much lower Q criterion values. Although, as mentioned by Baysal et. al. [61], the Q criterion is not the only sufficient parameter to determine the presence of a shear layer, as there are only three major phenomena occurring for the given Reynolds number as summarized by Lacagnina et al. [5], the only other major phenomena that can occur in this case would be that of shear layer instability, that generate unsteady pressure fluctuations near the airfoil surface. Therefore, this confirms the presence of shear layer instabilities as well.

Iso-surfaces of airfoil

Iso-surfaces depicting the variation of the Q-criterion in 3D space are a useful indicator of the expected physical phenomenon that can be visualized. This has described by Lacagnina [5] for noise generating mechanisms already, and can be divided into three major categories, namely:

1. Spanwise vortex roll-up.
2. Detached shear layer instabilities (such as K-H instabilities).
3. Shear layer flapping.

In order to confirm the presence of the first two physical processes, the iso-surfaces are plotted for Q-criterion as shown in Figure 4.16.
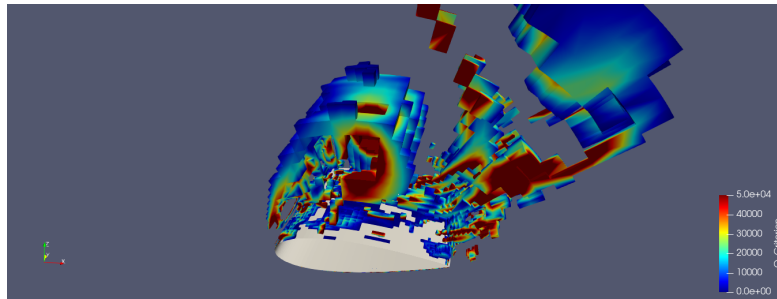
(a) Iso-surface of Q-criterion
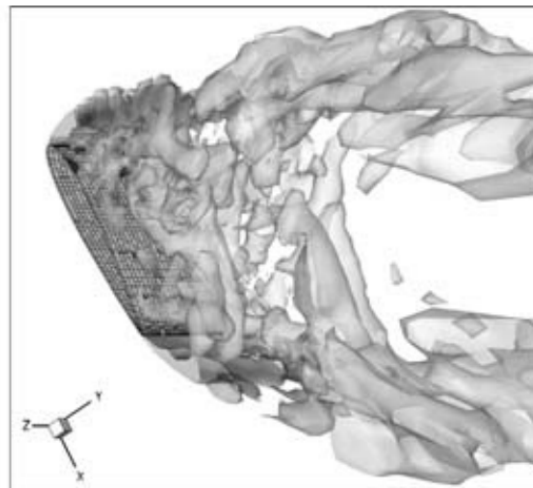
(b) Iso-surface observed by Yan

Figure 4.16: Iso-surfaces from (a) SU2 and (b) Yan et al. [3]

From sub-figure 4.16(a), it can be seen that there is indeed, spanwise vortex roll-up in the Y direction (spanwise direction). This is indicated by the presence of roller/rib vortical structures downstream of the airfoil, which was also observed by Yan [3] in sub-figure 4.16(b). There is also the presence of smaller structures near the suction side of the airfoil, as well as a few chord lengths away from the airfoil surface. This confirms that smaller structures are resolved by the LES mode of DDES as well, as this is activated outside the boundary layer, which is the detached region of the flow.

4.2.4. Comparison of time histories for different inner iterations
4.2.5. Impact on C_l and C_d

In order to provide an estimate of how much the C_l and C_d are affected by the increase in the number of inner iterations, a comparative study is done in order to take into account the effect of

the number of iterations on the C_l and C_d values. This is depicted by the plots in the upcoming sub-sections.

Variation of time varying C_l and C_d
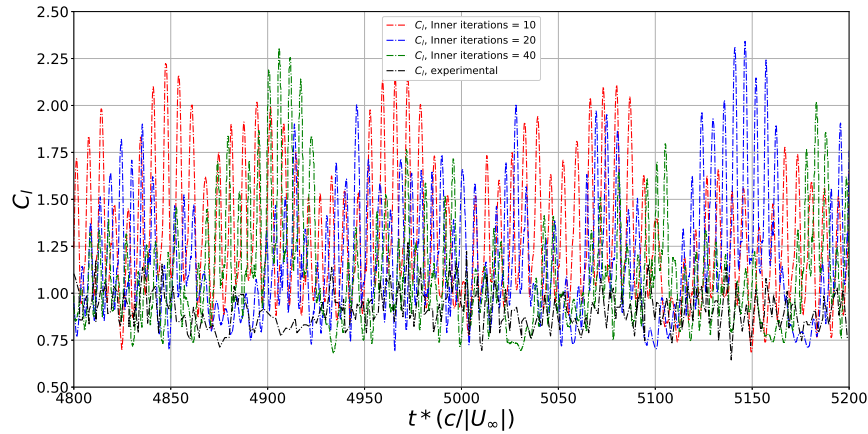
Figure 4.17: Variation of C_l for 10, 20 and 40 inner iterations
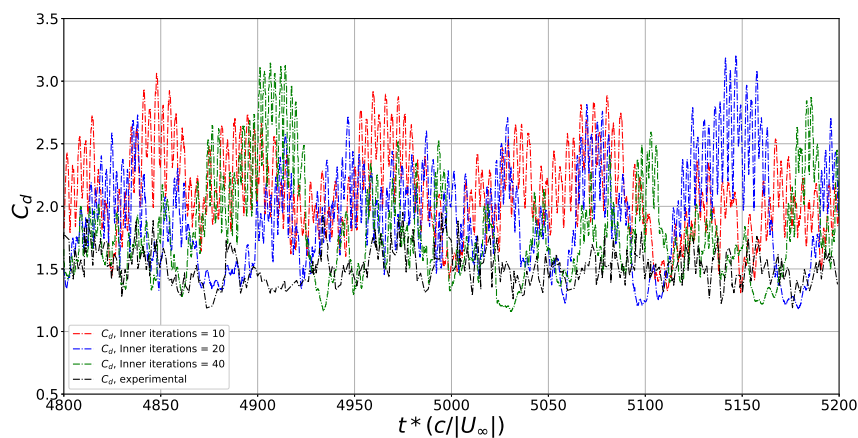
Figure 4.18: Variation of C_d for 10, 20 and 40 inner iterations

From Figures 4.17 and 4.18, it can be observed that in comparison to the trends observed in Figure 4.9, the mean values of the lift and drag coefficients are found to have an improved accuracy by about 10.67% and 11.16% respectively for 20 inner iterations. This can be attributed to an improved convergence, as the number of steady state simulations for a given time step are doubled.

In particular, for Figures 4.17 and 4.18, it can be observed that there is a large variation towards higher non-dimensional times. This can be accounted for by the fact that the solution that is obtained at those time instances, the error that is obtained through those time steps is propagated. Furthermore, as the flow regime is unsteady in nature, it is expected that the error in C_l and C_d would vary with the time instances.

Lastly, it can also be observed that there is a certain periodicity of these errors that can be observed between the time steps 4800 and 4900. On calculation of this periodicity, one can confirm that the peaks in both C_l and C_d are quasi-periodic in nature (as the periodicity varies

with the interval that one considers) of about 5 convective time units. This can be similarly observed in the experimental data as well, which confirms the nature of the flow solution.

Variation of PSD of C_l and C_d
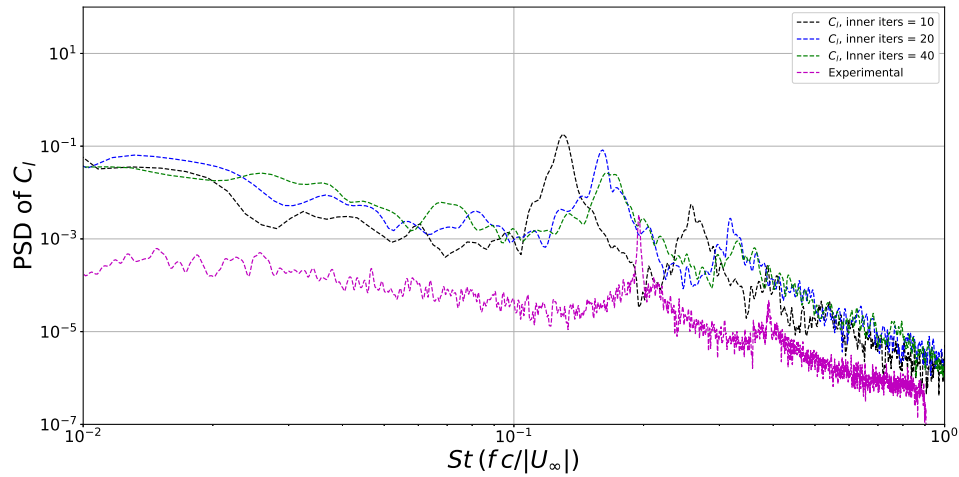
Figure 4.19: Comparison of PSD of C_l for 10 (black), 20 (blue) and 40 (green) inner iterations
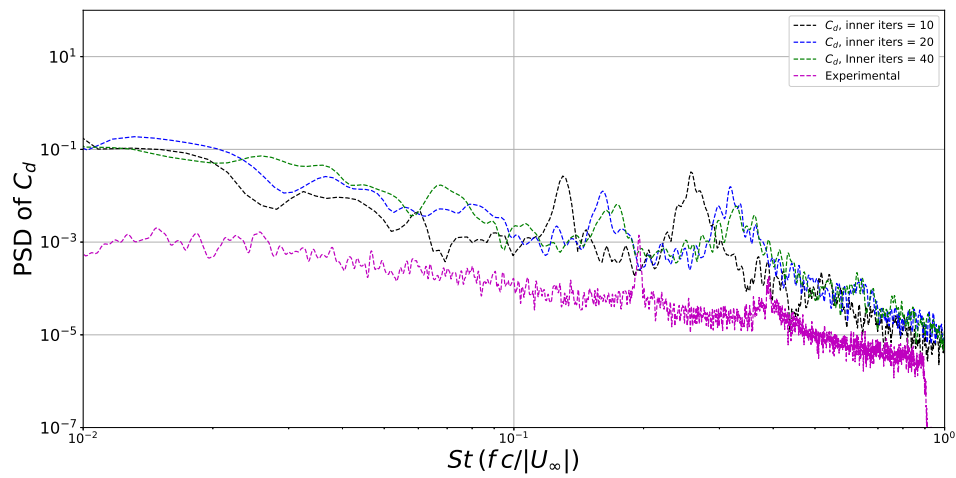
Figure 4.20: Comparison of PSD of C_d for 10 (black), 20 (blue) and 40 (green) inner iterations
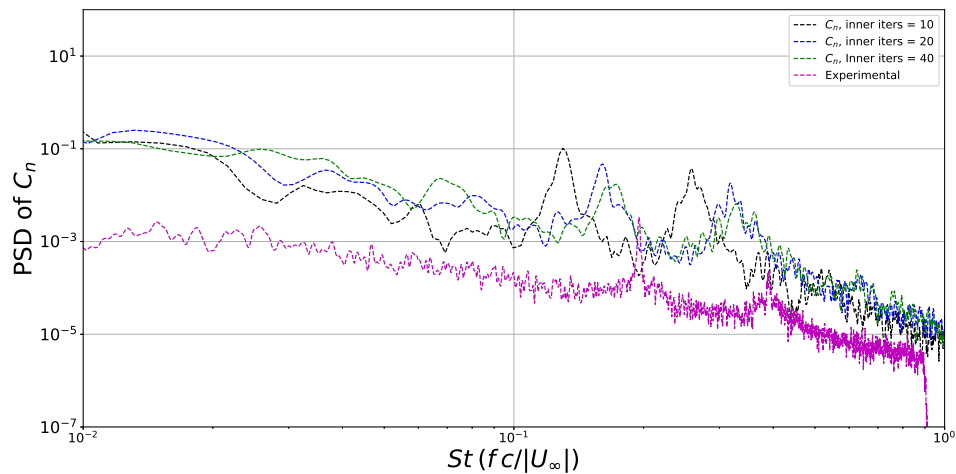
Figure 4.21: Comparison of PSD of C_n for 10 (black), 20 (blue) and 40 (green) inner iterations
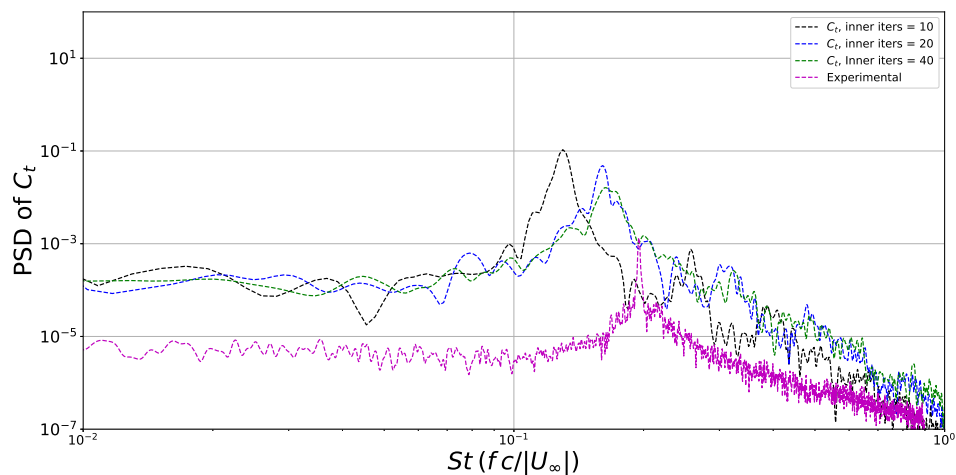
Figure 4.22: Comparison of PSD of C_t for 10 (black), 20 (blue) and 40 (green) inner iterations

From Figures 4.19, 4.20, 4.21 and 4.22, it can be observed that there is a noticeable shift in the peak for the lift coefficient spectrum on increasing the number of inner iterations. This can be attributed to the fact that the C_l values are calculated taking the entire airfoil surface, rather than at a particular section. This results in a higher magnitude of the PSD. Furthermore, there is also a slight translation of the peak that corresponds to the Strouhal frequency. For example, the Strouhal peak predicted by the PSD plot having 40 inner iterations This has been speculated as being caused due to the difference in the definition of the characteristic length to define the Strouhal number. This is not supposed to be the case for comparison with experimental data, wherein the comparison is performed for these coefficients. Therefore, there is a correction that needs to be done to the post-processed values of these coefficients, which has been later explained in sub-section 4.5.2. Another reason that can be cited for this is due to the fact that as the number of inner iterations is increased, the accuracy of the solution is naturally improved. At lower frequencies, there is an over-prediction of the magnitude of all the PSD plots in comparison to the experiment. This has also been observed in the literature by Zhang [16], and was cited as being caused due to the narrow span used for the analysis, which would be unable to capture the 3D turbulent structures accurately and hence, the aerodynamic parameters would not be

correctly obtained.

Another important observation that can be made on adding the filters to remove the noise is that for variation of C_t, there is only a single, major peak that can be observed. This can be reasoned out because of the fact that unlike C_n, which is computed in a direction normal to the airfoil, the tangential direction does not observe a vortex roll-up. This can also be confirmed with the comparison with experimental data, as has been done in Appendix A.

4.3. Comparison of results with various hybrid SGS models

In order to provide a comparative study between the impact of the turbulence models on the accuracy of the solution in comparison to experimental data as well as simulation results obtained from DES solvers, a study of the C_l calculated by using different hybrid SGS models has been described in this section. It is to be noted that in this case, the time history of C_l and C_d could not be obtained using Molina's case, and therefore, the comparisons for the time histories in this analysis are purely obtained by recreating the time history plots using the simulation data obtained from SU2 for various hybrid SGS models. These were then compared with the C_l time history obtained from the experiment, as shown in Figure 4.23.
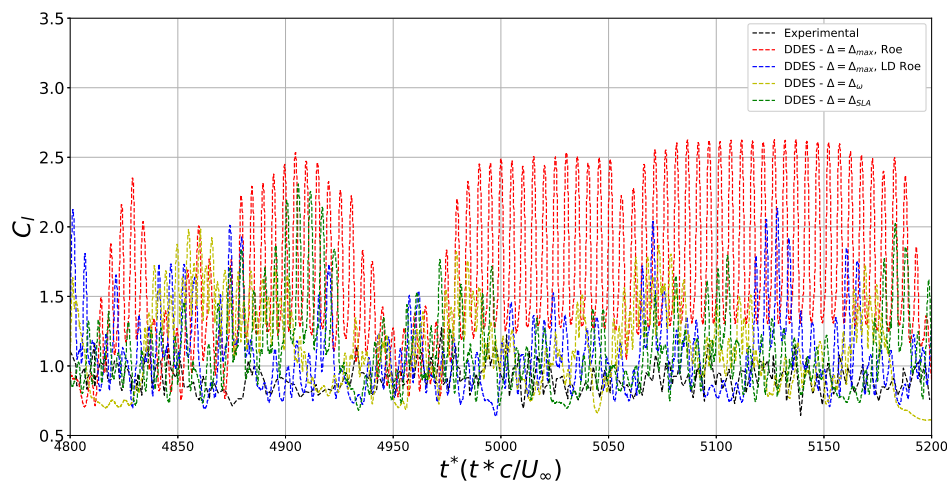
Figure 4.23: C_l time history using different SGS models

From Figure 4.23, it can be ascertained that the time histories of C_l obtained by Molina provide an estimate of how the various hybrid SGS models perform in comparison to the experimental data. One major take-away that can be obtained from this is the fact that the Roe's scheme tends to highly over-predict the magnitude of the time history plots in comparison to the experimental data. This is mainly because of the fact that the scheme tends to be quite numerically dissipative for lower Mach numbers, because of which there is an over-prediction of C_l. The low-dissipation Roe's scheme, on the other hand, provides a better estimate in terms of over-predicting the C_l compared to the experimental time series. This is because of the fact that the low dissipative effects is found to impact the prediction of C_l directly.

4.3.1. Comparison of SGS models obtained from Molina's results
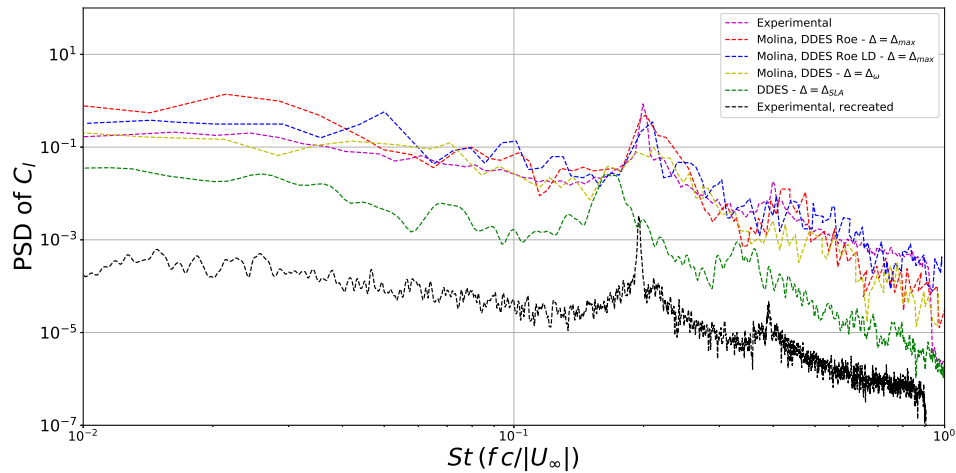
Figure 4.24: Comparison of PSD of C_l for different hybrid SGS models with Molina's results [12]

From Figure 4.24, it can be observed that the trend of similar vortex shedding and the corresponding shedding harmonic peak can be observed. However, from Molina et. al, it was understood that the vorticity-based DDES approach was the most closest to the experimental data. The prediction of the harmonics of the shedding frequency was not done by any of the hybrid SGS models, except the SLA-SGS model.

Another observation that can be made with regards to the magnitude of the trends is that the order of magnitude of the SGS solution. Given that the SU2 solution has slightly lesser magnitude as compared to both the experimental and Molina's results, one can conclude that the frequencies that are below the vortex shedding frequency are not properly taken into consideration. This was also observed in the findings from Zhang [16], in which the lower frequencies could not be captured because of the narrow width in the spanwise direction.

In general, there is a noticeable difference found for the results obtained for the PSD of C_l for different hybrid SGS models, as compared to their corresponding over-predicted time histories. Therefore, there is a need to correctly obtain the PSD from the time series re-created for the various SGS models and compare them.

4.3.2. Comparison of SGS models obtained from Molina's validated results

From the previous sub-section, there is indeed a discrepancy that can be seen in terms of the results obtained from the PSD plots compared to the predictions from the C_l time history plots as described by Figure 4.23, it is necessary to plot the PSD plots that are obtained from the recreated time series for each hybrid SGS model. This is shown by Figure 4.25.
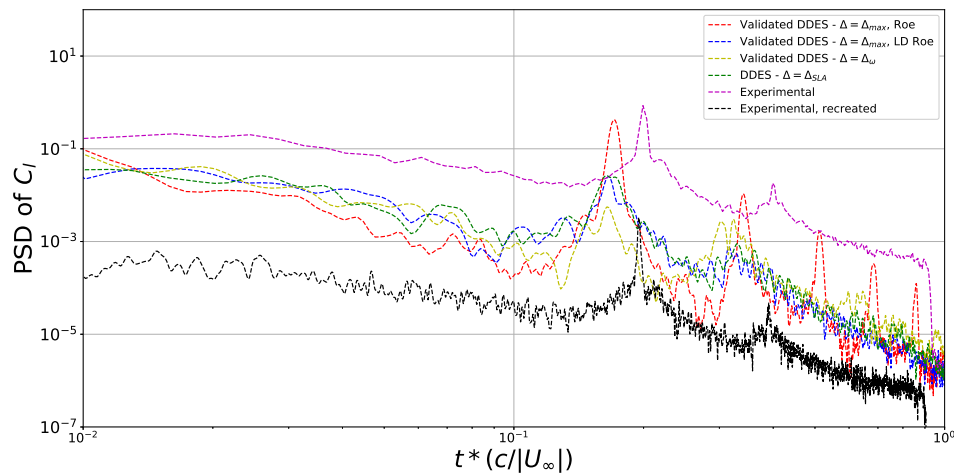
Figure 4.25: Comparison of PSD of C_l vs. St for different hybrid SGS models

Figure 4.25 essentially summarizes the discrepancies obtained when comparing the plot in Figure 4.24. It is quite clear that there is indeed, the presence of the first harmonic, as well as other peaks of the vortex shedding frequency that is predicted by the Roe's scheme, which is not predicted by the same trend obtained by Molina. This was also observed earlier by Zhang [16] for a lower simulation time. The additional peaks after the first harmonic would most likely be caused due to the overly dissipative nature of the Roe's scheme. If they were additional harmonics of the vortex shedding frequency, they would have had to be present in the experimental PSD plot as well, but that is indeed, not the case here. The other SGS models coupled with DDES, however, do not seem to be having these additional peaks. There is also the shift in the vortex shedding peaks that can be observed, at least for the peaks obtained for the main vortex shedding and its first harmonic, in comparison to the experimental PSD. This can be again accounted for due to the fact that the wake length is taken into account in the definition of Strouhal number in this analysis ($c \times \sin 60°$), which is not taken into account in the analysis done in the experiment. This is also elaborated in Appendix A.

Another important observation is that all the PSD plots under-predict the experimental time series obtained. Although this is contradictory to the result obtained from not only Molina, but also due to the fact that the C_l time series is over-predicted by the SU2 solution in comparison to the experimental data. However, this discrepancy is caused because of the fact that the PSD computed from the experimental time series using the algorithm given in Appendix A and Welch's approach are different compared to that obtained from the experiment. In reality, all the hybrid SGS models over-predict the PSD plot of the experimental data.

4.4. Comparison of results obtained from sectional 2D analysis

Since the results obtained so far are the three-dimensional (3D) aerodynamic parameters calculated as the time series as well as the PSD plots respectively, it is necessary to compare the results obtained for C_l and the other coefficients obtained from SU2 for a particular spanwise location on the airfoil. This is because of the fact that the analyses performed in the experiment were obtained for a section of the airfoil. Therefore, there is a need to obtain the corresponding sectional coefficients as well for comparison and validating with experimental data.

This was performed by taking into account the formulation of lift coefficient as given by Anderson [62]. According to this, the forces acting on the airfoil were described based on an airfoil having a unit span according to the geometry shown in Figure 4.26.
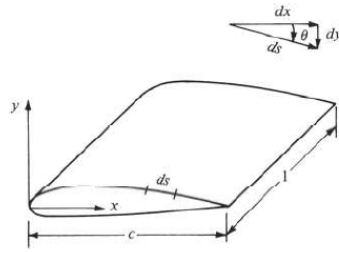
Figure 4.26: Figure showing different lengths of airfoil geometry, as described in Anderson [62]

From Figure 4.26, it can be observed that the following relations given by Equation 4.2 hold true:

$$dx = ds \, cos\theta$$
$$dy = -(ds \, sin\theta)$$
$$S = c(1) \tag{4.2}$$

Using the geometry shown in Figure 4.2, the forces acting on the airfoil are calculated. This is done by first finding the normal and axial (or tangential) force coefficients (given by c_n and c_a respectively) as shown by Equations 4.3 and 4.4 respectively.

$$c_n = \frac{1}{c} \left[\int_0^c (C_{p.l} - C_{p,u}) \, dx + \int_0^c \left(c_{f,u} \frac{\mathrm{d}y_u}{\mathrm{d}x} + c_{f,l} \frac{\mathrm{d}y_l}{\mathrm{d}x} \right) \, dx \right] \tag{4.3}$$

$$c_a = \frac{1}{c} \left[\int_0^c \left(C_{p,u} \frac{\mathrm{d}y_u}{\mathrm{d}x} - C_{p,l} \frac{\mathrm{d}y_l}{\mathrm{d}x} \right) \, dx + \int_0^c (c_{f,u} + c_{f,l}) \, dx \right] \tag{4.4}$$

In this case, the subscripts 'u' and 'l' denote the upper and lower sides of the airfoil respectively. Finally, if α is the angle of attack of the airfoil, then the lift and drag coefficients can be simply obtained by using a forces split-up as shown in Equations 4.5 and 4.6 respectively.

$$C_l = c_n cos\alpha - c_a sin\alpha \tag{4.5}$$
$$C_d = c_n sin\alpha + c_a cos\alpha \tag{4.6}$$

The results were obtained by using the Python module of Paraview called PvPython, and were compared with experimental data and the 3D results to provide a comparison between the two. The spanwise location for which the results were obtained was the section at 0.363b, where b is the span, which also corresponds to the location where the pressure measurements were taken into account in the experiment as well [6].

4.4.1. Time series of C_l
The time series of C_l is shown in Figure 4.27.
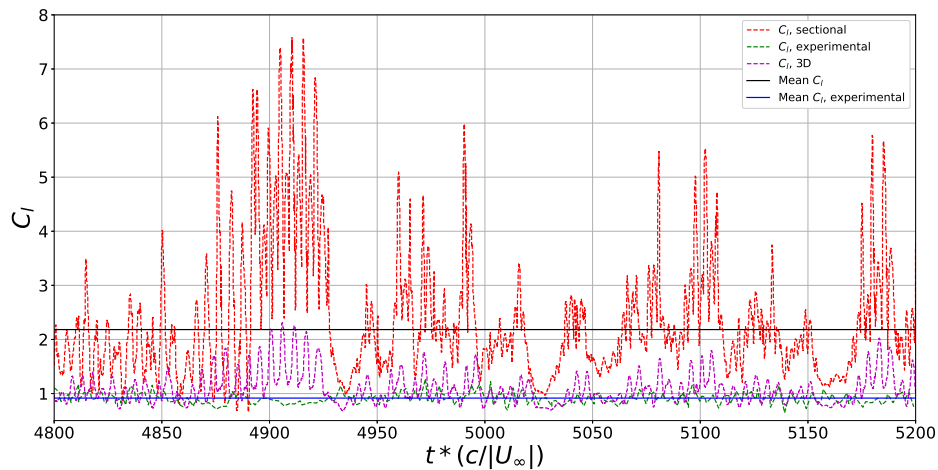
Figure 4.27: Variation of C_l with t^* at $x/b = 0.363$

From Figure 4.27, it can be observed that there is an especially large over-prediction of the c_l at the intervals of non-dimensional time steps 4850-4950 t^*. This was also observed in the intervals after 4950 CTUs. Therefore, the results obtained from this method are not found to be extremely reliable. There is, however, one trend that goes in accordance with that obtained from the 3D results, and that is the fluctuations that are present for each non-dimensional time step, although over-predicted by the 2D sectional values, are still in agreement with the trends obtained from the 3D PSD calculation. This can also be compared by taking a close-up view of the predicted values, as shown by Figure 4.28.
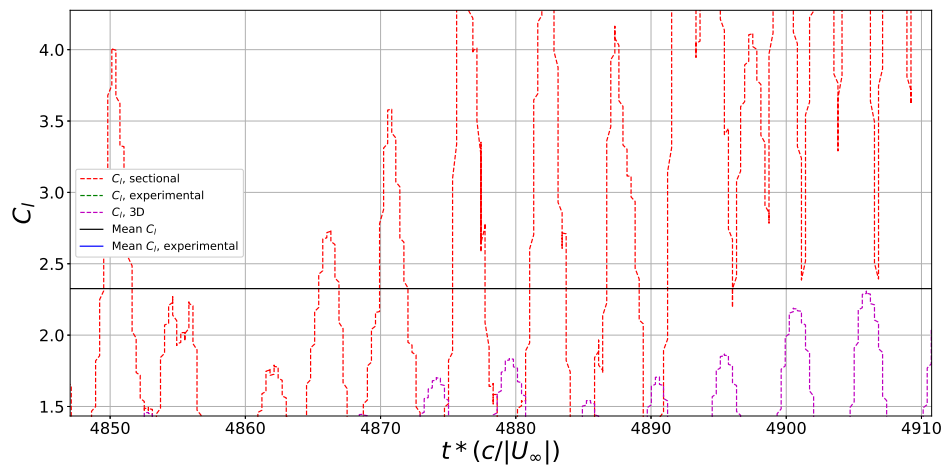
Figure 4.28: Close-up view of sectional C_l

As one can observe from Figure 4.28, it can be clearly seen that the fluctuation in C_l between any two CTUs obtained from the sectional lift and the 3D lift remain the same, as the gaps between any two peaks in the range of 4850 to 4950 t^* remains more or less the same. The peaks obtained from the sectional 2D results also mimic their locations as compared to the 3D results. However, there is still a massive over-prediction by the sectional 2D results. This can be confirmed by the mean values of the two coefficients. While the mean value of C_l predicted by the sectional value is 2.1825, while the mean value obtained from the 3D value is found to be 1.071. Therefore, one cannot be sure that the values obtained from the sectional 2D lift are physical. However, the C_l values predicted from this analysis are over-predicted as the number

of iterations progress, which is also consistent with the trends obtained from the 3D results. This is also consistent with the fact that for a span of $1c$, the 2D and 3D results are not very different [10].

4.4.2. PSD of C_l
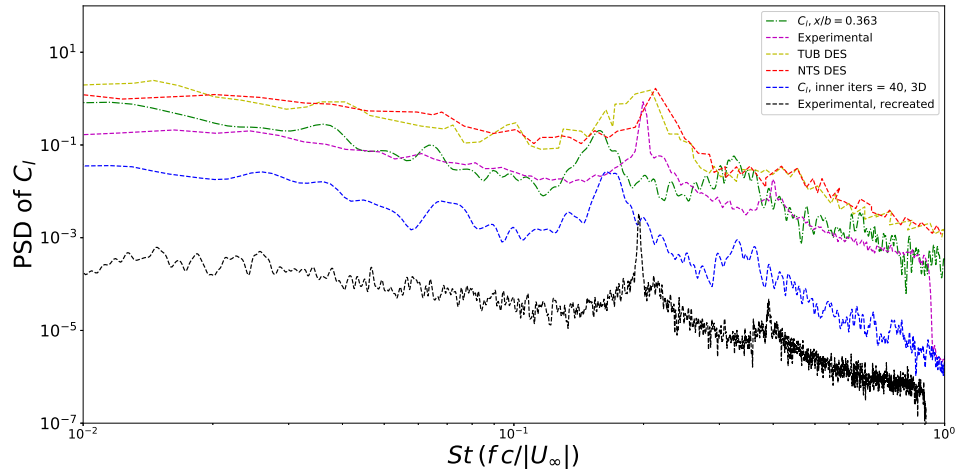
Figure 4.29: Comparison of PSD of C_l for the 3D case, 2D sectional data, experimental data [6] and computational data [14]

From Figure 4.29, the variation of the lift coefficient provides an insight into one very important phenomenon occurring: the 2D sectional results consistently over-predict the PSD values in comparison to the experimental data. This is consistent with the C_l time history as well and therefore, is physical as well. The 3D C_l values seem to have an over-prediction, but only for frequencies below the vortex-shedding peak. Given that a spanwise averaged peak could have been the only comparison with experimental data, the 3D coefficient could only have been compared in that manner. There is also a clearer shedding peak corresponding to the harmonic of vortex shedding for the sectional 2D C_l compared to the 3D case. This is also an indication that using the sectional 2D plot was actually beneficial to provide a correct estimate of the physical phenomenon happening when compared to the experimental results. Lastly, there is also a slight-under-prediction of the vortex shedding, as well as the harmonic of the vortex shedding peak - the St peak for vortex shedding from the 2D results is 0.162, while that from the experimental results is 0.2. In a similar manner, the harmonic of the vortex shedding peak predicted from the sectional 2D result comes out to be 0.35, while the one predicted from experimental data is about 0.4. This discrepancy can be caused due to the fact that there is an estimation of C_l that does not take into account the effect of wind tunnel effects as in the experiment, such as blockage effects, slipstream effects etc.

Furthermore, it is also important to notice that the difference in the 3D and 2D lift curves is not a lot, because of the fact that a periodic boundary condition is imposed on the ends of the walls. This would mean that there would be similar trends expected for all the surfaces on the airfoil, which would also be reflected in the aerodynamic performance coefficient plots. A better comparison can also be made by taking into account the spanwise averaged trends of the PSD plot.

4.4.3. Time series of C_d
The time series of C_d is shown in Figure 4.30.
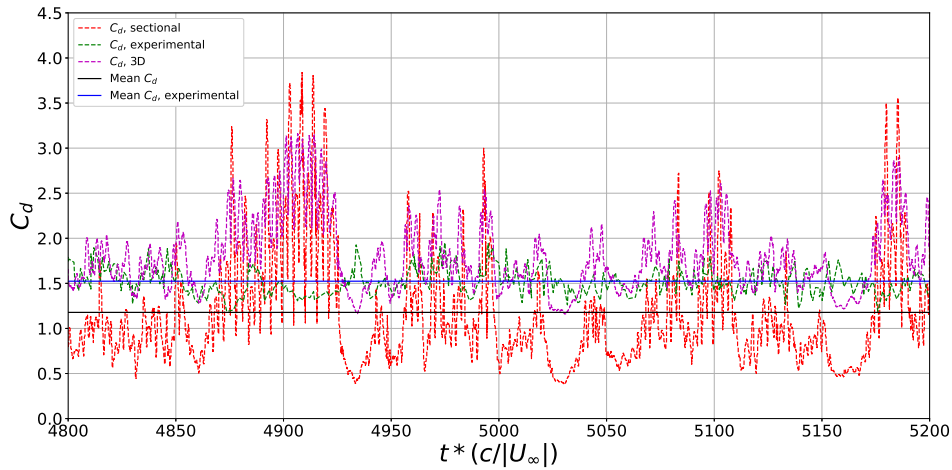
Figure 4.30: Variation of C_d with t^* at $x/b = 0.363$

From Figure 4.30, it can be observed that there is once again an over-prediction of C_d in comparison to the 3D data, but only corresponding to those time steps where there is an over-prediction of the density residuals. There is also an under-prediction of 13.33% in the C_d values predicted from the sectional 2D method. This could again be attributed to the fact that there is an under-prediction because of the absence of additional wind tunnel factors that could have contributed to a larger drag coefficient. This includes the effect of not including the effects of roughness on the airfoil, the absence of slipstream effects and so on, which were also described as the cause of the under-prediction of the sectional 2D C_l as well.

4.4.4. PSD of C_d
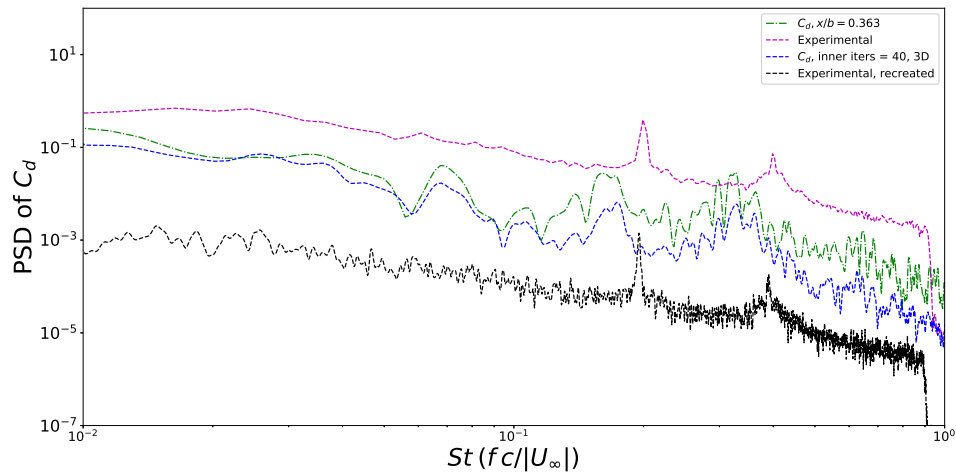
Figure 4.31: Comparison of PSD of C_d for the 3D case, 2D sectional data, experimental data [6] and computational data [14]

From Figure 4.31, it can be observed that there is an over-prediction of the PSD of C_d obtained from the 2D results compared to the 3D values. This could be because of the fact that formulation of PSD used in the calculation, as shown in Appendix A, misses a term dt, because of which the actual PSD prediction from the 2D case should be effectively lesser than the experiment, which would then match the trend predicted by the time series data of C_d. Furthermore, akin to what

was observed for the C_l plots, the PSD also has the absence of certain low-frequency content, as can be observed by the presence of the step. This is attributed to the presence of the filter that removes lower frequencies below a certain threshold.

4.5. Validation studies performed

Now that the results obtained from the simulations have been compared with an empirical model for sectional 2D calculations, the next step would be to validate the results obtained in the thesis with various other existing literature, so as to question the scientific validity of the results in different contexts.

The validation studies performed in this thesis are divided into multiple categories, which can be broadly described as either based on experimental or computational results. Given that the literature does not have a lot of experimental evidence for the current flow problem, as has been observed in Chapter 2, a lot of the following comparisons have been made using either different RANS turbulence models (such as S-A or variants of it), or with different kinds of meshes.

4.5.1. Validation of results with experimental data
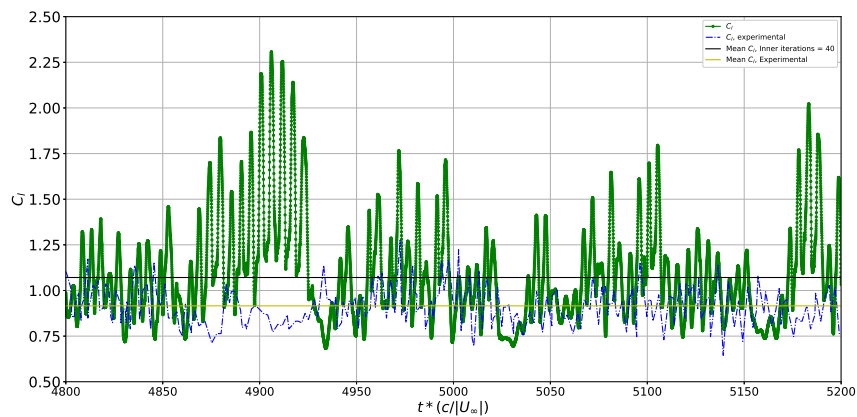
Figure 4.32: Comparison between C_l plots with DDES solution and Swalwell [6]

As can be seen from Figure 4.32, the C_l prediction still higher than experimental data. But the mean value is about 16.94%, which has a major offset because of the presence of an overshoot in the time steps between 4850 and 4950, as well as in various other intervals. This is primarily due to the fact that the narrow span of the current geometry plays a major role in the over-prediction of the lift coefficient. This was also noticed by Garbaruk [10]. This over-prediction can be primarily observed for the time steps between 4950 and 5000 non-dimensional time steps, as well as in the other t^* intervals.

From the literature involving multi-grid problems, one can also observe that there are two ways of looking at the fluctuations in the lift coefficient. One of the primary observations regarding this is the fact there is the presence of chaotic fluctuations in the C_l history. The second period that could be observed is the periodicity of vortex shedding, that provides an indication of the major flow physics in the problem, that of the presence of periodic vortex streets that were observed in Chapter 2.

Furthermore, as can be observed from the experimental data, there is a multi-modal phenomenon that can be observed, corresponding to both weak and strong vortex shedding modes. This was also observed in the DESider project, when there was a quasi-periodic vortex shedding observed for every 5 convective time units (non-dimensionalized by c/U_∞) [14]. This alternation between the weak and the strong vortex shedding modes is quite random in nature, and could also account for the fact that the solution would have to be run for an even more longer period of time.
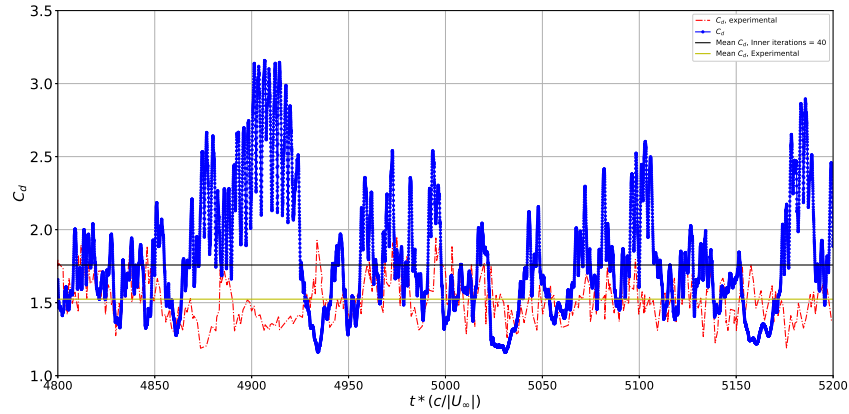
Figure 4.33: Comparison between C_d plots with DDES solution and Swalwell [6]

In order to delve into how the performance characteristics of the airfoil would be affected by the number of inner iterations, this section compares the coefficients with experimental data from Thiele et al. [63].

4.5.2. Validation of results with DES and experimental data

The comparison of the lift coefficient is performed by using both experimental data obtained from Swalwell et. al [6], as well as computational results obtained from the DESider project [14], in particular, the ones obtained from TU Berlin and NTS University, St. Petersburg. Another comparison is done by adding the Hanning weighting to the results, so that the impact of the same is observed. This is the default comparison that is performed for the rest of the force coefficients, such as the C_d, C_t and C_n ones.
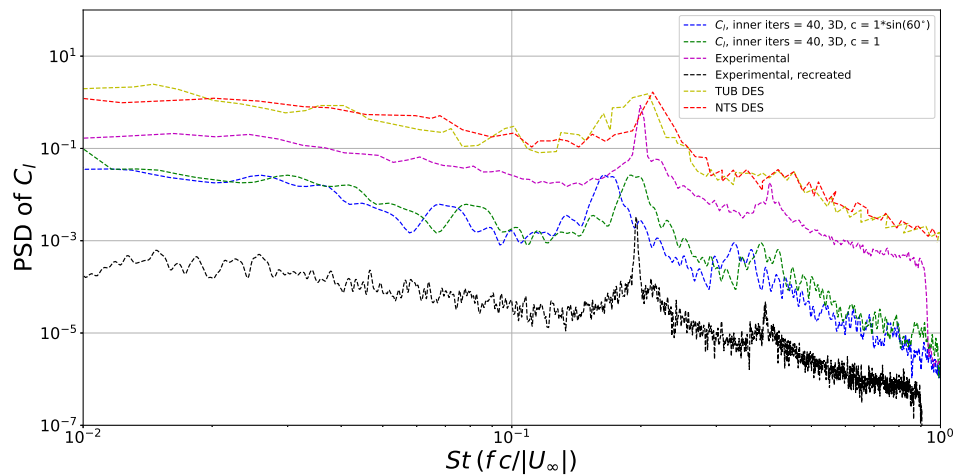
Figure 4.34: Variation of C_l vs. St using (a) SU2 (depicted by blue and green) (b) DES data from the DESider project (depicted by red and yellow) [14] (c) Experimental data from Swalwell (depicted by magenta) (d) Re-created experimental PSD of C_l by using data provided by the DESider project [14] (depicted by black) [6]

From Figure 4.34, it can be observed here that there are two peaks that can be observed: one corresponding to the vortex shedding frequency, and the other corresponding to the harmonic of the vortex shedding frequency itself. While the former can be estimated by using experimental evidence, the latter requires the use of empirical/semi-empirical data for validation. Furthermore, the peak for vortex shedding corresponding obtained from SU2 (~ 0.199) is similar to the one

as the one mentioned by experimental data (~ 0.2). Thus, there is a good agreement with identifying the vortex shedding frequency. Additionally, there is also a presence of a second peak corresponding to the experimental data, which also occurs at nearly the same Strouhal number (~ 0.41). Lastly, there is a good order of magnitude agreement between the SU2 and experimental results (the order of magnitude both PSDs is of order 10^{-1}), which also justifies the use and the advantage of the DDES approach over the DES approach.

From Figure 4.34, it can be observed that corresponding to the second peak of the harmonic of vortex shedding there is a Strouhal number of 0.4. In comparison to the literature, this proves to be a pretty accurate description, when compared with the second peak with Swalwell et. al., there is a considerably good comparison, as the experimental value comes out to be predicted lower than the simulation value. This can be accounted for due to either the use of the coarse mesh in the present case, or because of the narrow span used, that causes an over-prediction of the results. This has also been confirmed from previous studies by Garbaruk et al. [10].
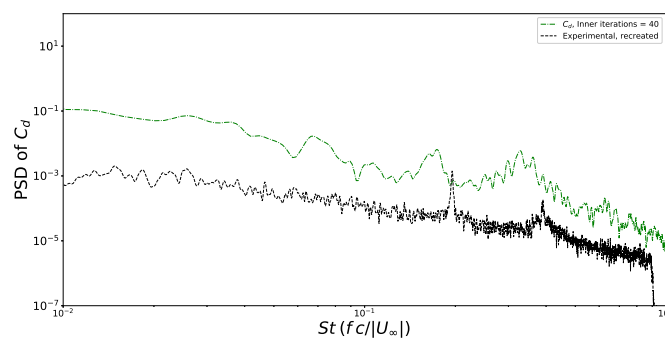
Figure 4.35: Variation of C_d vs. St using (a) SU2 (depicted by black) and (b) Experimental data [6]

Similar to what has been observed for the C_l time history in Figure 4.34, the drag results in Figure 4.35 have a similar trend, with the peaks corresponding to vortex shedding having a higher magnitude in comparison to the experimental data. Furthermore, there is also the presence of an additional peak corresponding to a Strouhal number of 0.4245, which has an error of approximately 5.31% compared to that predicted by the experiment. The harmonic of the vortex shedding frequency is over-predicted by about 6.93% in comparison to the experimental data.
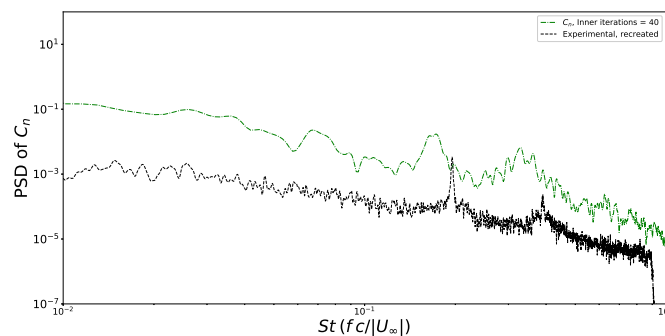
Figure 4.36: Variation of C_n vs. St using (a) SU2 (depicted by black) and (b) Experimental data [6]

From Figure 4.36, it can be observed that the shedding frequency for the vortices is visible, but is not so clear for the peak that corresponds to the harmonic of vortex shedding. Furthermore, there is a good order of magnitude comparison obtained for higher frequencies, especially beyond the characteristic vortex shedding frequency. For the main vortex shedding peak, the

over-prediction by the simulation data is by 2.43%, while for the peak corresponding to the first harmonic of the vortex shedding frequency, the simulation data over-predicts the peak by 7.2%.
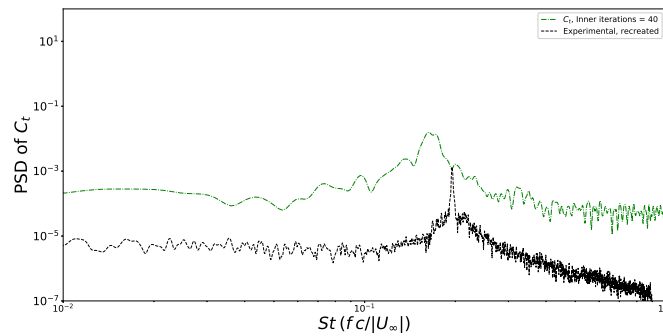
Figure 4.37: Variation of C_t vs. St using (a) SU2 (depicted by black) and (b) Experimental data [6]

From Figure 4.37, it can be seen that the shedding frequency for the vortices is visible, but is absent for the harmonic of vortex shedding. The main peak corresponding to vortex shedding is slightly over-predicted by the simulation result by 1.82%, which is well within the scientific limits of accuracy. However, there is a good order of magnitude comparison obtained for higher frequencies, especially beyond the characteristic vortex shedding frequency, given by the Strouhal number of 0.2 [6]. Another important observation that can be made in this comparison is the fact that the first harmonic corresponding to vortex shedding was found to be absent. This could be because of the fact that the tangential force coefficient does not take into account the vortex roll-up in the spanwise direction, which could contribute to the absence of this harmonic being detected.

4.5.3. Validation of existing hybrid SGS models by Molina

In order to obtain a comparison between the 3D results obtained in this thesis and other studies available in the literature in terms of the hybrid SGS models, turbulence models and different kinds of meshes, different validation studies are performed. In order to confirm the results obtained in the literature using different hybrid SGS models, an attempt to replicate the results obtained by Molina et al. [12] is done. These models are, namely, the DDES approach by taking the maximum grid size and using the Roe's scheme (denoted by $\Delta = \Delta_{max}$, Roe), the DDES approach by taking the maximum grid size and using the low-dissipation Roe's scheme (denoted by $\Delta = \Delta_{max}$, LD Roe) and the vorticity-based DDES approach using the LD Roe's scheme (denoted by $\Delta = \Delta_\omega$), respectively.

The comparison of these various models is first done by comparing the time series history of C_l for each hybrid SGS model, and then the PSD spectra are compared. All the models are also compared with the SLA-SGS, keeping in mind the fact that the there is a shift in the peak, that corresponds to the likely wake width ($c \times \sin 60°$). This is also to compare the results with the experimental data, which has also made a similar calculation for the Strouhal number calculation. It is to be noted that the time history of C_l from the data provided by Molina could not be obtained, and hence, was not compared in the time series. Hence, the time series for this sub-section was obtained by re-creating the various hybrid SGS models. The results obtained from these models are described in the subsequent sub-sections.

DDES using $\Delta = \Delta_{max}$ and Roe's scheme
The comparison of the time series history of C_l for $\Delta = \Delta_{max}$ compared to the results obtained from the experiment, as well as the SLA-SGS scheme is described in Figure 4.38.
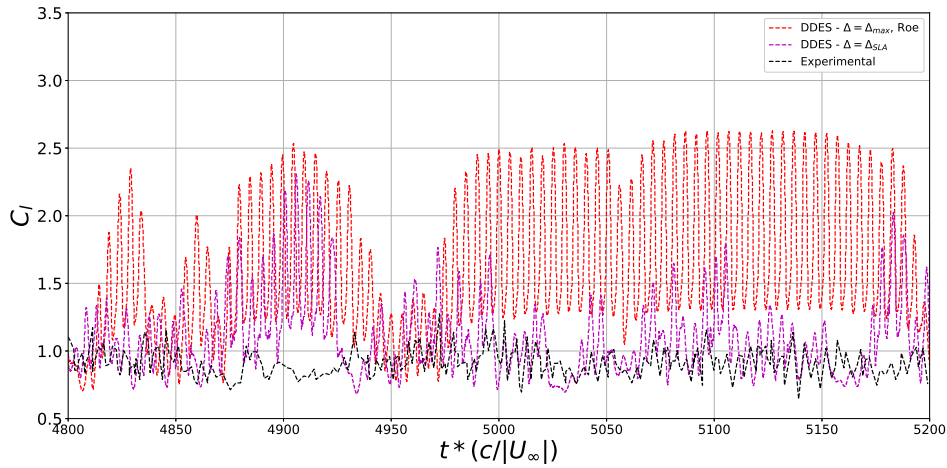
Figure 4.38: Comparison of time histories of C_l obtained from the Roe's scheme, compared with the SLA-SGS scheme and experimental data [6]

From Figure 4.38, it can be observed that there is a clear over-prediction of the C_l values in comparison to not only the experiment, but also the SLA-SGS results as well. This can be due to the over-prediction of C_l because of a narrow span, which was first observed in the PSD plots obtained in the DESider project [14], and later by Garbaruk [10]. Another interesting observation that can be made is a seemingly constant variation of C_l after 4975 CTUs. There is a possibility that this is caused because of the fact that the Roe's scheme, being purely upwind in nature, causes numerical errors to be considerably less dispersed in comparison to the results obtained from the more conservative results obtained from the NTS scheme, which was used to obtain results for the SLA-SGS model. The over-prediction by using the Roe's scheme and the regular DDES ($\Delta = \Delta_{max}$) amounts to an error in the mean value of C_l of about 48.31% compared to the simulation data and the experimental time series by approximately 62.79%, which are both extremely high. Therefore, the trends obtained from the time history plots are over-predicted due to the nature of the numerical scheme, and the chaotic fluctuations are characteristic of the complex physics that one encounters in the current flow problem.

The variation of the PSD of C_l for the results obtained from Molina and the validation study, along with the experimental PSD plot, are presented in Figure 4.39.
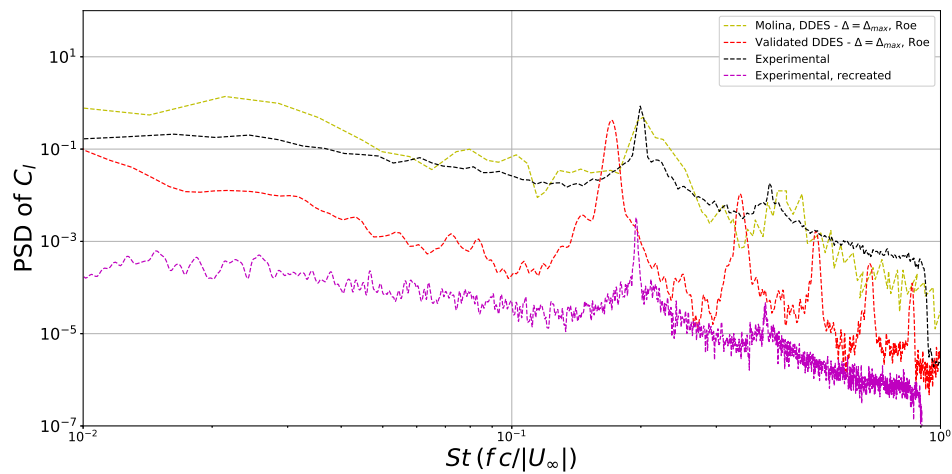
Figure 4.39: Validation of PSD of C_l using Roe's scheme

From Figure 4.39, it can be observed that there is a clear discrepancy in the prediction of the PSD from the Roe's scheme run as compared to the results obtained from Molina. This could be because of the fact that the present simulation setup has used a slightly different formulation of PSD in comparison to the literature (there is a factor of dt that causes the results to differ, which has also been found to match with that used in the literature, as can be seen in the results obtained from sub-section 4.5.2). Furthermore, there is a large number of peaks that can be found in the larger frequencies, which can be attributed to due to the Roe's scheme's upwind nature, or the presence of additional harmonics corresponding to vortex shedding, which is unlikely the case due to the absence of these additional harmonics in the experimental plot. In either case, these are an indication of the presence of excess eddy viscosity in the Roe's scheme at low Mach numbers. Furthermore, there is a shift in the Strouhal number peaks corresponding to vortex shedding and the harmonic corresponding to the peak of vortex shedding , in order to account for the correct comparison with experimental data (the length scale in the validation simulation result is taken to be $c * \sin 60°$ instead of c in order to be consistent on comparing with experimental data). These results are very similar to the ones obtained by Zhang et al. [16] as can be seen in Figure 2.9, wherein the large fluctuations at higher frequencies were obtained even for lower CTUs. Furthermore, the over-prediction of the PSD at lower frequencies was attributed to the fact that the spanwise effects could not be accurately depicted with the current geometry having a span of $1c$. This was insufficient to capture the 3D turbulent fluctuations, as was also the case with the results obtained by Zhang as well.

Furthermore, the discrepancy regarding the over-prediction of the PSD obtained from the Roe's scheme, as compared to the re-created experimental PSD can also be noticed, with the prediction in the vortex shedding peak in this case corresponding to the nature of the numerical scheme itself, rather than the difference in the characteristic length scale used to define the Strouhal number. The difference in the St peaks for the major vortex shedding peak, predicted by Roe's scheme and using the $\Delta = \Delta_{max}$ DDES scheme is about 12.19%.

DDES using $\Delta = \Delta_{max}$ and LD Roe's scheme
The result in this sub-section was obtained by using the Roe's scheme in tandem with the NTS dissipation scheme, as the Roe's scheme was found to diverge when using the FD wall dissipation function that was used by Molina.

The comparison of the time series history of C_l for the low-dissipation Roe's scheme using the $\Delta = \Delta_{max}$ SGS scheme, compared to the results obtained from the experiment, as well as the SLA-SGS scheme is described in Figure 4.40.
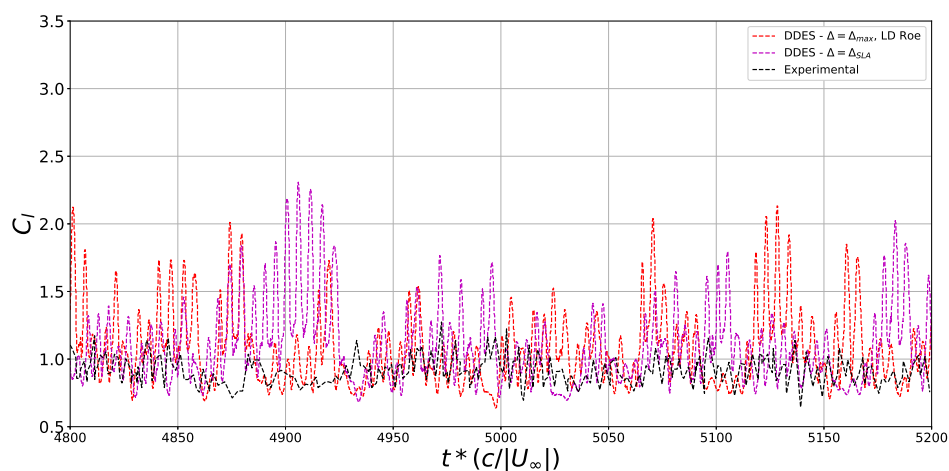
Figure 4.40: Comparison of time histories of C_l obtained from the low dissipation Roe's scheme, compared with the SLA-SGS scheme and experimental data [6]

From Figure 4.40, it can be observed that unlike the regular Roe's scheme, the low-dissipation scheme seems to provide a better order of magnitude comparison with the SLA-SGS and experimental results alike, although the magnitudes are still over-predicted. Furthermore, there is also the presence of a chaotic fluctuations that are characteristic of DDES simulations. The literature ([8], [16]) has mentioned several times that these are caused due to the lack of computational time. However, given the stochastic nature of the flow, the literature has shown that these fluctuations do not die down even after 1000 CTUs [3]. Therefore, it can be concluded that this vindicated the stochastic nature of the flow, as the fluctuations do not go down even after 5000 CTUs. Although this is despite the fact that the solution obtained from this analysis was the found to be obtained by using a converged solution, as was determined from the residuals explained in Chapter 3, the stochastic nature of the flow still ensures that these fluctuations remain. This was also observed in the work performed in the DESider project [14].

The variation of the PSD of C_l with St in comparison with the LD Roe's scheme (using the f_d function), the validated model (using the NTS LD Roe function) and experimental data is given in Figure 4.41.
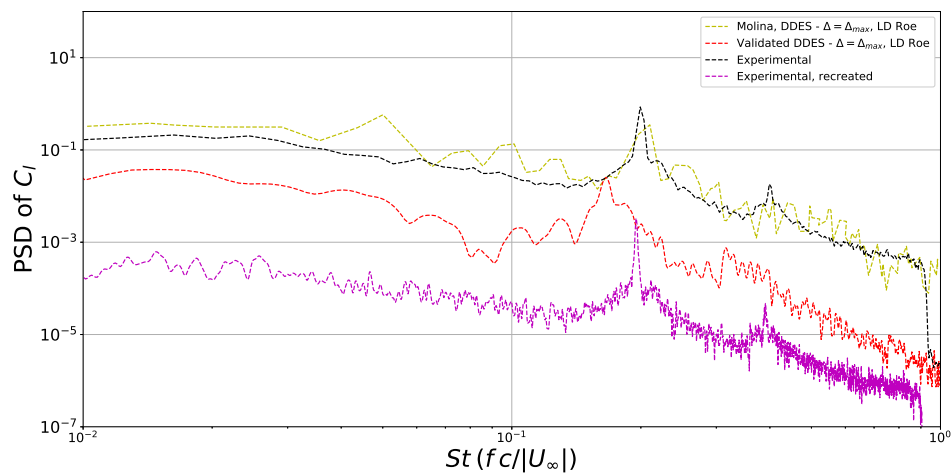
Figure 4.41: Validation of PSD of C_l using the low-dissipation (LD) Roe's scheme

From Figure 4.41, it can once again be observed that there is an overall under-prediction of the magnitude of PSD of C_l. This could be due to the fact that there is a difference in the low dissipation function used with the Roe's scheme (FD vs. NTS). The operation of the FD function is simply based on the empirical function f_d of the DDES formulation [43], which seems to be over-predicting the eddy viscosity because of the use of only a single upwind scheme, in contrast to the NTS function that predicts a larger eddy viscosity in separated flow regions based on a blending function [54]. Furthermore, there is a shift in the PSD plots obtained from the simulation as compared to the PSD plot obtained from the experimental PSD, which can be accounted for the fact that there is a difference in the length scale that is taken into account as explained in the previous sub-section. However, the re-created experimental PSD also has a shift in the peak corresponding to the major vortex shedding. This is due to the nature of the LD Roe scheme itself, which causes a difference of 14.59% compared to the re-created experimental PSD.

DDES using $\Delta = \Delta_\omega$
The results in this sub-section, like the previous sub-section, was obtained by using the Roe's scheme in tandem with the NTS dissipation scheme, as the Roe's scheme was found to diverge when using the FD wall dissipation function that was used by Molina.

The comparison of the time series history of C_l for the vorticity-based SGS scheme ($\Delta = \Delta_\omega$), compared to the results obtained from the experiment, as well as the SLA-SGS scheme is described in Figure 4.42.
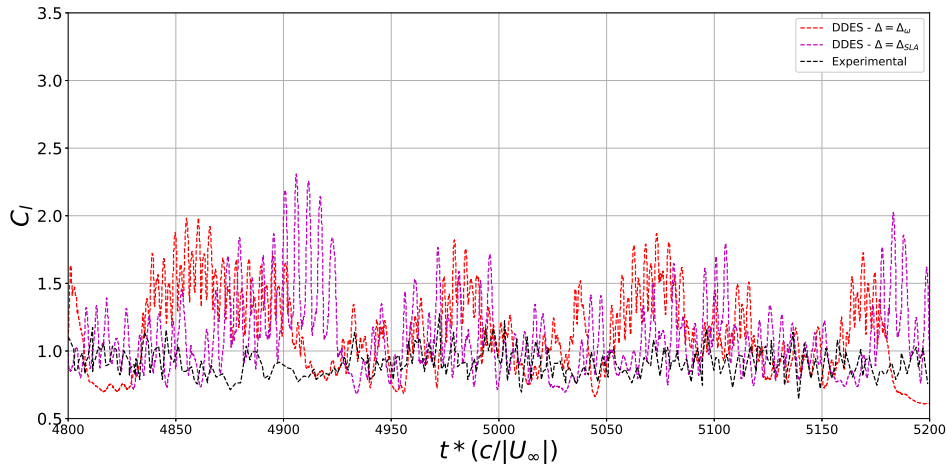
Figure 4.42: Comparison of time histories of C_l obtained from the vorticity-based SGS scheme, compared with the SLA-SGS scheme and experimental data [6]

From Figure 4.42, it can be observed that there is a clear shift in the time history plot of C_l. This could be due to the fact that the definition of the sub-grid length scale is very different in the two cases: while the former takes into account the grid sizes from all directions, the regions of the smallest grid size can be troublesome, which can cause an incorrect computation of the grid size and the corresponding resolution of the vortices. Therefore, there is a phase shift in the prediction of C_l by the vorticity-based SGS model. The over-prediction compared to the experimental data is still present, and the mean value of C_l is comparatively higher than the experimental value (18.44% compared to 16.94% from the SLA-SGS method).

The variation in the PSD of C_l with St for the vorticity based DDES, the validated model (using Roe's scheme and the $\Delta = \Delta_\omega$ SGS model with DDES), and the experimental data is given in Figure 4.43.
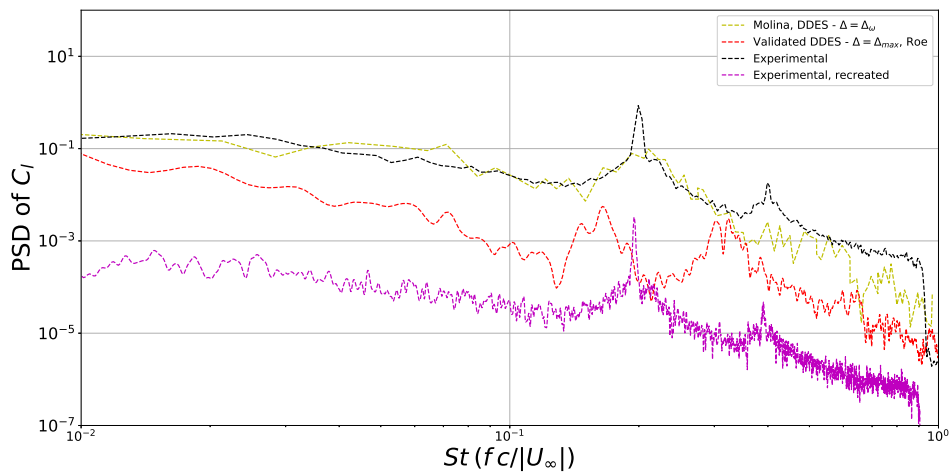
Figure 4.43: Validation of PSD of C_l using the vorticity-based DDES with Roe's scheme and the FD low dissipation function

From Figure 4.43, there is once again a discrepancy in terms of the order of magnitude. Once again, the numerical scheme in tandem with the method used to obtain the flow solution come into the picture - the vorticity-based approach, correcting the length scale to be used

based on the formulation provided by Deck [42]. This could contribute to the activation of LES in regions where the wall function would otherwise operate in the RANS mode. This could cause an increased eddy viscosity prediction, thus reducing the C_l prediction.

A general remark regarding the three validation studies that can be made is that the simulation results seem to under-predict the PSD magnitude at almost all frequencies. This could be due to the fact that the results obtained from the simulation are 3D values of C_l, that cause the amplitude of the frequencies to be under-predicted. Therefore, in such a case, the vortex-shedding peak is only taken to be the point of reference when comparing with experimental data. Furthermore, the over-prediction at lower frequencies is because of the fact that a narrow span was used. When comparing all the three models with the re-created experimental PSD trends, however, it was observed that there was clearly an over-prediction by all the models. This is also consistent with their corresponding time histories.

4.5.4. Validation of SLA-SGS model results with SAS model

This section covers the validation of the results obtained from the sub-grid adapted scale (SLA) based hybrid SGS model in comparison to the scale-adaptive simulation (SAS) approach. On the outset, it might seem to the reader that the comparison is for results obtained from different turbulence models. However, it must be kept in mind that this is also in accordance with the fact that the there is a need to explore how various turbulence models impact the aerodynamic results obtained.

Validation of results from Patel et al. [18]

In order to provide a reasoning of the SLA-SGS model results as a justification of its use in subsequent comparisons, a validation study is performed with the study conducted by Patel et al. [18]. To provide a comparison of the impact of the turbulence model on the C_l and C_d, this comparison is made for the purpose of obtaining the impact of a turbulence model that can be alternately used in place of the current SA model.

In this study, a NACA 0012 airfoil was used to verify the capabilities of a DES solver that used a variant of the Spalart-Allmaras (SA) turbulence model by introducing a new term in the strain rate tensor that incorporates the use of a first order velocity gradient, called the scale adaptive simulation (SAS) model. This approach, first described by Egorov and Menter for hybrid RANS/LES applications [64], was done by taking into account the fact that the turbulence length scale is locally adjusted to account for flow inhomogeneities. This is done by using the von Karman length scale and generalizing the same for any given three-dimensional flow. The model resulting from this analysis uses URANS for stationary and boundary layer attached flows, and reduces eddy viscosity based on the local vortex size for massively separated flows.

The reason for comparing the results obtained from the NACA 0012 airfoil is because of the fact that at such high angles of attack, the influence of airfoil thickness would be expected to be minimal [3]. Therefore, this comparison between two airfoils of different thicknesses at this angle of attack is indeed, justified.

The mesh used was also an O-grid one, with the Reynolds number for the flow to be 13 $\times$ 10^5, and the Mach number to be 0.5. A 4th weighted essentially non-oscillatory (WENO) scheme was used for spatial discretization, while a dual time-stepping approach was used for temporal discretization, with a first order implicit Euler scheme used for the pseudo-time stepping routine.

The variation of the C_l and C_d time history has been shown in Figures 4.44 and 4.46 respectively in comparison to the experimental data obtained by Swalwell [6]. The comparison has been done for 500 convective time units (CTUs), as per the rough guidelines established by Garbaruk et al. [10] for spanwise effects for a geometry of span $4c$. Although the current geometry is not of span $4c$, the comparison can only be made valid by taking into account the right number of CTUs. The results obtained from the simulation were compared with for 40 inner iterations, as has been the case when comparing with other results from the literature for the validation studies.
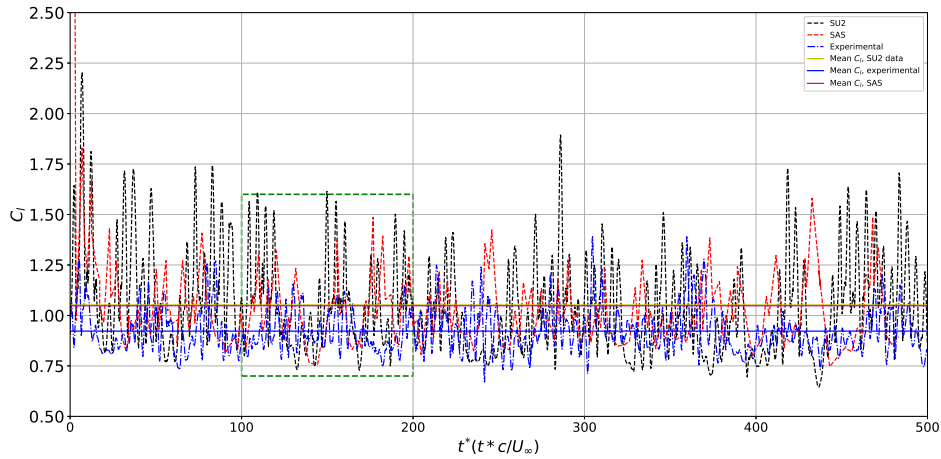
Figure 4.44: Variation of C_l vs. dimensionless time (t^*) using experimental [6], SLA-SGS (SU2) and SAS [18]

From Figure 4.44, it can be seen that although there is still an over-prediction of the lift coefficient time history from SU2 in comparison to the SAS results, the order of magnitude of C_l remains the same. The fluctuations corresponding to the time history of C_l are indeed, a consequence of the numerical setting used. Given that there is a 4th order scheme used in space for obtaining the SAS results, there is clearly a higher value of lift predicted by the 2nd order solver, which can be attributed to a poorer spatial accuracy of the 2nd order solver. Another interesting observation that can be made with regards to this is the fact that there is a periodic variation of C_l predicted by SU2 in comparison to the SAS results. This can be shown as a close-up view of the fluctuations in the initial time steps as shown in Figure 4.45, as the region within the green box as shown in Figure 4.44.
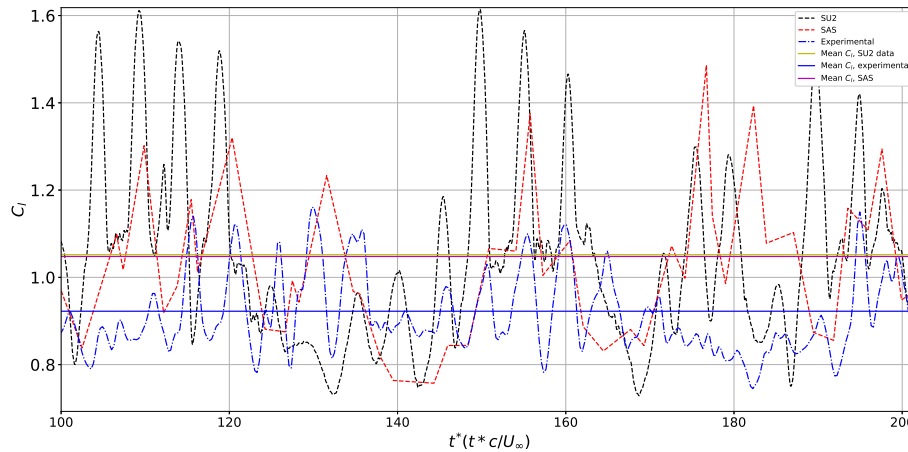
Figure 4.45: Close-up of variation of C_l with t^*

As we can observe in Figure 4.45, the variation of the C_l with t^* depicts an interesting relationship that gives an insight into the time step of the simulation. Notably, given that there are two different time steps, as described in more detail in sub-sub-section 3.1.4, have an influence on these trends as well, which can be observed in the following manner. As described by Gsell et al. [65] occurring in the case of a bluff body like a cylinder, the vortex shedding cycles corresponding to dual-time stepping schemes can have a two-fold effect, namely having two shedding periods, which was also observed as a multi-modal behaviour of the vortex shedding

modes. Quantitatively speaking, this is because of the fact that the local time step is impacted by the steady state CFL, that causes the distance between peaks to vary as shown in Figure 4.45. The SAS solution can also be seen to reflect this change, as the distance between two successive peaks seems to depict. Alternately, this could also indicate the presence of multi-modal behaviour that has been described in the literature [14]. The variation of C_d vs. t^* also shows a very similar variation as that observed in the C_l vs. t^* case, as shown in Figure 4.46.
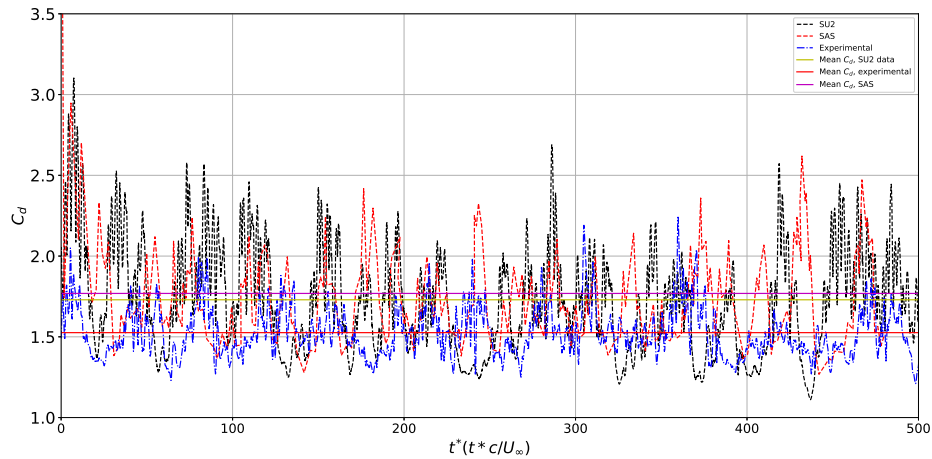
Figure 4.46: Variation of C_d vs. dimensionless time (t^*) using experimental [6], SLA-SGS (SU2 results) and SAS results [18]

Another interesting observation that can be made with regards to the mean of the coefficients. This can be summarized from the comparison of their values, that have been shown in Table 4.1.

Parameter	SLA-SGS (SU2)	SAS	Experiment
C_l	1.05197	1.04788	0.92236
C_d	1.72936	1.768696	1.52586

Table 4.1: Comparison of mean values of C_l from SU2, SAS [18] and experimental data [6]

From Table 4.1, it can be easily obtained that the discrepancy in the C_l value predicted by the SLA-SGS model using the SA turbulence model is slightly more over-predicted (14.05%) in comparison to the SAS model (13.61%). However, the C_d prediction speaks otherwise: the SAS model over-predicts the C_d (15.91%) in comparison to the SLA-SGS model (13.34%). This can be reasoned from the formulation of the turbulence models - the SAS turbulence model, as described by Menter [66], allows for the higher wave numbers to dissipate energy to the lower wave numbers rather than accumulating. This results in the necessary amount of eddy viscosity that has to be calculated in comparison to the SA model. However, since it is well-known from the literature that the S-A model performs poorly at the onset of adverse pressure gradients, as shown by Medida [32]. Therefore, this results in a delayed separation region, and hence, an over-predicted lift coefficient value. However, the discrepancy in the C_d over-prediction can be attributed to the fact that the SAS model takes into account a lower velocity gradient predicted in the separation regions, which causes the prediction of a high von Karman length scale. This results in a comparatively advanced transition from RANS to LES in comparison to SLA-SGS, which thus, causes the prediction of a higher drag coefficient due to a higher eddy viscosity generation.

For a more detailed statistical approach to the analysis of C_l and C_d, in accordance with the guidelines set the reader may have a further reading in Appendix C.

Validation of results from Winkler et al. [17]

In this sub-section, an effort was made to obtain a computational validation of the results obtained from SU2 with other solvers that have been developed in the past to solve the flow problem at hand. In particular, this sections describes an effort to validate the effect of using an SLA-SGS approach as against other SA turbulence models. This was done by using a solver BCFD, also using an SAS solver that can be potentially used as an alternative to the existing unsteady solver for SA-DDES in the CFD solver of Boeing named BCFD [17].

Furthermore, an additional motivation to pursue this investigation was to obtain the variation in the running spanwise averaged results of lift and drag with different kinds of meshes used, as well as SAS results, so that a more holistic and generalized comparison could be made in line with the mesh requirements that are needed in order to obtain a fruitful result. This is in line with the detailed statistical analysis of Garbaruk et al.[10] as well, in which a variability in the statistics could be obtained by investigating the running spanwise averaged trends of C_l and C_d.

In Winkler's investigation, a flow around the NACA 0021 airfoil was investigated at an angle of attack of 60° at a Reynolds number of 2.7×10^5, using BCFD.

Using the SAS turbulence model, the isotropic turbulence approach was also used to compare SAS with DDES on different grid levels and topologies. Therefore, different kinds of meshes were used, with the purpose of obtaining a comparative study between them. Using a domain having four chord lengths (with the chord being one inch), three different meshes were generated, by converting structured O-grids into unstructured grids. As far as the mesh topology was concerned, there were two different kinds of meshes used, namely the hexahedral and the mixed element meshes. The coarse, medium and fine hexahedral meshes had 0.42 million, 3.36 million and 26.88 million cells respectively, while the mixed element coarse, medium and fine mesh consisted of 2.06, 10.76 and 61.23 million cells respectively.

Given that the current mesh also used hexahedral elements, it would be useful to obtain insights as to how using a different mesh would have changed the results obtained. Therefore, this analysis would be useful for the purpose of comparing not only different turbulence models (S-A vs. SAS), but also different meshes (hexahedral vs. mixed).

The variation of the running (cumulative) spanwise-averaged C_l and C_d plots, averaged over the span, are given in Figures 4.47 and 4.48 respectively. The time averaging is performed for the parameters by taking into account the average value of the parameter from every preceding instant. The reason for choosing the initial range of 500 CTUs is because of the fact that according to the literature, it was mentioned that the transient effects of the solution would be absent after 400 CTUs.
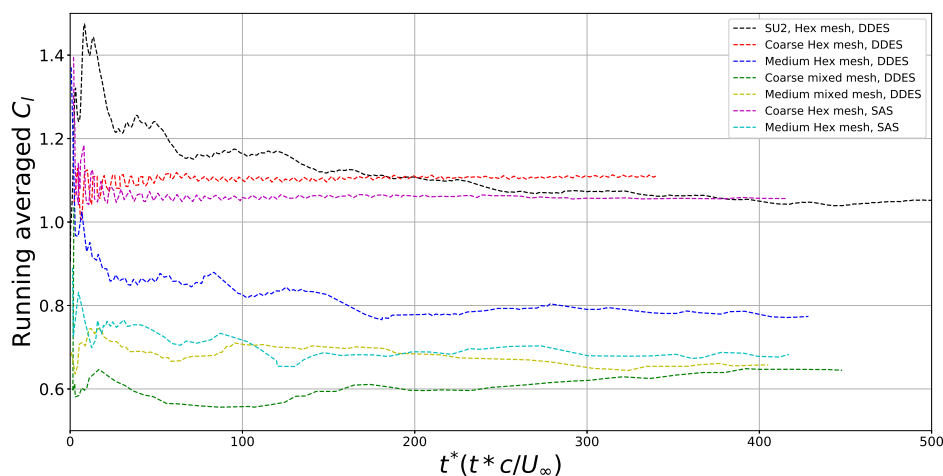
Figure 4.47: Running averaged variation of C_l compared with results from Winkler [17]

From Figure 4.47, it can be observed that while there is an initial over-prediction with the current grid, there is a period after 400 CTUs after which there seems to be a steady state reached for the C_l. The results obtained for a span of $1c$, however, is an encouraging sign, given that the literature predicts that this is only the case for an airfoil of span $4c$ ([10],[17]), and not for a span of $1c$. Furthermore, there is also a general observation that using a mixed kind of mesh (involving both tetrahedrons and hexahedrons) improves the convergence of the time averaged value, as is clearly predicted. Finally, the comparison with the SAS results, obtained on a hexahedral mesh, shows that an almost constant value of C_l can be reached even before 400 iterations are performed. This is also an encouraging sign to compare the results obtained from the regular S-A model with variations of the same model using the SAS approach.
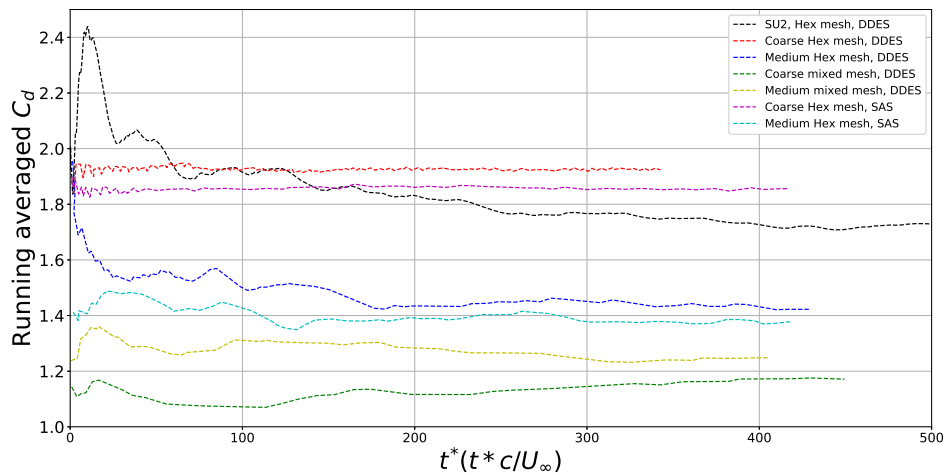
Figure 4.48: Running span-wise averaged variation of C_d compared with results from Winkler [17]

From Figure 4.48, it can be observed that in comparison to the time-averaged C_d, the result obtained from SU2 does not reach an almost constant value after 400 CTUs. This could be accounted for due to the fact that it is computationally a challenge to have obtained a converged C_d value within 500 CTUs. The SAS model, once again, seems to have obtained an improved convergence for a hexahedral mesh. This once again, provides an incentive for trying out the SAS approach in future investigations using the current mesh and span. Furthermore, this also means that there is a need to investigate the SU2 results a finer mesh and a mixed mesh with tetrahedrons and hexahedral elements, so that there would be a better insight that could be obtained for this analysis. The need for a finer mesh is also highlighted in the results obtained from the DDES approach using two different meshes - the medium hexahedral converges much faster in comparison to the coarse hexahedral mesh. Furthermore, the medium mixed mesh converges slower than the coarse mixed mesh. This implies that having a mixed mesh using the DDES mesh would not necessarily be useful using the S-A model.

Once these studies have been performed, it would now be a good opportunity to revisit the research questions in order to provide answers to them.

4.6. Revisiting research questions

As a precursor to the conclusion, this section provides an attempt to revisit the sub-research questions described in Section 2.2. These are, therefore, answered in a systematic manner as described as follows.

1. *What is the influence of the hybrid SGS model on the performance characteristics of the airfoil?*
   Ans: The hybrid SGS model was found to provide a reasonable estimate of the aerodynamic performance parameters that were taken into consideration (C_l, C_d, C_n and C_t).

This was, however, also affected by the fact that having a geometry of span $1c$ did impact the over-prediction of the results. Therefore, there is a requirement to use a geometry of a greater span to further explore the possibilities of using this in comparison with other hybrid SGS cases. The comparison with the 2D sectional values obtained from a basic force analysis of all the forces acting on the airfoil did give an insight into what could have changed in comparison to other studies in the literature that performed similar studies.

2. *What is the influence of increasing the number of inner iterations on the performance characteristics of the airfoil?*
   Ans: It became very clear from the PSD plots for the various aerodynamic coefficients that increasing the number of inner iterations did cause the vortex shedding peaks (the major and the first harmonic) to shift towards that obtained from the experiment. This shows that increasing the number of inner iterations definitely increased the accuracy of the solution, albeit the magnitude of the time history and PSD plots remained more or less the same. However, it was also the effect of this shift diminished after 40 inner iterations. This was also the reason why having 40 inner iterations was used for the purpose of comparing the results with other validation cases available in the literature, as well as when comparing with other turbulence models and even meshes.

3. *What is the influence of the hybrid SGS model on the determination of accurate flow physics?*
   Ans: The hybrid SGS model that has been used for the purpose of comparing the simulation results in this thesis, which is the shear-layer adapted sub-grid scale (SLA-SGS) model, was found to provide a good insight into the shear layer instabilities of the flow problem from the contours of the Q-criterion, and was also able to predict the first harmonic of the peak corresponding to vortex shedding, which was definitely an improvement compared to the other SGS models available in the literature. The constant shift in the vortex shedding peak, that was caused due to the definition of the wake length being used to define the Strouhal number, clearly affected the predicted peaks. This was because of an inconsistency in the literature with regards to using this convention of the characteristic length scale used. The over-prediction in the magnitudes of the PSD plots remained as a result of the geometry haing a finite span. However, the use of a less dissipative numerical scheme (the NTS in this case) improved the prediction of the harmonic corresponding to vortex shedding.

Now that the answers to the sub-research questions have been obtained, the next step of the thesis to provide a conclusion to the thesis. This would be useful to provide logical conclusions to not only summarize the findings from thesis, but also to provide a point where the thesis can be reflected upon.

5

Conclusion

This chapter summarizes the major structure of this thesis, along with the major findings that have been obtained. The thesis begins with an introduction of the problem statement in Chapter 1. The motivation behind pursuing it from the context of the industry as well as a research problem. This motivation is obtained as a research gap that is found from the literature in Chapter 2. Next, the simulation setup is provided, which provides information regarding the freestream settings and the numerical schemes used in Chapter 3. The results are then presented in the order in which the simulations were performed, namely RANS 1st and 2nd orders, followed by the DDES 2nd order simulation. From the RANS simulations, it was pretty evident that the unsteady flow phenomena could not be captured because of the inherently steady nature of RANS. Furthermore, because RANS does not involve the resolution of the finest turbulent flow structures, a lot of the three-dimensionality of the flow, such as vortex shedding and vortex roll-up, could be captured using RANS as well. Therefore, the DDES results were explored in a lot more detail. The results obtained from the 3D lift and drag coefficients only improved with the increase in the number of inner iterations (in terms of the mean value of the lift and drag coefficient, as well as their corresponding errors compared with the experiment). While there was a constant shift in the values of the Strouhal peaks, that was accounted as a matter of fact, due to the inconsistency in the length scale taken in the literature. This has been found to show up in almost all analyses performed. Furthermore, given the fact that there is a discrepancy obtained for calculating the PSD formulation using different numerical schemes, there is a further need to investigate the validity of the schemes obtained from the literature. The presence of chaotic fluctuations also confirmed the stochastic nature of the simulation. Another interesting finding that was performed was for the impact of the number of inner iterations on the aerodynamic coefficients used to describe the flow problem. It was found that while the solution did improve in terms of the prediction of the vortex shedding and first harmonic peaks from 10 to 20 inner iterations, the solution did not dramatically improve when the number of inner iterations were changed from 20 to 40. This led to the conclusion that the solution did not have an appreciably improved accuracy after 40 inner iterations.

Furthermore, as confirmed by the literature, the results predicted from the simulations were also over-predicted due to the narrow span of the existing geometry, as was mentioned earlier by Garbaruk [10]. Therefore, there is a need to perform the same analysis, but using a geometry with a larger span. The next part of the results section involved the comparison of the 3D results with a 2D spanwise averaged results, that gave a conclusion that it was indeed, the spanwise results that could be improved on by correcting them with empirical coefficients that provide an insight into the correction effects that would take place to match results with experimental data. The results section was then concluded with multiple validation studies performed with the results obtained from experimental data, different SGS models, and different meshes (based on grid size and topology). It was found that on comparison with experimental data, there was a discrepancy that was caused because the re-created PSD plots did not match with that obtained from the experiment. Furthermore, the re-created hybrid SGS plots were also quite different from the ones obtained from the findings of Molina [12].

6

Future Recommendations

This chapter describes the future recommendations that can be done for the purpose of improving the results from the current thesis. These can be categorized based on the studies that are performed during the thesis.

6.1. Simulation Setup

Given that the freestream settings cannot be modified, the simulation setup can only be changed in the numerical settings, that is, the spatial and temporal discretization aspects of the setup. Therefore, the following changes are suggested from the spatial discretization point of view:

1. Given that the spatial discretization was performed by using a second order scheme (a low-dissipation AUSM scheme was used with an alternate pressure flux formulation), it is advisable that given the over-prediction of various performance parameters, a higher order scheme (preferably a 3rd or 4th order scheme) be used in space, so that a more accurate value be obtained. The proof of an improved spatial scheme can also be observed in the findings of Patel et al. [18], wherein improved comparison with the experimental findings were obtained using a higher order scheme.

2. The slope limiter used was the VENKATAKRISHNAN limiter as described by Venkatakrishnan [67] to obtain a converged and steady state solution for upwind schemes by imposing a monotonicity condition. Given that there is a still a scope to obtain a solution with even lower density residuals, one can adopt an approach to obtain such a solution by trying a more dissipative scheme, but adding slope limiters that take into account the convergence difficulties obtained in adaptive grids as obtained by Wang [68], or else, adopting a different approach to enforcing monotonicity on the solution by ensuring that the solution does not exceed the maximum and minimum values at the neighbours of the control volumes as shown by Barth and Jespersen [69].

3. There is an option to introduce a parameter that can emulate the characteristic features of central differencing schemes such as the JST and the Lax-Friedrich ones in terms of setting a lower bound of numerical dissipation. This can be achieved by using the ENTROPY_FIX_COEFF setting, which essentially puts a limit on the convective Eigenvalue. Although this is more suitable for flows with shocks, it has been found that this method also works well for low Mach number flows.

4. A comparative study of the different kinds of low-dissipation Roe schemes can be performed, in order to provide the correct distinction between the various low-dissipation functions available, such as the FD scheme (based specifically on the DDES method's f_d function as described in detail in Section 3.8), the NTS scheme (Travin and Shur's blending function approach [54] used for the present simulation) and the absence of any dissipation. This would provide a good insight into whether having a separate low dissipation function is necessary to avoid numerical noise, or if there is a requirement to use a low-dissipation Roe scheme entirely.

From the temporal discretization point of view, there are also the following suggestions that could be taken into account:

1. Although Euler implicit schemes are quite suitable for the purpose of stability and convergence, they can still be quite heavy on memory requirements, as is the nature of implicit calculations. Therefore, there can be a comparative study by using an explicit scheme using different unsteady CFL numbers. This would provide a much better comparison with respect to the memory requirements.

2. The time step, although calculated based on the flow physics to be investigated, could have an independent study in which a varying time step could be investigated, so that the impact of having a smaller or larger time step would have on the final solution, as well as the overall convergence of the simulation.

3. Given that increasing the number of inner iterations does not improve the convergence of the solution, an investigation with different convective CFLs can also be performed, so that the impact on the flow solution can be studied.

4. As is the case with the use of variants of Roe's scheme in low Mach numbers, there could be the use of different preconditioning schemes that could be studied for the purpose of accelerating convergence. In the current solver, the Implicit Lower Upper (ILU) solver, as described in sub-section 3.1.5, however, the more cost effective schemes can be tried, such as the Lower-Upper Symmetric Gauss-Seidel (LU-SGS) and the Jacobi options.

6.2. Turbulence model settings

1. From the turbulence model point of view, it is a well-known fact that the S-A model tends to perform poorly in the onset of adverse pressure gradients [32]. Therefore, it would be wise to operate with other models as well (possible variants of S-A, such as using an SAS approach), so that the onset of boundary layer separation is not delayed.

2. SU2 also has additional S-A variants that take into account compressibility effects, and hence, that is also another variant that could be tried and tested for future analyses.

6.3. Mesh settings

The mesh settings that were used in this simulation involved the use of an O-grid, whose coarse version has been used in the literature in the past. However, it has been clearly found from the results described that there is an over-prediction of a majority of the performance parameters, and therefore, there is a need to investigate the mesh settings better. Some of the suggestions for this purpose are as follows:

1. The use of a finer mesh, as suggested by Molina et al. [12], would serve the purpose of investigating the validity of the current hybrid SGS model on improving the performance coefficients. Although grid refinement does not make a significant impact to the results as suggested by the DESider project [14], the effect of the SLA-SGS model to facilitate the study of the spanwise effects would be quite helpful.

2. Given that the current geometry has a unit span (specifically in the current case, a span of $1c$), it is important to increase the span to upto $4c$. This is important in order to make a better estimate of the validity of the existing comparisons with the literature (both experimental and computational data). This is in accordance with the findings of the DESider project [14].

3. In light of the comparison made with results from Winkler in Section 4.5.4, The use of other meshes, such as a C-type or the H-type (a hybrid of the C and O type), could be tried out, in order to test the impact of different mesh strategies on the solution and the performance parameters.

6.4. Acoustics analysis

Although a detailed account of the acoustics code will be given in the appendix B.1, it is only imperative to provide useful recommendations for future analyses, some of which include:

1. Various kind of observer orientations can be tried out, apart from the circular kind shown in Figure B.2, such as an elliptical one, a rectangular one and so on, such that the variation of the pressure spectrum obtained can be compared.

2. The current formulation only has the solid formulation of the FW-H equations, that would provide an insight into the noise generated by the monopole and dipole sources of sound. However, as has been recently obtained from the work of Kim and Turner [70], there is a possibility that quadrupole noise could dominate dipole noise at post-stall angles, although at low Mach numbers, Lighthill's theory [71] predicts otherwise. Therefore, a future study could confirm whether such a prediction holds true for deep stall as well or not.

3. The current formulation still misses the presence of a permeable surface. If such a formulation could be specified within the code, then it would be easier to calculate the noise from quadrupole sources of sound.

As far as post-processing analysis is concerned, there can also be a comment to try different kinds of filters, apart from the one used in the results obtained. This is simply in order to ensure that at lower frequencies, the spectrum is not entirely dampened out.

To conclude, future studies should be conducted to investigate the multi-modal behaviour of the flow physics. Therefore, a general recommendation would be to perform additional studies involving performing a proper orthogonal decomposition (POD) study involving multiple modes involved in the flow. This would possibly allow one to explore the complexity in the flow physics.

Bibliography

[1] William J McCroskey. "Unsteady airfoils". In: *Annual review of fluid mechanics* 14.1 (1982), pp. 285–311.

[2] Alex Laratro et al. "A discussion of wind turbine interaction and stall contributions to wind farm noise". In: *Journal of Wind Engineering and Industrial Aerodynamics* 127 (2014), pp. 1–10.

[3] J Yan, C Mockett, and F Thiele. "Investigation of alternative length scale substitutions in detached-eddy simulation". In: *Flow, Turbulence and Combustion* 74.1 (2005), pp. 85–102.

[4] Jacob M Turner and Jae Wook Kim. "Aerofoil dipole noise due to flow separation and stall at a low Reynolds number". In: *International Journal of Heat and Fluid Flow* 86 (2020), p. 108715.

[5] Giovanni Lacagnina et al. "Mechanisms of airfoil noise near stall conditions". In: *Physical Review Fluids* 4.12 (2019), p. 123902.

[6] Katrina E Swalwell, John Sheridan, WH Melbourne, et al. "The effect of turbulence intensity on stall of the NACA 0021 aerofoil". In: *14th Australasian fluid mechanics conference*. 2001, pp. 10–14.

[7] M Shur et al. "Detached-eddy simulation of an airfoil at high angle of attack". In: *Engineering turbulence modelling and experiments 4*. Elsevier, 1999, pp. 669–678.

[8] M Strelets. "Detached eddy simulation of massively separated flows". In: *39th Aerospace sciences meeting and exhibit*. 2001, p. 879.

[9] PR Spalart. "Comments on the feasibility of LES for wings, and on hybrid RANS/LES approach, advances in DNS/LES". In: *Proceedings of 1st AFOSR International Conference on DNS/LES, 1997*. 1997.

[10] A Garbaruk et al. "Evaluation of time sample and span size effects in DES of nominally 2D airfoils beyond stall". In: *Progress in hybrid RANS-LES modelling*. Springer, 2010, pp. 87–99.

[11] Hong-Sik Im and Ge-Cheng Zha. "Delayed detached eddy simulation of airfoil stall flows using high-order schemes". In: *Journal of Fluids Engineering* 136.11 (2014).

[12] Eduardo Molina et al. "Hybrid rans/les calculations in su2". In: *23rd AIAA computational fluid dynamics conference*. 2017, p. 4284.

[13] Alex Laratro et al. "Self-noise of NACA 0012 and NACA 0021 aerofoils at the onset of stall". In: *International Journal of Aeroacoustics* 16.3 (2017), pp. 181–195.

[14] Werner Haase, Marianna Braza, and Alistair Revell. *DESider–A European Effort on Hybrid RANS-LES Modelling: Results of the European-Union Funded Project, 2004-2007*. Vol. 103. Springer Science & Business Media, 2009.

[15] Arthur Fage and FC Johansen. "XLII. The structure of vortex sheets". In: *The London, Edinburgh, and Dublin Philosophical Magazine and Journal of Science* 5.28 (1928), pp. 417–441.

[16] Ye Zhang, Alexander van Zuijlen, and Gerard van Bussel. "Massively separated turbulent flow simulation around non-rotating MEXICO blade by means of RANS and DDES approaches in OpenFOAM". In: *33rd AIAA Applied Aerodynamics Conference*. 2015, p. 2716.

[17] Chad Winkler, Andrew Dorgan, and Mortaza Mani. "Scale adaptive simulations of turbulent flows on unstructured grids". In: *20th AIAA Computational Fluid Dynamics Conference*. 2011, p. 3559.

[18]   Purvic Patel, Yunchao Yang, and Gecheng Zha. "Scale Adaptive Simulation of stalled NACA 0012 airfoil using high order schemes". In: *AIAA Aviation 2019 Forum*. 2019, p. 3527.

[19]   Stéphane Moreau, Michel Roger, and Julien Christophe. "Flow features and self-noise of airfoils near stall or in stall". In: *15th AIAA/CEAS Aeroacoustics Conference (30th AIAA Aeroacoustics Conference)*. 2009, p. 3198.

[20]   Frank M White and Joseph Majdalani. *Viscous fluid flow*. Vol. 3. McGraw-Hill New York, 2006.

[21]   Claus Wagner, Thomas Hüttl, and Pierre Sagaut. *Large-eddy simulation for acoustics*. Vol. 20. Cambridge University Press, 2007.

[22]   Akihiro Tadamasa and Mehrdad Zangeneh. "Numerical prediction of wind turbine noise". In: *Renewable energy* 36.7 (2011), pp. 1902–1912.

[23]   Jaber H Almutairi, Lloyd E Jones, and Neil D Sandham. "Intermittent bursting of a laminar separation bubble on an airfoil". In: *AIAA journal* 48.2 (2010), pp. 414–426.

[24]   William R Wolf and Sanjiva K Lele. "Trailing-edge noise predictions using compressible large-eddy simulation and acoustic analogy". In: *AIAA journal* 50.11 (2012), pp. 2423–2434.

[25]   Bram Van Leer. "Towards the ultimate conservative difference scheme. V. A second-order sequel to Godunov's method". In: *Journal of computational Physics* 32.1 (1979), pp. 101–136.

[26]   Philip L Roe. "Approximate Riemann solvers, parameter vectors, and difference schemes". In: *Journal of computational physics* 43.2 (1981), pp. 357–372.

[27]   Eiji Shima and Keiichi Kitamura. "Parameter-free simple low-dissipation AUSM-family scheme for all speeds". In: *AIAA journal* 49.8 (2011), pp. 1693–1709.

[28]   N Sørensen et al. "Power curve predictions wp2 deliverable 2.3". In: *Technical Report* (2014).

[29]   CD Argyropoulos and NC Markatos. "Recent advances on the numerical modelling of turbulent flows". In: *Applied Mathematical Modelling* 39.2 (2015), pp. 693–732.

[30]   Stephen B Pope. *Turbulent flows*. 2001.

[31]   Philippe Spalart and Steven Allmaras. "A one-equation turbulence model for aerodynamic flows". In: *30th aerospace sciences meeting and exhibit*. 1992, p. 439.

[32]   Shivaji Medida. "Correlation-based transition modeling for external aerodynamic flows". PhD thesis. University of Maryland, College Park, 2014.

[33]   Florian R Menter. "Two-equation eddy-viscosity turbulence models for engineering applications". In: *AIAA journal* 32.8 (1994), pp. 1598–1605.

[34]   David C Wilcox. "Reassessment of the scale-determining equation for advanced turbulence models". In: *AIAA journal* 26.11 (1988), pp. 1299–1310.

[35]   Paul G Tucker and James C Tyacke. "Eddy resolving simulations in aerospace–Invited paper (Numerical Fluid 2014)". In: *Applied Mathematics and Computation* 272 (2016), pp. 582–592.

[36]   Philippe R Spalart. "Strategies for turbulence modelling and simulations". In: *International journal of heat and fluid flow* 21.3 (2000), pp. 252–263.

[37]   Philippe R Spalart. "Detached-eddy simulation". In: *Annual review of fluid mechanics* 41 (2009), pp. 181–202.

[38]   Robert S Rogallo and Parviz Moin. "Numerical simulation of turbulent flows". In: *Annual review of fluid mechanics* 16.1 (1984), pp. 99–137.

[39]   Jochen Fröhlich and Dominic Von Terzi. "Hybrid LES/RANS methods for the simulation of turbulent flows". In: *Progress in Aerospace Sciences* 44.5 (2008), pp. 349–377.

[40]   Lars Davidson and Simon Dahlström. "Hybrid LES-RANS: An approach to make LES applicable at high Reynolds number". In: *International journal of computational fluid dynamics* 19.6 (2005), pp. 415–427.

[41] Lars Davidson. *Fluid mechanics, turbulent flow and turbulence modeling*. 2015.

[42] Sébastien Deck. "Recent improvements in the zonal detached eddy simulation (ZDES) formulation". In: *Theoretical and Computational Fluid Dynamics* 26.6 (2012), pp. 523–550.

[43] ES Molina. "Detached Eddy Simulation in SU2". PhD thesis. Ph. D. thesis, Aeronautical Institute of Technology, 2018.

[44] FR Menter and M Kuntz. "Adaptation of eddy-viscosity turbulence models to unsteady separated flow behind vehicles". In: *The aerodynamics of heavy vehicles: trucks, buses, and trains*. Springer, 2004, pp. 339–352.

[45] Christophe Bogey, Olivier Marsden, and Christophe Bailly. "Large-eddy simulation of the flow and acoustic fields of a Reynolds number 10 5 subsonic jet with tripped exit boundary layers". In: *Physics of Fluids* 23.3 (2011), p. 035104.

[46] Philippe R Spalart et al. "A new version of detached-eddy simulation, resistant to ambiguous grid densities". In: *Theoretical and computational fluid dynamics* 20.3 (2006), pp. 181–195.

[47] Michael L Shur et al. "Evaluation of vortex generators for separation control in a transcritical cylinder flow". In: *AIAA Journal* 53.10 (2015), pp. 2967–2977.

[48] Sébastien Deck. "Numerical simulation of transonic buffet over a supercritical airfoil". In: *AIAA journal* 43.7 (2005), pp. 1556–1566.

[49] Charles Mockett et al. "Two non-zonal approaches to accelerate RANS to LES transition of free shear layers in DES". In: *Progress in hybrid rans-les modelling*. Springer, 2015, pp. 187–201.

[50] Thomas D Economon et al. "SU2: An open-source suite for multiphysics simulation and design". In: *Aiaa Journal* 54.3 (2016), pp. 828–846.

[51] S Vitale, M Pini, and P Colonna. "Multistage Turbomachinery Design Using the Discrete Adjoint Method Within the Open-Source Software SU2". In: *Journal of Propulsion and Power* 36.3 (2020), pp. 465–478.

[52] Sparsh Sharma et al. "Numerical investigation of noise generation by rod-airfoil configuration using DES (SU2) and the FW-H analogy". In: *25th AIAA/CEAS Aeroacoustics Conference*. 2019, p. 2400.

[53] Ruben Sanchez et al. "Assessment of the fluid-structure interaction capabilities for aeronautical applications of the open-source solver SU2". In: (2016).

[54] A Travin et al. "Physical and numerical upgrades in the detached-eddy simulation of complex turbulent flows". In: *Advances in LES of complex flows*. Springer, 2002, pp. 239–254.

[55] Antony Jameson. "Time dependent calculations using multigrid, with applications to unsteady flows past airfoils and wings". In: *10th Computational Fluid Dynamics Conference*. 1991, p. 1596.

[56] Yousef Saad. "ILUT: A dual threshold incomplete LU factorization". In: *Numerical linear algebra with applications* 1.4 (1994), pp. 387–402.

[57] Zhixiang Xiao et al. "Numerical dissipation effects on massive separation around tandem cylinders". In: *AIAA journal* 50.5 (2012), pp. 1119–1136.

[58] Zhixiang Xiao et al. "Comparisons of three improved DES methods on unsteady flows past tandem cylinders". In: *Progress in Hybrid RANS-LES Modelling*. Springer, 2012, pp. 231–243.

[59] Mikhail L Shur et al. "An enhanced version of DES with rapid transition from RANS to LES in separated flows". In: *Flow, turbulence and combustion* 95.4 (2015), pp. 709–737.

[60] Francisco Palacios et al. "Stanford university unstructured (su 2): an open-source integrated computational environment for multi-physics simulation and design". In: *51st AIAA aerospace sciences meeting including the new horizons forum and aerospace exposition*. 2013, p. 287.

[61] Kudret Baysal and Ulrich Rist. "Identification and quantification of shear layer influences on the generation of vortex structures". In: *New Results in Numerical and Experimental Fluid Mechanics VII*. Springer, 2010, pp. 241–248.

[62] John David Anderson Jr. *Fundamentals of aerodynamics*. Tata McGraw-Hill Education, 2010.

[63] C Mockett, U Bunge, and F Thiele. "Turbulence modelling in application to the vortex shedding of stalled airfoils". In: *Engineering Turbulence Modelling and Experiments 6*. Elsevier, 2005, pp. 617–626.

[64] Yu Egorov and F Menter. "Development and application of SST-SAS turbulence model in the DESIDER project". In: *Advances in Hybrid RANS-LES Modelling*. Springer, 2008, pp. 261–270.

[65] Simon Gsell, Umberto D'ortona, and Julien Favier. "Multigrid dual-time-stepping lattice Boltzmann method". In: *Physical Review E* 101.2 (2020), p. 023309.

[66] FR Menter and Y Egorov. "The scale-adaptive simulation method for unsteady turbulent flow predictions. Part 1: theory and model description". In: *Flow, turbulence and combustion* 85.1 (2010), pp. 113–138.

[67] Venkat Venkatakrishnan. "On the accuracy of limiters and convergence to steady state solutions". In: *31st Aerospace Sciences Meeting*. 1993, p. 880.

[68] ZJ Wang. "A fast nested multi-grid viscous flow solver for adaptive Cartesian/Quad grids". In: *International Journal for Numerical Methods in Fluids* 33.5 (2000), pp. 657–680.

[69] Timothy Barth and Dennis Jespersen. "The design and application of upwind schemes on unstructured meshes". In: *27th Aerospace sciences meeting*. 1989, p. 366.

[70] Jacob Turner and Jae Woook Kim. "Quadrupole noise generated from a low-speed aerofoil in near-and full-stall conditions". In: *Journal of Fluid Mechanics* (2021).

[71] Michael James Lighthill. "On sound generated aerodynamically I. General theory". In: *Proceedings of the Royal Society of London. Series A. Mathematical and Physical Sciences* 211.1107 (1952), pp. 564–587.

[72] Peter Welch. "The use of fast Fourier transform for the estimation of power spectra: a method based on time averaging over short, modified periodograms". In: *IEEE Transactions on audio and electroacoustics* 15.2 (1967), pp. 70–73.

[73] Eduardo Molina et al. "Flow and noise predictions around tandem cylinders using DDES approach with SU2". In: *AIAA Scitech 2019 Forum*. 2019, p. 0326.

[74] JE Ffowcs Williams and LH Hall. "Aerodynamic sound generation by turbulent flow in the vicinity of a scattering half plane". In: *Journal of fluid mechanics* 40.4 (1970), pp. 657–670.

[75] N Curle. "The influence of solid boundaries upon aerodynamic sound". In: *Proceedings of the Royal Society of London. Series A. Mathematical and Physical Sciences* 231.1187 (1955), pp. 505–514.

[76] F Farassat and MK Myers. "The Kirchhoff formula for a supersonically moving surface". In: (1996).

[77] Anastasios S Lyrintzis. "Surface integral methods in computational aeroacoustics—From the (CFD) near-field to the (Acoustic) far-field". In: *International journal of aeroacoustics* 2.2 (2003), pp. 95–128.

[78] Ivan E Sutherland, Robert F Sproull, and Robert A Schumacker. "A characterization of ten hidden-surface algorithms". In: *ACM Computing Surveys (CSUR)* 6.1 (1974), pp. 1–55.

[79] Andrey Nikolaevich Kolmogorov. "The local structure of turbulence in incompressible viscous fluid for very large Reynolds numbers". In: *Cr Acad. Sci. URSS* 30 (1941), pp. 301–305.

A
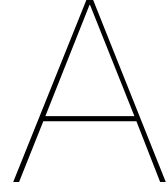
Appendix A

A.1. Power Spectral Density

The PSD of C_l is calculated by using the formulation given by Welch's method [72], which takes the average of the periodogram that is given by the spectrum, as shown in Equation A.1.

$$\hat{P(f_n)} = \frac{1}{K} \sum_{j=0}^{L-1} I_k(f_n)$$ (A.1)

Here, $I_k(f_n)$ is the modified periodogram, given by Equation A.3, and W(j) is the weighting function. U is the average of the square of the weighing function, given by Equation A.2.

$$U = \frac{1}{L} \sum_{j=0}^{L-1} W^2(j)$$ (A.2)

In this case, the Hamming weighting function was taken into consideration, that is described in much more detail in Section A.2.

$$I_k(f_n) = \frac{L}{U} |A_k(n)|^2, \ \ k = 1, 2, ...K$$ (A.3)

Where A_1, A_2, ... , A_n are finite Fourier transforms of data set $X(j)$, as given by Equation A.4. f_n is the sampling frequency, given by $f_n = \frac{n}{L}$, where n = 0,1,...L/2.

$$A_k(n) = \frac{1}{L} \sum_{j=0}^{L-1} X_k(j)W(j)e^{-2kij\,n/L}$$ (A.4)

For the purpose of all the calculations, there were 5000 samples used for calculating the PSD, which was deemed to be sufficient as per the definition of Nyquist's criterion to capture the vortex shedding obtained in this analysis, which was found to be of the order of about 10^1 Hz.

However, in the literature, it has been found that the formulation for PSD obtained in the literature was given by Equation A.5.

$$PSD = \lim_{N \to \infty} \frac{(\Delta t)^2}{T} fft(quantity)$$ (A.5)

On comparing the PSD formulae given in Equations A.5 and the Welch's approach A.1, it is very clear that there is a discrepancy of Δt that can be obtained. This was noticed when trying to reproduce the results obtained from the experimental time series as well, to compare the plots obtained in the PSD. This is shown in Figure A.1, wherein the re-created experimental plot was also obtained by using the Welch's approach that is commonly used in signal processing.
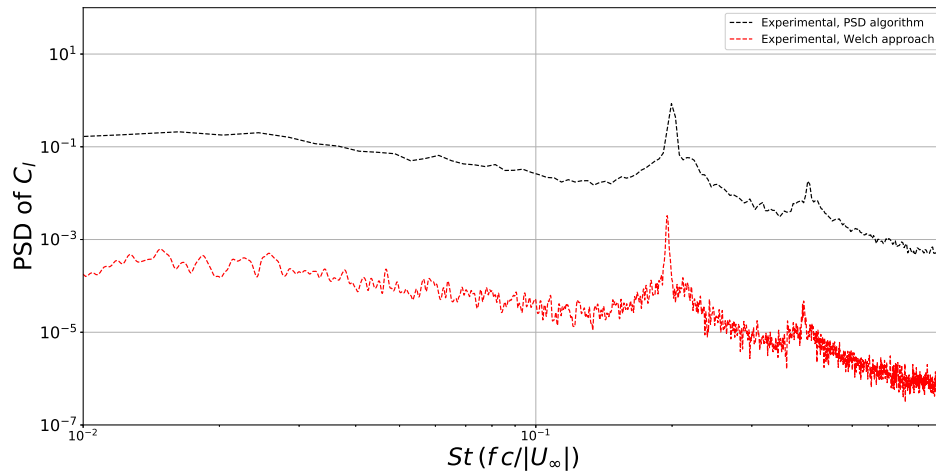
Figure A.1: Discrepancy obtained from PSD calculation of C_l obtained from SU2 and sectional results with Swalwell's paper with Equation A.5

From Figure A.1, the discrepancy is quite clear, and it is due to the fact that there is a discrepancy in the comparison of results that could be found in the literature. This was found to be the case, because the results obtained from the paper of Molina [12] seemed to have matched the results using the same formulation, which was not the case. This was also be found to be reflected in the 2D calculations as well, as can be observed in Figure A.2.
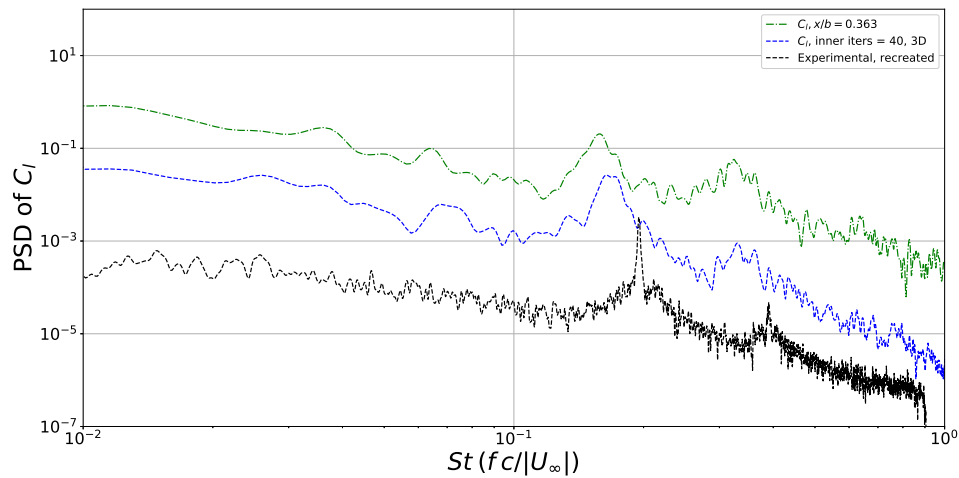
Figure A.2: Variation of PSD of C_l with St, compared with sectional 2D values and recreated PSD from Swalwell's experimental time series [6]

From Figure A.2, it is very clear that there is a discrepancy that is also predicted by the 2D C_l values as well, as compared to the experimental data. The remaining performance parameters also reflect this change, as can be observed in Figures A.3, A.4 and A.5 respectively.
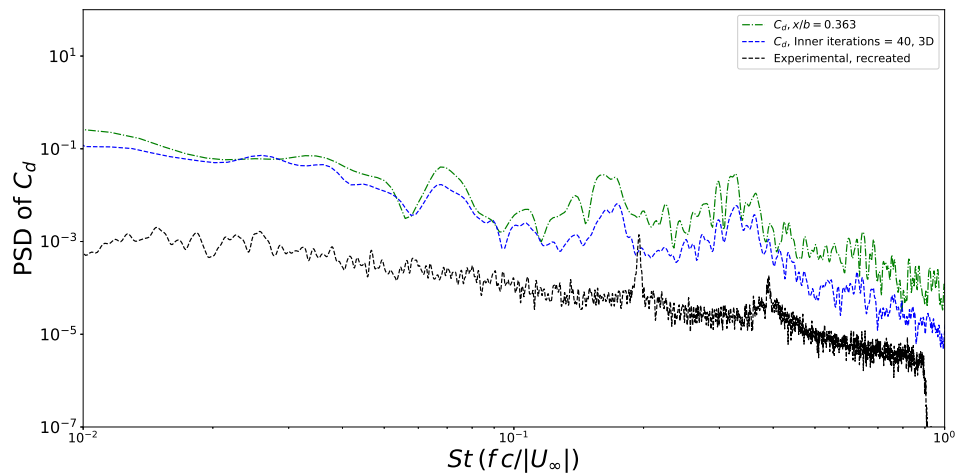
Figure A.3: Variation of PSD OF C_d with St, compared with sectional 2D values and recreated PSD from Swalwell's experimental time series [6]

From Figure A.3, it is clear that the discrepancy of dt still holds with the magnitude of PSD. However, one good indication of the correctness of the solution is the presence of both the vortex shedding and the harmonic of vortex shedding peaks as predicted by the 3D SU2 solution. The Strouhal peak corresponding to vortex shedding in this case was off from the experimental value by 8.44%.
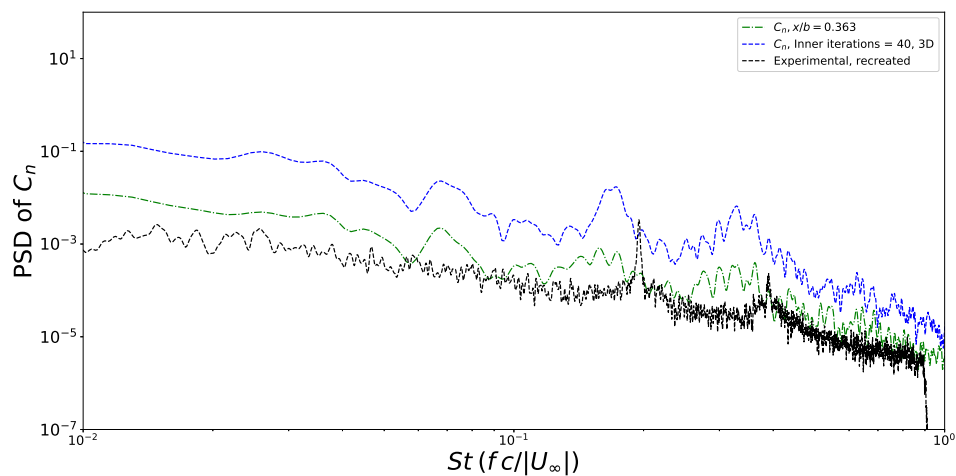
Figure A.4: Variation of PSD OF C_n with St, compared with recreated PSD from Swalwell's experimental time series [6]

From Figure A.4, it can be observed that akin to the PSD predicted by C_d, one can observe the presence of two distinct peaks, each of which correspond to the vortex shedding and harmonic of vortex shedding peaks respectively. This can be primarily seen only in the 3D C_n trend. However, their magnitudes are off by approximately 8.9% and 5.36% respectively. Furthermore, there is the presence of additional peaks, that are a result of the nature of the grid itself being coarse. The major point of difference compared to the other coefficients in this case is that the C_n trend predicted by the 2D case is under-predicted compared to the 3D case.
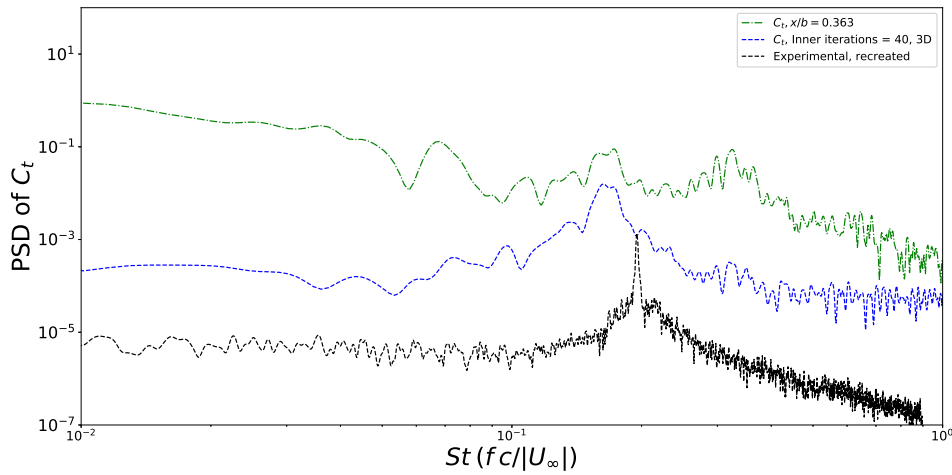
Figure A.5: Variation of PSD OF C_t with St, compared with recreated PSD from Swalwell's experimental time series
[6]

From Figure A.5, it can be observed that unlike the other coefficients, there is only a single peak, that corresponds to the vortex shedding frequency (the Strouhal number from the experiment comes out to be 0.225, while the one predicted by SU2 is 0.206). The absence of the harmonic of vortex shedding Strouhal peak in both PSD predictions can be reasoned because of the fact that there is vortex roll-up according to the findings of Lacagnina [5] only in the lateral direction and not in the tangential direction.

To summarize, all the plots clearly show the over-prediction compared to the experimental PSD, as depicted in their corresponding time history plots. The only exception to this is the sectional C_n plot, which is under-predicted compared to the corresponding 3D value. The much larger over-prediction of the sectional C_t plot compared to the sectional C_n plot also contributes to the fact that there is an overall over-prediction of the C_l and C_d values.

A.2. Hamming weighing

There is an additional Hamming weighting that is applied on the data along with the Welch's approach in order to remove the nearest side lobes. This is done by using the Hamming weight, that is defined by Equation A.6.

$$w(n) = 0.5 - 0.5cos\left(\frac{2\pi n}{M-1}\right) \quad 0 \leq n \leq M-1 \tag{A.6}$$

Where M is the number of samples that could be used to remove the spurious vectors, and n is the number of samples used. In a graphical form, this can be represented by Figure A.6.
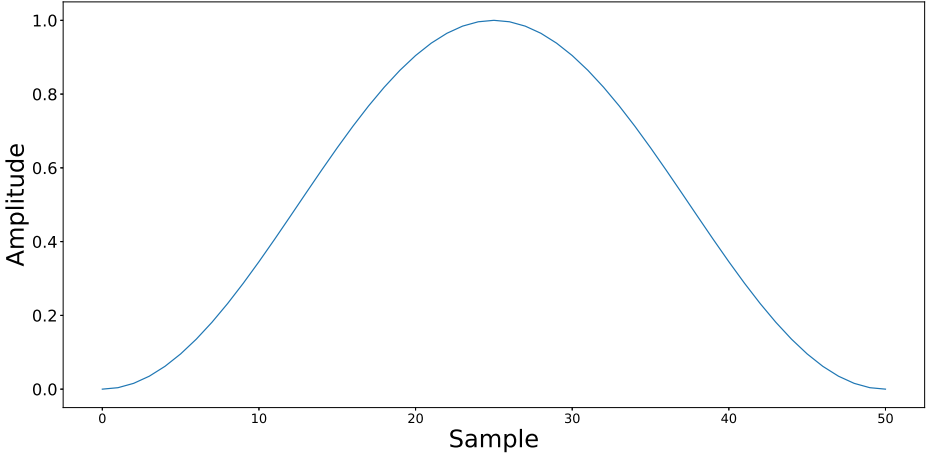
Figure A.6: Hamming window

B

Appendix B

B.1. Acoustics solver in SU2

In this section, a glimpse into the working of the acoustics solver setup in SU2 has been described. This was found by fixing the sampling frequency, which has been done in Section 3.2. The code discussed in this section was used to obtain the results for a test case of tandem cylinders [73].

B.2. A brief introduction of the FW-H equations

Ffowcs-William and Hawking [74] later extended Curles' theorem [75] to incorporate moving, physical, non-deformable surfaces, and generalized Lighthill's analogy. This was done by first introducing a Heaviside step function to the source terms of the continuity and momentum equations, combining them, and then solving for the pressure fluctuations by using Green's function. The final form of the FW-H equation, on solving the partial differential equation, is shown in Equation B.1.

$$
4\pi\rho_0 c_0^2 = \frac{\partial^2}{\partial x_i \partial x_j} \int_{V_o} \left[\frac{T_{ij}}{r|1-M_r|} \right]_{\tau=\tau^*} \mathsf{d}V(\mathbf{z}) \quad - \frac{\partial}{\partial x_i} \int_{S_o} \left[\frac{(\rho\nu_i(\nu_i - V_i) + p_{ij})n_j}{r|1-M_r|} \right]_{\tau=\tau^*} \mathsf{d}S
$$
$$
+ \frac{\partial}{\partial t} \int_{S_o} \left[\frac{(\rho\nu_j - \rho'V_j)n_j}{r|1-M_r|} \right]_{\tau=\tau^*} \mathsf{d}S \tag{B.1}
$$

Where M_r is the Mach Number taken w.r.t the observer located at a distance r from the source, v_i is the velocity of the sound source, V_i is the velocity of the surface, τ is the retarded time, which is defined as the time taken for the acoustic fluctuations to reach the observer from the source, taking into account the time it was emitted, called the emission time (defined by 't') and the time it takes to reach the observer (defined by the distance between the source and the observer). This is defined by Equation B.2. The asterisk indicates that the sound reaches the observer from the source at the corrected emission time, defined as $\tau^* = t - r(\tau^*)/c_\infty$.

$$
\tau = t - \frac{r}{c_0} \tag{B.2}
$$

It is also interesting at this point to introduce a popular formulation in the literature by Farassat, that involved the description of using Kirchhoff's formulation [76] to rigid surfaces. This is the formulation that has been described by Equation B.1, and is valid for stationary observers and for a surface that is moving at an arbitrary speed. This has also been extended to two dimensional surfaces by implementing two dimensional frequency formulation that uses a modified Green's function [77].

The biggest takeaway from the FW-H equations is the fact that it clearly distinguishes between the three major sources of sound for rotor noise, which is relevant in the case of wind

turbine, propeller and helicopter blades. This includes quadrupoles, denoted by the first term with Lighthill's stress tensor T_{ij}. It represents the sound radiated by both turbulence as well as other non-linear flow disturbances, such as shock waves occurring on the blade surface. The second term represents the dipole source term, and it gives an indication of the surface loading (given by p_{ij}) on the blade. Lastly, the third term represents the thickness noise or the volume displacement source term, which is non-zero only when the observer sees a time varying surface velocity at the emission time. The separation of the source terms allows one to compute only the main sources of flow (for example, calculating quadrupole noise for low Mach number flows). The other advantages of this method include the numerous algorithms that can be used to calculate the contribution of the noise sources.

However, the FW-H equations have one disadvantage, and that is the requirement of volume integration over the entire source region in order to compute the contribution of noise from the quadrupole source within the domain. Since volume integration is computationally expensive, the quadrupole noise sources would have to be approximated, but this issue cannot be completely removed.

B.3. Implementation of FW-H equations in SU2

The FW-H equations in SU2 have been implemented by using several functions that can be explained by using the following inputs as shown in the following flowchart format as shown in Figure B.1.
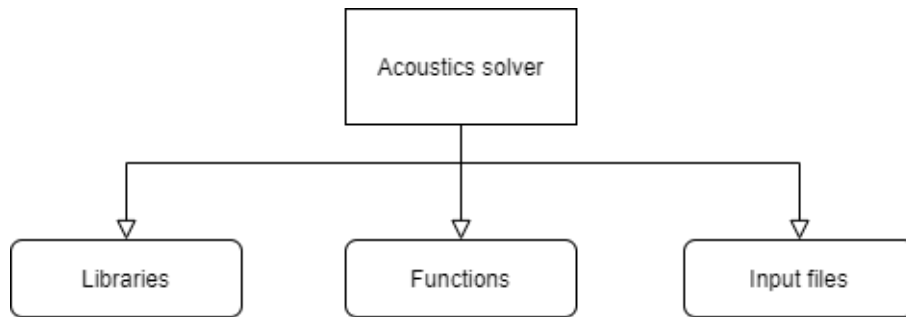
Figure B.1: Flowchart showing overview of acoustics solver

According to Figure B.1, the acoustics solver can be briefly classified into three major modules, namely:

1. The libraries that are imported.
2. The functions used for calculating various quantities.
3. The input files to be given to the solver.

Each of the above modules will be described in more detail in the upcoming sections of this chapter.

B.4. Libraries imported

The various libraries that are imported in the acoustics solver are summarized as follows:

1. **os:** Used to invoke the SU2_RUN environment variable to run SU2 along with the acoustics code.
2. **sys:** Used to append the SU2_RUN environment variable to the path where the acoustics code is present to run SU2 in tandem with the acoustics solver.
3. **optparse:** Allows the user to enter multiple inputs using a single parse command, to be sorted in the order given by the solver.
4. **numpy:** Allows for the user to perform multiple numerical operations, including scalar product calculations, reading text files and so on.

5. **pandas:** Allows to perform operations on text and csv files, including opening files, reading specific parts and closing files.
6. **glob:** Used to identify patterns in file names in order to read and extract information from them easily.
7. **pdb:** Used to provide an interactive debugger to the user to ensure the easy detection of errors and their subsequent correction.
8. **numba:** Used to simply parallelization of the code by extending its operation on multiple systems for complex geometries.
9. **struct:** Provides an easier pathway to read a structure present in a given dat file.
10. **sys:** Provides a system variable to invoke the `SU2_RUN` environment variable.
11. **time:** Used to provide an indication of how much time every operation takes.
12. **scipy:** Provides functions to perform operations such as `interp1d` for the interpolation between grid points and, `griddata` for extracting information from grid points.
13. **timeit:** Function to time the operating time required for the code to run as an indication to the user.

B.5. Functions involved in code
This section describes the various functions involved in the acoustics code in detail.

B.5.1. `compute_scalar_product`
This function obtains the product of two arrays $A = (a_1, a_2, a_3)$ and $B = (b_1, b_2, b_3)$, according to the scalar product rule as shown in Equation B.3.

$$A \cdot B = a_1 b_1 + a_2 b_2 + a_3 b_3 \tag{B.3}$$

This function is invoked later when computing the normal component of velocities when identifying noise sources from the flow by the function `Extract_NoiseSources`.

B.5.2. `read_binary_fwh`
This function reads the binary FW-H file and performs the following functions:

1. Displaying the message "Reading file".
2. Extracts the number of time steps ($ntime$) and number of points in the geometry as well, the latter being to determine the number of degrees of freedom ($ndof$) in the problem.
3. Displays the file size in bytes.
4. Starts a timer to compute the time taken to obtain the solution, and displays the time.

B.5.3. `write_binary_fwh`
This function opens an empty binary file, writes the parameters $ntime$, $ndof$ and $ntime * ndof$ in one go, and closes the file.

B.5.4. `CSVtoArray`
This function reads all the `surface_flow` files in the CSV format, sorts them and converts them into a binary format. It then returns a single, binary data file called `data_file`.

The next set of functions obtain the sources of sound in the flow field and calculate the pressure spectrum from them in that sequence by recovering the various parameters necessary to solve the FW-H equations.

B.5.5. `Compute_RadiationVec`
This function computes the radiation vector from the source to the observer (located at $(x_{obs}, y_{obs}, z_{obs})$), taking into account the Glauert compressibility factor (defined by $\beta = \sqrt{1 - M^2}$). This function defines the coordinates, surface normals as well as the number of panels. It also returns the surface geometry along with the radiation vector. This function also provides a difference between

the analogies of the FW-H equations (1A vs. `1A_WT`), by including the compressibility factor in the latter as a wind tunnel correction. The radiation vectors are calculated by using Equations B.4, B.5 and B.6 for the 1A formulation, and Equations B.7, B.8 and B.9 for the 1A WT formulation respectively.

$$|r_{mag}| = \sqrt{(x_{obs} - x)^2 + (y_{obs} - y)^2 + (z_{obs} - z)^2}$$

$$r_{1,1A} = \frac{(x_{obs} - x)}{|r_{mag}|} \tag{B.4}$$

$$r_{2,1A} = \frac{(y_{obs} - y)}{|r_{mag}|} \tag{B.5}$$

$$r_{3,1A} = \frac{(z_{obs} - z)}{|r_{mag}|} \tag{B.6}$$

$$r^* = \sqrt{r_1^2 + \beta^2(r_2^2 + r_3^2)}$$

$$|r_{mag,1A\_WT}| = \frac{(-M_\infty \cdot (x_{obs} - x) + r^*)}{\beta^2}$$

$$r_{1,1A\_WT} = \frac{(-M_\infty \cdot (x_{obs} - x)) + (x_{obs} - x)}{\beta^2 \cdot |r_{mag,1A\_WT}|} \tag{B.7}$$

$$r_{2,1A\_WT} = \frac{(y_{obs} - y)}{|r_{mag,1A\_WT}|} \tag{B.8}$$

$$r_{3,1A\_WT} = \frac{(z_{obs} - z)}{|r_{mag,1A\_WT}|} \tag{B.9}$$

B.5.6. `Extract_NoiseSources`

The inputs that are given to this function are the number of panels, observer locations and the surface geometry. It calculates the momentum fluxes from all three coordinate inputs (x,y and z respectively), and provide an output thta gives the different sources of sound (in this case, the monopole and dipole sources only are used). These momentum fluxes are obtained by using Equations B.10, B.11 and B.12 respectively. The total flux formulation is given by B.13. This momentum flux is indicative of the monopole source of noise from the flow.

$$F_1 = \rho(u_x \cdot n_x + u_y \cdot n_y + u_z \cdot n_z)u_x + (p - p_\infty) \cdot n_x \tag{B.10}$$

$$F_2 = \rho(u_x \cdot n_x + u_y \cdot n_y + u_z \cdot n_z)u_y + (p - p_\infty) \cdot n_y \tag{B.11}$$

$$F_3 = \rho(u_x \cdot n_x + u_y \cdot n_y + u_z \cdot n_z)u_z + (p - p_\infty) \cdot n_z \tag{B.12}$$

$$F_r = F_1 \cdot r_1 + F_2 \cdot r_2 + F_3 \cdot r_3 \tag{B.13}$$

B.5.7. `Extract_Mean`

This function provides the same output as `Extract_NoiseSources`, but by subtracting the mean value of the total momentum flux calculated from it, as shown in Equation B.14.

$$F_r = F_r - \overline{F_r} \tag{B.14}$$

Where the bar over F_r represents the mean value of F_r.

B.5.8. `Compute_RetardedTime`

This function calculates the time-varying momentum flux in accordance with the retarded time theory. Taking the same inputs as the `Compute_RetardedTime` function along with the time step as an input, the surface velocity and the speed of sound in that medium are also taken into consideration by taking a forward differencing scheme into account to interpolate the values obtained from the nearest neighbours in a given stencil (given the fact that the FW-H equation is first order in time, but calculating the velocity derivative requires a second time derivative which requires a second order stencil to solve for velocity). Using these, the time-varying momentum

flux F_r is calculated, with the appropriate weights are provided depending on the location of the node. This is provided by Equation For all other nodes. This, in fact, represents the dipole contribution of the sound sources, and is the discrete form of the right hand side of Equation B.1.

$$\dot{F}_r = \frac{-F_{r,i+2} + 4\,F_{r,i+1} - 3\,F_{r,i}}{2\,\Delta t} \qquad \text{(For the first node)}$$

$$\dot{F}_r = \frac{F_{r,i-2} - 4\,F_{r,i-1} + 3\,F_{r,i}}{2\,\Delta t} \qquad \text{(For the last node)}$$

$$\dot{F}_r = \frac{-F_{r,i+2} + 4\,F_{r,i+1} - 3\,F_{r,i}}{2\,\Delta t} \qquad \text{(For all other nodes)}$$

Once the momentum fluxes are calculated, the pressure spectrum is then calculated by using the FW-H equations given by Equation B.15.

$$pp_{ret} = \frac{\left(\frac{\dot{F}_r}{r^*\,a_\infty} + \frac{F_r}{r^{*2}}\right)\,dS}{4\,\pi} \qquad (B.15)$$

B.5.9. `Compute_RetardedTime_WT`
Akin to the function `Compute_RetardedTime`, but includes Glauert's Mach number correction. This includes the definition of the loading terms L_r and L_m, that are used to define the terms on the right hand side of Equation B.1. Furthermore, this formulation also takes into account the Mach number in the direction of the source (denoted by M_r), that is simply an indication of the relative motion between the source(s) and the observer(s).

B.5.10. `Compute_ObserverTime`
This function calculates the time taken for the sound to propagate from the source to the observer in accordance with the retarded time theory described in Section B.2, according to Equation B.2. The source and observer times are computed by using a simple formula as shown in Equations B.16 and B.17 respectively.

$$t_{source} = dt * (iter_{start} + N^{th}_{sample} * F_{sample}) \qquad (B.16)$$

$$t_{Obs} = t_{source} + \frac{r}{a_\infty} \qquad (B.17)$$

Where dt is the acoustic time step to be taken into account, N^{th}_{sample} is the nth sample that is used to compute the sampling frequency, and F_{sample} is the sampling frequency. The final outputs that are given from this function are t_{interp} and t_{Obs} respectively.

The time step is also effectively "dilated" between two observer locations for a given sound source, and therefore, this function also calculates an interpolated time step dt_{interp} by taking into account this distance.

B.5.11. `Integrate_Sources`
This function integrates the pressure spectrum pp_{ret} that is calculated from the interpolated time step dt_{interp} with the pressure spectrum calculated from the time step dt. This spectrum is calculated in the time domain.

B.5.12. `Interp_PressureSignal`
This function interpolates the observer locations based on both the x and y coordinates, and obtains the interpolated pressure spectrum pp_{interp} calculated using t_{interp} from the function `Compute_ObserverTime`.

B.5.13. `SU2_SetSpline`

This function essentially obtains the velocity component normal to the surface of the geometry for each and every element. This is done by taking a weighted linear operator into consideration. There is also another function with the same name, that performs a similar operation, but by using a cubic spline.

B.5.14. `Interp_PressureSignal_Fast`

This function computes the final pressure signal in the time domain, by using the interpolated output for the geometry as defined by the function `SU2_SetSpline`. It finally returns the interpolated pressure spectrum accordingly.

B.6. Input files

The other aspects that are to be covered in the acoustics section include the following inputs to the solver as well, in addition to the configuration file, namely:

1. Surface normals drawn between two points.
2. Observer locations.
3. Configuration file.
4. Binary FW-H file.

B.6.1. Surface normals

The surface normals to the surface analyzed in this problem (the airfoil in this case) are obtained in two different ways, one by providing a normalized input to the solver by using a regular cross product, and the other, by using Newell's method of computing the surface normals, which gives the normals in the absolute sense without normalization. The formulation of Newell is based on the calculating the normals by taking the projections of each individual element by taking a weighted value of the two points using their sum and difference for the next and previous element respectively [78].

B.6.2. Observer locations

The observer locations are defined in a circular manner around the sound source. This is inspired by the tutorial that has been used for the tandem cylinders case. A comparison between the two is depicted in Figure B.2.

(a) Test case   (b) Tandem cylinders
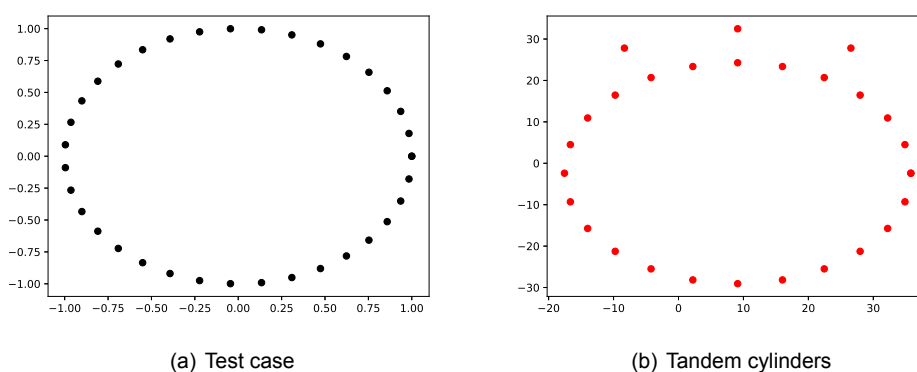
Figure B.2: Comparison of observer locations as taken in (a) Test case and (b) Tandem cylinder case [73]

From Figure B.2, it can be clearly seen that there is the presence of three additional observers in the tandem cylinder case as shown by Molina. This could account for the presence of an additional permeable surface or a given section for which the noise is evaluated.

B.6.3. Configuration file

The configuration file provides an insight to the user about the flow conditions that are used for the geometry. This is simply used to provide inputs such as the Mach number, Reynolds number, number of dimensions of the problem, sampling frequency, the type of analogy ($1A$ or `1A_WT`), and the kind of FW-H formulation used (solid or permeable).

B.6.4. Binary FW-H file

The information regarding the unsteady pressure fluctuations is stored in a binary file called `fwhbin.dat`, that is automatically generated by invoking the function `write_binary_fwh`.

B.7. Overview of working of acoustics code

The initial acoustics code that was investigated was an extension of the one created by Eduardo Molina for the tandem cylinder test case [73], whose file was divided into several sections. The summary of the method in which they had performed the acoustic calculation are given by the following steps:

1. The various input files are read by the acoustics solver, with the various vtk files that are provided as the inputs being converted into a single binary file using a user-defined function, that provides information about the surface pressure fluctuations to the solver in a single file.

2. The observer locations are provided as inputs to the solver in the form of a `.dat` file in a circular manner. This has been inspired by the way the observers are placed by Molina et. al. as shown in Figure B.2.

3. The surface normals are provided as inputs to the current solver for the purpose of calculating the projection of the radiation vector from the source in the direction of the observers.

4. The observer locations are also required for the purpose of calculating the radiation vector itself. This vector is used in the 1A Farassat formulation of the FW-H equations.

5. Of the different formulations of the FW-H equation available, the `1A_{WT}` formulation (standing for 1A, Wind Tunnel) is used, as it accounts for compressibility effects (by including the Glauert factor ($\beta = \sqrt{(1 - M^2)}$)) and has lesser bugs in comparison to the 1A formulation.

6. The retarded time approach is used as the default setting for the purpose of solving the FW-H equations in SU2. And given the computational requirements for the current problem (airfoil in deep stall), as well as the accuracy of the retarded formulation, it is safe to say that the retarded formulation is better used for the purpose of this problem.

7. The observer time (τ) is then calculated in accordance with the retarded time equation and in terms of the source time, as given by Equation B.18.

$$\tau = t_{source} + \frac{r}{a_\infty} \tag{B.18}$$

   Where r is the radiation vector from the source to the observer, and a_∞ is the speed of sound in the medium.

8. The pressure signal is given as the output in the time domain, which can be converted into the frequency domain by using a Fast Fourier Transform (FFT) in the post-processing stages.

9. The freestream conditions that are given as inputs, such as the Mach number, Reynolds number, number of dimensions of the problem, sampling frequency, the type of analogy ($1A$ or `1A_WT`), and the kind of FW-H formulation used (solid or permeable) are provided as inputs.

10. The outputs of the noise is stored in a separate file called `observers.dat` for every observer location.

$$C$$
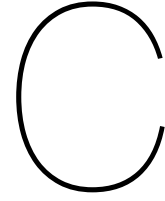
Appendix C

C.1. Uncertainty in force coefficients

In order to provide a statistical investigation of the lift and drag coefficients, the number of time samples taken into account in the simulation (denoted by T) were used to calculate the confidence intervals. Therefore, the relative errors of the mean (denoted by μ) and standard deviation (denoted by σ) of the lift and drag coefficients were found according to Equations C.1 and C.2 respectively. Furthermore, the 95% confidence interval corresponding to a quantity ϕ (ϕ = σ or μ) is given by the relation C.3.

$$\varepsilon[\mu] \approx \sqrt{\frac{1}{2BT}} \frac{\sigma}{\mu} \tag{C.1}$$

$$\varepsilon[\sigma] \approx \sqrt{\frac{1}{4BT}} \tag{C.2}$$

$$\frac{\phi}{1 + 2\varepsilon[\phi]} \leq \phi \leq \frac{\phi}{1 - 2\varepsilon[\phi]} \tag{C.3}$$

Where ε is the relative error corresponding to each quantity, T are the total number of convective time units for which the simulation was run ($T = tc/U_\infty$) and B is the error scaling bandwidth. These relations were obtained as a part of the best practice guidelines that were provided based on the outcomes of the DESider project [14].

According to the findings of the DESider project, for NACA 0021 at an angle of attack of $60°$, the value of B is equal to 0.149 for C_l and 0.0898 for C_d. In the current simulation settings, a total physical time of 149.76 s, corresponding to 5200 T were taken to compare the results with experimental data. Rounding the physical time to 150 s would mean that $T = 5400$, but it was found that the difference in the relative errors calculated from the two was within an order of 10^{-3}. Therefore, a value of 5400 T was taken, as the simulations performed earlier were for this value of T.

3D values of C_l and C_d
Plugging in the values of T, B, σ and μ, we get the corresponding relative errors as shown in Table C.1, and the confidence intervals as an indication of the uncertainty of the mean and standard deviation as shown in Table C.2.

Parameter	$\varepsilon[\mu]$	$\varepsilon[\sigma]$	$\mu \pm \sigma$
3D C_l	0.006649	0.017627	1.070977 ± 0.280332
3D C_d	0.007196	0.022706	1.757762 ± 0.393944

Table C.1: Calculation of relative errors of C_l and C_d - 3D values

From Table C.1, it can be observed that the error associated with C_d is higher for the mean values as compared to the error in the mean values for C_l. This accounts for the fact that because of the complex flow physics, the drag coefficient is found to be difficult to predict at such high angles of attack. This was also observed in the analysis of Garbaruk [10], when they had computed the relative errors for C_l and C_d, albeit using a different formula. The high error is attributed to the presence of a narrow span as well ($1c$ compared to $4c$).

The confidence intervals correspond to the mean and standard deviations of the 3D C_l and C_d are given by Table C.2.

Parameter	Confidence interval $[\mu]$	Confidence interval $[\sigma]$
3D C_l	$1.056922 \leq 1.070977 \leq 1.085411$	$0.270786 \leq 0.280332 \leq 0.290576$
3D C_d	$1.732823 \leq 1.757762 \leq 1.783429$	$0.376831 \leq 0.393944 \leq 0.395741$

Table C.2: Confidence intervals for 3D C_l and C_d

From Figure C.2, it can be observed that the uncertainty (difference in the maximum and minimum values) in the mean value of C_l is found to have a confidence that has a lesser uncertainty than the uncertainty in the standard deviation of C_d. Furthermore, it can also be seen that the confidence intervals of the standard deviation are more uniformly distributed about the standard deviation in comparison to that of the confidence intervals of the mean. However, a more holistic comparison can only be made by comparing these values with their corresponding ones obtained from the sectional force coefficients.

2D values of C_l and C_d
The corresponding values of these relative errors, when computed for the 2D sectional C_l and C_d values are given in Table C.3. This is calculated at $x/b = 0.363$, which corresponds to the same section where the pressure taps were placed in the experiment of Swalwell [6].

Parameter	$\varepsilon[\mu]$	$\varepsilon[\sigma]$	$\mu \pm \sigma$
2D C_l	0.0124287	0.017627	2.182515 ± 1.088147
2D C_d	0.016753	0.022706	1.178013 ± 0.614612

Table C.3: Calculation of relative errors of C_l and C_d - 2D values

From Table C.3, it can be observed that just like the 3D lift coefficient, the error associated with the sectional C_d is higher for the mean values as compared to the error in the mean values for C_l. Comparatively, in this case, the error is comparatively higher for the sectional 2D coefficient than the corresponding 3D values. This can be due to the fact the calculation of the spanwise coefficients seem to have again raised the concern for having a geometry with a narrower span as well.

In order to provide a better meaning to the confidence intervals obtained from the 3D C_l and C_d values, the confidence intervals correspond to the mean and standard deviations of the 2D C_l and C_d are also obtained, as given by Table C.4.

Parameter	Confidence interval $[\mu]$	Confidence interval $[\sigma]$
2D C_l	$2.129579 \leq 2.182515 \leq 2.2381496$	$1.051092 \leq 1.088147 \leq 1.12791$
2D C_d	$1.139822 \leq 1.178013 \leq 1.218852$	$0.587914 \leq 0.614612 \leq 0.643851$

Table C.4: Confidence intervals for 2D C_l and C_d

On comparing Tables C.4 and C.2, it can be clearly observed that the there is a clear drift in the confidence intervals of the mean values of, which are also mimicked by the confidence intervals of the standard deviation. This has been a behaviour observed even in the case of longer simulation time periods, as has been described by Garbaruk [10] as well.

A general conclusive remark that can be made for this analysis is that there can be a better comparison that could be made for future validations, if the same statistical analysis can be

performed for a geometry having a span $4c$. This way, it can also be confirmed that the ratio of σ/μ is found to be larger for the smaller geometry, which was also an important finding from Garbaruk [10]. However, this does not apply for standard deviations, as the statistical error is unaffected by the span size.

C.2. LES capability test of current grid

In order to test the LES capability of the current DDES grid, that has been described in quite a bit of detail in Section 3.1.1, a spectral analysis is performed by obtaining the variation of the resolved unsteady velocity field with Strouhal number. This method, although used for LES grids, is a good test can be used to detect whether the filter cut-off wave number lies within the inertial sub-range or not. This test was performed for DES grids made by Mockett et. al. [63].

The reason for choosing this paper when comparing the existing SU2 results is because of the fact that at such a high angle of attack, it would make sense to consider the airfoil as a bluff body. Given that the flow separation occurs virtually at the leading edge itself, as has been depicted by several flow illustrations in previous sections, the airfoils, regardless of their thickness, behave in very similar manners. Hence, the comparison between different airfoils (namely, NACA 0012 and NACA 0021) at the same angle of attack of $60°$ is justified. The same reasoning has also been provided by Yan et. al [3] when comparing their results with another airfoil at the same angle of attack.

The variation of the turbulence kinetic energy is also compared with the variation of the turbulence dissipation rate (denoted by ε), which is a function of the turbulent kinetic energy (given as a function of wave number κ) as shown in Equation C.4. This is nothing but Kolmogorov's law of energy cascade [79], which is a clear indicator that the energy is being transferred from the larger scales to the smaller ones, and being dissipated at the smaller scales.

$$E(\kappa) \propto \kappa^{2/3}\varepsilon^{-5/3} \tag{C.4}$$

Where κ is the wave number and ε is the turbulent dissipation rate.

The results obtained from the simulation for this case are obtained for four different chordwise locations, namely at $x/c = 0.225$, $x/c = 0.275$, $x/c = 0.735$ and at $x/c = 2$ respectively. The reason for choosing these locations is because of the fact that at the first two locations, one can observe the boundary layer detaching from the suction side of the airfoil surface. This would cause a redistribution of the turbulent kinetic energy from the boundary layer to the flow itself, as well as the presence of the formation of a leading edge vortex, as has been described by Lacagnina et al. [5]. This results in the presence of a peak, as can be seen in the following figures. The last two locations, namely $x/c = 0.735$ and $x/c = 2$, are in order to obtain an insight of the flow physics after the detachment of the boundary layer from the suction side of the airfoil surface. And as for the location $x/c = 2$, this location provides an insight into the development of the wake downstream of the airfoil.

Hence, on a logarithmic plot, the slope of the turbulent kinetic energy is plotted along with the resolved unsteady velocity field, which gives an estimate of the deviation of the same at higher frequencies. This is shown at different locations downstream of the location where flow separation occurs in Figures C.1 and C.2 respectively. It is also to be noted that the data obtained from Mockett has been digitized, and therefore, at higher frequencies, there is a clear demarcation of frequencies rather than a continuous spectrum.
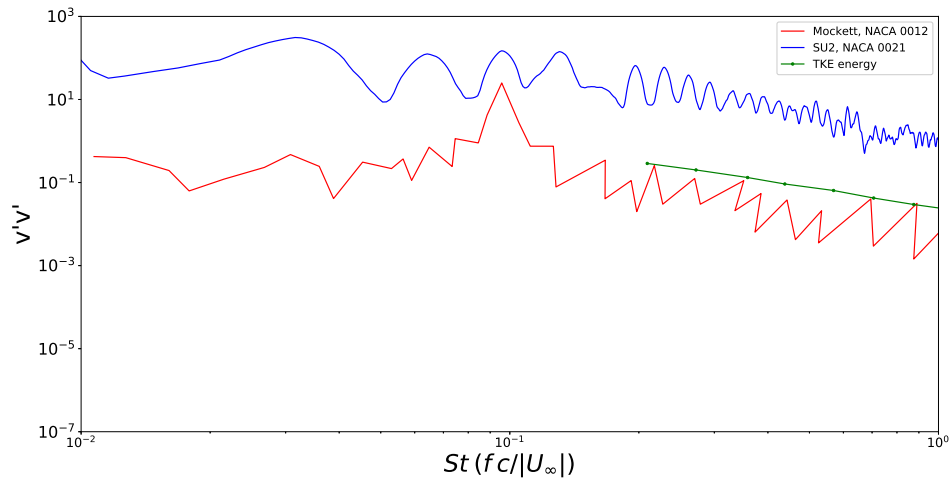
(a) $x/c = 0.225$
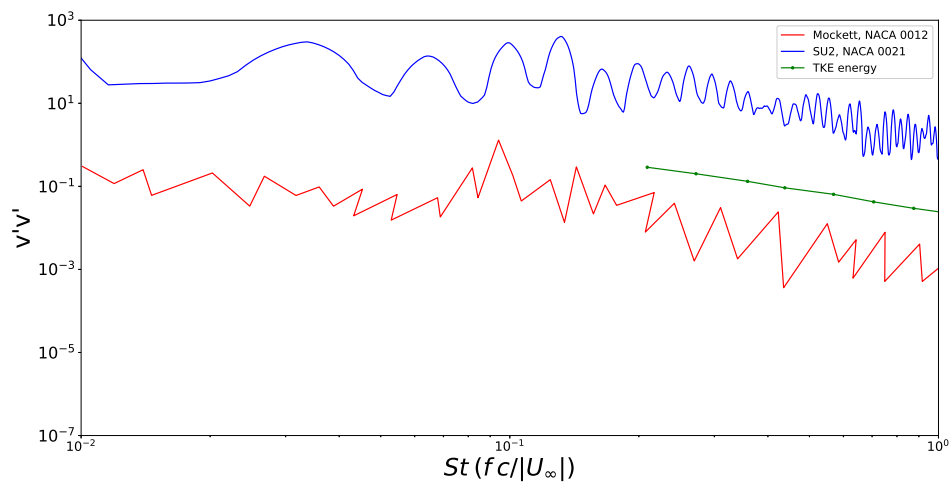
(b) $x/c = 0.275$

Figure C.1: Variation of $v'v'$ vs. St at $x/c = 0.225$ and $x/c = 0.275$

From Figure C.1, it can be observed that the there is a clear over-prediction of the resolved velocity fluctuations for the current grid, which can be accounted for due to the fact that the DDES solution that can be extracted from the current grid does not provide an accurate indicator of the resolved velocity fluctuations. This can also be seen in the prediction of the peaks at lower Strouhal numbers, which is indicative of the fact that despite removing the noise from the PSD signal, there are multiple peaks that can be observed (one additional peak just before the main peak at $x/c = 0.225$ and two additional peaks just before the main peak at $x/c = 0.275$). Lastly, one final observation that can be made for this analysis is that at higher frequencies, the slope of the PSD spectrum obtained is comparable to that obtained for the -5/3 spectrum of the turbulent kinetic energy. This is also a good verification that the relation between the turbulent kinetic energy and the wave number is indeed justified (since higher the wave number, higher the frequency and hence, higher the energy content).
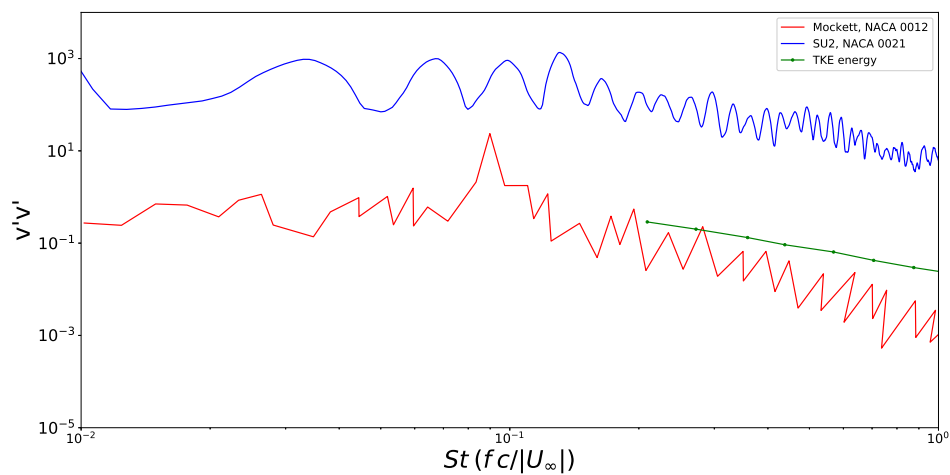
(a) $x/c = 0.735$
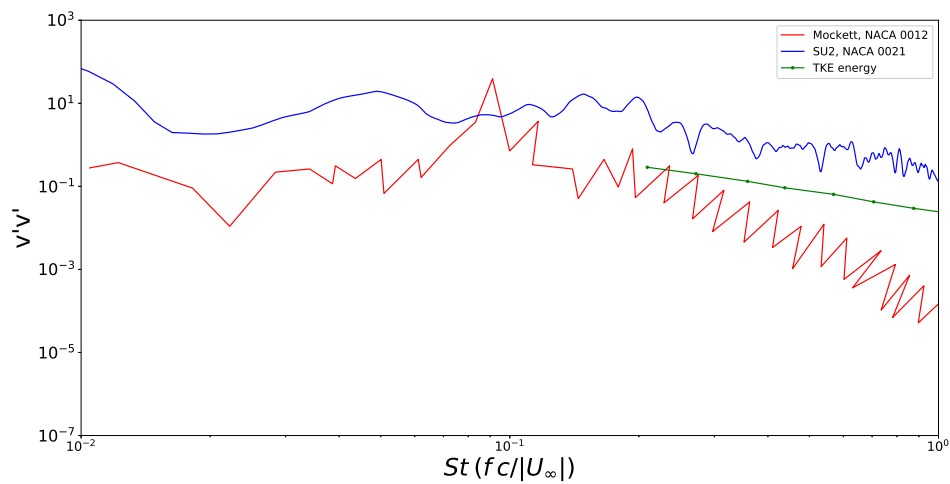
(b) $x/c = 2$

Figure C.2: Variation of $v'v'$ vs. St at $x/c = 0.735$ and $x/c = 2$

From Figure C.2, it can be observed that at $x/c = 0.735$, there is the presence of multiple peaks again despite the noise being removed from the PSD signal. This can be attributed to the fact that there could be multiple vortices which are detected at this chord-wise location, which could account for this. Furthermore, one can also observe that once again, at higher frequencies, there is a good agreement between the slope predicted by the -5/3 line and that followed by the PSD spectrum of the resolved fluctuating velocities. One important observation that can be made regarding the PSD spectrum at $x/c = 2$ is the absence of peaks corresponding to vortex shedding. This can be accounted for as due to the fact that at that spatial location, the vortices are essentially dissipated due to turbulence, which causes no real detection of the same. This can be further verified in the eddy viscosity as well as the pressure contours of earlier sections. Furthermore, another very interesting, and also important observation, that can be made with regards to the higher frequencies. There is a clear deviation of the trend observed in the DES grid in comparison to the DDES grid at higher frequencies. This can be due to the fact that at higher wave numbers for this spatial location, there is a tendency to deviate from the -5/3 rule, because of the fact that there is a higher turbulent dissipation occurring at that location for the DES grid. This could be a consequence of the fact that DES suffers from the issue of

MSD (modified stress depletion), in which the grid suffers from a lower eddy viscosity prediction than that predicted from Equation C.4. Since the DDES results do not have this discrepancy because of a smoother transition from RANS to LES, it can be concluded that this is indeed, a good reason to use DDES over DES. Although Spalart has mentioned in his paper that extreme grids using the DDES approach do suffer from this problem [46], the current grid is too coarse to be considered in that category.

A general comment that can be made with regards to how the higher frequency content varies with the -5/3 line can be attributed to the cut-off wave-number for the grid, which is invariably defined by the grid size. This is a characteristic feature of DDES grids, which allows for transition from RANS to LES in a much smoother manner compared to DES. To conclude, this study concludes one of the most important parts of verifying the LES capability of the grid. It would be useful in future studies to compare these results with the fine mesh as well.

C.3. Attempts for fine mesh

It would be incomplete to not mention the fact that a finer mesh was attempted to be run using a span of $4c$ for the same airfoil (NACA 0021), in order to test the validity of the SLA-SGS model for a geometry having a higher span. Furthermore, this was also the recommendation of Garbaruk [10], which proved that there is a need for using a geometry of a higher span for the purpose of obtaining a much better comparison with experimental data. The following settings were applied for the same:

1. The mesh was run with different convective CFL numbers (of orders between 10^{-1} - 10^{1}).
2. Using an adaptive CFL setting, with changing the adaptive values (minimum and maximum CFL with their corresponding factors).
3. The mesh was operated using different hybrid SGS models available for DDES, including the ones adapted for shear layer flows (vorticity-based and the shear-layer adapted).
4. The use of a different slope limiter available (`VENKATAKRISHNAN_WANG` in this case) was also attempted.
5. Using a different linear solver (`LU_SGS`) was also attempted.

In all the above cases, the major problem that was encountered was that the linear solver had diverged, either at the beginning of the solution, or after a few runs. Therefore, it was concluded that a more detailed investigation into the fine mesh would have to be made in the future.